Alma Mater Studiorum - Università di Bologna

DOTTORATO DI RICERCA IN

SCIENZE E TECNOLOGIE AGRARIE, AMBIENTALI E ALIMENTARI

Ciclo 34

Settore Concorsuale: 07/C1 - INGEGNERIA AGRARIA, FORESTALE E DEI BIOSISTEMI

Settore Scientifico Disciplinare: AGR/09 - MECCANICA AGRARIA

HYPERSPECTRAL IMAGING AND OTHER OPTICAL TECHNIQUES FOR (IN-FIELD/IN-LAB) PHYSICO-CHEMICAL ATTRIBUTES ESTIMATION OF AGRI-FOOD VEGETAL PRODUCTS

Presentata da: Alessandro Benelli

Coordinatore Dottorato

Massimiliano Petracci

Supervisore

Angelo Fabbri

Co-supervisori

Luigi Ragni

Chiara Cevoli

Esame finale anno 2022

INDEX

Glossary of acronyms and abbreviations

°Bx	Degrees Brix
A	Absorbance
A_C	Calibrated diffuse absorbance spectrum
ACS	American Chemical Society
ANN	Artificial neural network
ANOVA	Analysis of variance
ASD	Analytical Spectral Devices
ATV	All-terrain vehicle
AUC	Area under the curve
BB	Branch and bound
BLW	Broadleaf weeds
c	Concentration of absorbing species
CA	Conservation agriculture
C_{ab}	Chlorophyll content
Cal.	Calibration
CARS	Competitive adaptive reweighted sampling
CCD	Charge-coupled device
CFS	Correlation-based feature selection
CMOS	Complementary metal-oxide semiconductor
CNN	Convolutional neural networks
COW	Correlation optimised warping
CR	Continuum removal
CV	Canopy volume
D1	First derivative
DA	Discriminant analysis
DM	Dry matter
DSS	Decision support system
DW	Dry weight
EFL	Effective focal lenght
EMSC	Extended multiplicative scatter correction
EN	Electronic nose
ERDC	U.S. Army Engineer Research and Development Center
FAO	Food and Agriculture Organisation of the United Nations
FB-HTP	Field-based high-throughput phenotyping
FF	Flesh firmness
FLC	Flavonols content
FLDA	Fisher's linear discriminant analysis
FOW	Field of view
FPS	Frames per second
GA	Genetic algorithm
GBRST	Ground-based remote sensing techniques
GDD	Growing degree days
GNDVI	Green normalised difference vegetation index
GR	Glyphosate-resistant
GRNN	Generalised regression neural network
GS	Glyphosate-sensitive
GW	Grass weeds
HLBI	Hyperspectral light backscattering imaging
HS	Hyperspectral
HSC	Hyperspectral camera
HSD	Honestly significant difference
HSI	Hyperspectral imaging
HTP	High-throughput phenotyping
I	Transmitted radiation intensity
I_0	Incident radiation intensity
IFA	Intelligent Fruit Analyser
IFD	Intelligent Firmness Detector
iPLS	Interval partial least squares
IVA	In-field visual assessment
JPL	Jet Propulsion Laboratory
K	Cohen's kappa coefficient
kNN	k-nearest neighbour

l	Path length
LD	Leaf density
LiDAR	Light detection and ranging
LLBI	Laser light backscattering imaging
LNC	Leaf nitrogen content
LV	Latent variable
M	Measured value
MC	Mean centred
MIR	Mid-infrared
MIS	Magnetic induction spectroscopy
ML	Maximum likelihood
MLBI	Multispectral light backscattering imaging
MLP	Multilayer perceptron
MLR	Multiple linear regression
mND	Modified normalised difference
MOG	Mixtures of Gaussians
MRI	Magnetic resonance imaging
MRMR	Minimum redundancy-maximum relevance
MS	Multispectral
MSC	Multiplicative scatter correction
MTf	Magness-Taylor flesh firmness
N	Newton
NASA	National Aeronautics and Space Administration
NDVI	Normalised difference vegetation index
NIR	Near-infrared
NNI	Nitrogen nutrition index
nv	number of variables
OIV	International Organization of Vine and Wine
P	Mean predicted value
PA	Precision agriculture
PCA	Principal component analysis
PCR	Principal component regression
PGP	Prism-grating-prism
PIA	Photo interpretation assessment
PLA	Projected leaf area
PLS	Partial least squares
PLScomp	PLS components
PLS-DA	Partial least squares discriminant analysis
PLSR	Partial least square regression
Pred.	Prediction
PRI	Photochemical reflectance index
PRI	Partial root zone drying irrigation
PV	Precision viticulture
R	Reflectance
r	Correlation coefficient
R^2	Coefficient of determination
R^2_{CV}	Coefficient of determination of cross-validation
R^2_P	Coefficient of determination of prediction
R_C	Calibrated diffuse reflectance spectrum
R_D	Dark reference reflectance spectrum
RDI	Regulated deficit irrigation
RE	Relative error
RI	Raman imaging
RMSE	Root mean square error
RMSECV	Root mean square error of cross-validation
RMSEP	Root mean square error of prediction
ROC	Receiver operating characteristic
ROI	Region of interest
r_P	Correlation coefficient of prediction
RPD	Residual prediction deviation
rPLS	Recursive weighted partial least squares
R_R	Raw diffuse reflectance spectrum
R_W	White reference reflectance spectrum
R_λ	Reflectance at a given wavelength
s	Lighting time
SA	Simulated annealing
SAW	Surface acoustic wave

SAWR	Surface acoustic wave resonator
SEP_c	Standard error of prediction corrected of the bias
SERS	Surface enhanced Raman scattering
SIMCA	Soft independent modelling class analogies
SIPI	Structural independent pigment index
SiVM	Simplex volume maximisation
SNV	Standard normal variate
SOM	Self-organising maps
SORS	Spatially offset Raman spectroscopy
SPA	Successive projections algorithm
SPAD	Soil plant analysis development
SSC	Soluble solids content
SSPP	Spectral-Sensitive Pulsed Photometry
SVM	Support vector machines
SVR	Support vector regression
SWIR	Short-wave infrared
SWNIR	Short-wave near-infrared
SWR	Stepwise regression
TA	Titratable acidity
TCC	Total carotenoids content
Tc-Ta	Canopy expansion
TD-GC/MS	Thermal desorption gas chromatography/mass spectrometry
TIR	Thermal infrared
TPC	Total phenolic content
TRS	Time-domain diffuse reflectance spectroscopy
TSS	Total Soluble Solids
TWC	Turf water content
UAV	Unmanned aerial vehicle
UGV	Unmanned ground vehicle
UV	Ultraviolet
UVE	Uninformative variable elimination
V	Voltage
VI	Vegetation index
VIP	Variable importance in projection
Vis	Visible
VNIR	Visible to near-infrared
VOCs	Volatile organic compounds
VRT	Variable rate technology
WAR	Width across-row
WIR	width in-row
Y	Measured response
$\hat{Y}$	Predicted response
γ	Outlier significance level
ε	Molar decadic extinction coefficient
λ_{ref}	Reference wavelength

ABSTRACT

In the agri-food sector, measurement and monitoring activities contribute to high quality end products. In particular, considering food of plant origin, several product quality attributes, vegetation indices characterising plant growth, the state of plant hydration, the degree of fruit maturity or the presence of defects and diseases in the plant or the fruit itself can be monitored. Among the non-destructive measurement techniques, a large variety of optical techniques are available, including hyperspectral imaging (HSI) in the visible/near-infrared (Vis/NIR) range, which, due to the capacity to integrate image analysis and spectroscopy, proved particularly useful in agronomy and food science. Many published studies regarding HSI systems were carried out under controlled laboratory conditions. In contrast, few studies describe the application of HSI technology directly in the field, in particular for high-resolution proximal measurements carried out on the ground.

Based on this background, the activities of the present PhD project were aimed at exploring and deepening knowledge in the application of optical techniques for the estimation of quality attributes of agri-food plant products. First, research activities on laboratory trials carried out on apricots and kiwis for the estimation of soluble solids content (SSC) and flesh firmness (FF) through HSI were reported; subsequently, FF was estimated on kiwis using a NIR-sensitive device; finally, the procyanidin content of red wine was estimated through a device based on the pulsed spectral sensitive photometry technique. In the second part, trials were carried out directly in the field to assess the degree of ripeness of red wine grapes by estimating SSC through HSI, and finally a method for the automatic selection of regions of interest in hyperspectral images of the vineyard was developed.

The activities described above have revealed the potential of the optical techniques for sorting-line application; moreover, the application of the HSI technique directly in the field has proved particularly interesting, suggesting further investigations to solve a variety of problems arising from the presence of the many environmental variables that may affect the results of the analyses.

1. INTRODUCTION

The present section provides an overview of non-destructive measurement techniques based on optical spectroscopy and imaging. Next, visible/near-infrared spectroscopy is introduced in more detail, and finally, hyperspectral imaging is presented, describing the analytical process that starts with hyperspectral image acquisition and ends with the development of classification and prediction models.

1.1. Non-destructive spectroscopic and imaging techniques

Non-destructive assessment of food quality is a widely reported topic in recent scientific literature. The combined use of sensors based on optical technologies with mathematical models and algorithms allows to measure food quality attributes by identifying correlations with physical/chemical properties. Spectroscopy, a technique based on differentiation in frequency (wavelength) of electromagnetic radiation, is becoming even more accessible due to increased data processing capacities and simplification in calibration procedures (Ruiz-Altisent et al., 2010). In addition, in recent years the integration of spectroscopy with imaging is experiencing increasing application in quality and safety assessment of agricultural and food products (Adebayo et al., 2016). Spectroscopic techniques integrated with imaging include Raman, Vis/NIR, fluorescence, and light backscattering (Hussain et al., 2018).

Raman spectroscopy, relying on inelastic scattering of photons, provides a series of narrow, well-resolved bands that result from the vibration of covalent bonds (in particular, relatively neutral ones, such as intramolecular C–C, C–H, C=C) building up a structural fingerprint by which molecules can be identified; furthermore, Raman spectroscopy eliminates water interferences; finally, it is used to characterize the orientation of anisotropic crystal structures. Raman spectroscopy uses lasers as light sources, with spectral ranges from ultraviolet (UV) to NIR (Zhang, 2017). Accordingly, Raman imaging (RI) is used to identify the locations of chemical and crystal structures in samples (Hussain et al., 2018; Pathmanaban et al., 2019). Among the new evolution of Raman spectroscopy, surface enhanced Raman scattering (SERS) amplifies the scattering intensity of molecules by nanostructured metallic particles; spatially offset Raman spectroscopy (SORS), allowing deep probing of diffusely scattering objects (Mosca et al., 2021), has been used to evaluate internal maturity of tomato samples (Hussain et al., 2018).

NIR spectroscopy focuses on the vibrational movements of the hydrogen bonds in the functional groups of molecules, such as C–H, O–H and N–H, and is oriented to quantitative analysis, such as the determination of the concentration of chemical groups. Hyperspectral imaging (HSI) combines visible and/or near-infrared (Vis/NIR) spectroscopy and imaging, and it is widely used as an effective tool for agri-food quality assessment. HSI, like NIR spectroscopy, is primarily related to bonds involving the lightest atom, hydrogen, in functional groups (Delwiche, 2015). Each pixel in the image contains spectral data, which provides a map of the quality attributes of the sample (Hussain et al., 2018).

Fluorescence spectroscopy is based on the emission of a unique fluorescence occurring when specific organic compounds, fluorophores, are excited by ultraviolet/visible (UV/Vis) radiation, and in reverting to the ground state by photon emission, lose some of the absorbed energy due to vibrational relaxation of the excited state. As a result, according to the Stokes rule, the fluorescence spectrum shifts toward longer wavelengths, hence of lower energy, than the absorption spectrum (Hussain et al., 2018; Sikorska et al., 2019). Fluorescent organic compounds (fluorophores) frequently present conjugate systems of C=C double bonds, aromatic character, and rigid molecular skeletons. Fluorophores include polyaromatic hydrocarbons, heterocyclic compounds, and some highly unsaturated aliphatic compounds. In addition, the nature and position of substituents affect fluorescence characteristics as well (Sikorska et al., 2019). An interesting evolution of fluorescence spectroscopy is the hyperspectral fluorescence imaging (HSFI), which combines the advantages of fluorescence with those of spatial dimension; HSFI was used for the evaluation of fruit ripening and for the detection of defects, diseases, aflatoxin contamination, and faecal contamination (Sikorska et al., 2019).

While vibrational NIR and mid-infrared (MIR) spectroscopy can have low sensitivity for the quantification of minor food components, especially in those foods, such as fruit, that have water as a major component, fluorescence spectroscopy has the advantage of high sensitivity and selectivity for the study of minor and trace components in complex food matrices. In this context, Raman spectroscopy provides complementary information to MIR spectroscopy, with the advantage of eliminating interference from water, but has a low signal intensity and is subject to interference caused by the fluorescence of the sample (Sikorska et al., 2019).

Light backscattering is based on the information stored in the backscattered photons that interact with the internal components of the analysed sample. In fruits and vegetables, the joint surfaces of the cell wall mostly contribute to the backscattering effect, however suspended particles such as starch, chloroplasts and mitochondria can also generate diffusion by refraction on their surface. There are two light

backscattering techniques, monochromatic light backscattering imaging or laser light backscattering imaging (LLBI) and broadband light backscattering imaging, which can be split into multispectral light backscattering imaging (MLBI) and hyperspectral light backscattering imaging (HLBI). LLBI requires a monochromatic laser diode as light source; compared to MLBI and HLBI techniques, where the light source is usually a halogen lamp generating broadband light, LLBI can provide a higher light intensity per unit area, therefore light can penetrate deeper into the sample, generating more diffuse photons, which will hold more information. MLBI and HLBI, however, have the advantage of generating images containing full information in the considered wavelength range, whereas in the case of LLBI, information will be gained only in the considered wavelength (Mollazade et al., 2012).

1.2. Origins of hyperspectral imaging technology

Imaging spectrometry, a remote sensing technique introduced in the mid-1980s at the Jet Propulsion Laboratory (JPL) of the California Institute of Technology in Pasadena, sparked the development of hyperspectral imaging (Liu et al., 2015). Airborne and spaceborne sensors were applied for remote and direct identification of materials on the Earth's surface: the output were images of the observed surface, coupled with reflectance spectra consisting of up to 200 contiguous spectral bands (Goetz et al., 1985). In recent decades, imaging techniques have also been developed and implemented in the agro-industry for product assessment and classification (ElMasry & Sun, 2010). The integration of imaging techniques with spectroscopy, which occurred through the development of HSI technology, has also combined their strengths (Lu & Park, 2015).

1.3. Near-infrared spectroscopy

According to quantum theory, the absorption of light by a molecule occurs through discrete changes in energy levels (quantum levels); when a molecular interatomic bond absorbs an energy equal to the difference between two adjacent quantum levels, fundamental vibrations occur between the bonded atoms, characterised by specific vibrational wavelengths in the region of the mid-infrared (MIR, 2500–25000 nm). The presence of anharmonicity allows for overtone transitions and combination bands, whose vibrations are observed in the near-infrared range (NIR, 780–2500 nm). The observation of overtone and combination band vibrations in the NIR region provides

several benefits: (1) the absorption bands are weak, so no sample dilutions are required; (2) the largest vibrational movements concern the bonds of hydrogen atoms located in the functional groups of molecules (typically C–H, O–H, and N–H, prevalent in organic molecules), while the vibrations of intrachain bonds such as C–C are not active; (3) it is suitable for quantitative analysis, such as the determination of chemical group concentration; however, it is not suitable for qualitative analysis, since the high degree of band overlap does not allow the vibration of a chosen bond to be exactly assigned to a specific wavelength (Delwiche, 2015).

The calculation of the concentration of a solute in gases and liquids with negligible scattering is based on the Beer-Lambert law: $A = \log_{10}(I_0/I) = \varepsilon\ c\ l$, where A is the absorbance, I_0 is the incident radiation intensity, I the transmitted radiation intensity, ε the molar decadic extinction coefficient, c the concentration of absorbing species, and l the path length. In diffuse reflectance analyses, such as proximal or remote sensing hyperspectral analysis, the calculation of the concentration of the compound of interest is based on an approximation of the Beer-Lambert law: $\log_{10}(1/R) \approx$ [analyte], where R stands for reflectance and square brackets for concentration. A further simplification concerns the direct use of the reflectance R, assuming that the degree of non-linearity between R and its $\log_{10}$ reciprocal transform is irrelevant: for instance, in the R range 0.2–0.8 the coefficient of determination with $\log_{10}(1/R)$ is 0.97 (Delwiche, 2015).

Among the most relevant applications in the agro-food sector, NIR spectroscopy can be used to predict physico-chemical quality attributes related to the degree of ripeness of the fruit such as soluble solids content (SSC), flesh firmness (FF), acidity, phenolic content, and vitamin content (Liu et al., 2015; Chandrasekaran et al., 2019).

1.4. Vis/NIR hyperspectral imaging and quality attributes of fruits

HSI techniques in the Vis/NIR range, originally developed for remote sensing, have later spread mainly to the agri-food, material science and pharmaceutical sectors. In agri-food sector, these techniques are widely applied for grains, vegetables, and meat products (Chandrasekaran et al., 2019). Compared to traditional 'point' NIR spectroscopy, HSI provides spatial information, allowing for example the mapping of target attributes. HSI is therefore promising for the development of new, fast, and cost-effective non-destructive techniques for quality assessments of fruits.

Since HSI is based on Vis/NIR spectroscopy, both will present the same absorbance bands. For fruit analyses, the visible/short wave NIR region (Vis/SWNIR, 400–1100 nm) appears relevant. Data in the visible spectral range (400–750 nm) can be used to

assess external features such as colour, shape, size, defects, and faecal contamination (Liu et al., 2015; Chandrasekaran et al., 2019). The visible spectrum includes the absorption bands of some substances used as fruit maturity indices: carotenes and xanthophylls absorb at 420–500 nm (Walsh et al., 2020), and up to 600 nm (Munera et al., 2017), with beta-carotene close to 475 nm (Walsh et al., 2020); anthocyanins absorb at around 500 nm (ElMasry et al., 2007), up to 530–550 nm for an anthocyanin pigment sugar-protein complex in apples; chlorophyll absorbs at 670–720 nm (Walsh et al., 2020). In the SWNIR region (750–1100 nm), water absorption bands are localised at 760 nm and 960–970 nm, and are characterised by overtone of O–H bonds (McGlone & Kawano, 1998; Nicolaï et al., 2007). The absorption band at about 840 nm has been associated with sugar (Pu et al., 2016). Finally, the peaks observed in the 950–1000 nm region were related to both water and carbohydrates, as the second overtone of the O–H and N–H bonds, a combination band of the O–H bond, and the third overtone of the C–H bond were detected in the aforementioned region (Camps & Christen, 2009).

Since the water content of a fruit is about 74–90% (Salunkhe & Kadam, 1995), the water-related absorption band can be expected to prevail. As observed, the water absorption peaks in the SWNIR region are not very marked and broad. Therefore, the SSC spectral information in the 800–1000 nm range will tend to be less covered by water (Camps & Christen, 2009; Manley et al., 2007). However, the SWNIR assessment of macro-constituents such as SSC and dry matter content could be strongly dependent on a negative correlation with water (Walsh et al., 2020). Wavelengths > 1100 nm result in narrower and stronger absorption peaks than those observed in SWNIR, and therefore provide superior performance in the assessment of internal fruit quality attributes compared to those obtained in SWNIR. However, the SWNIR region is preferred to the region with wavelengths > 1100 nm, as the relatively low water absorption coefficient in the SWNIR region allows for deeper light penetration into the fruit. The lower effective penetration depth associated with the use of longer wavelengths could limit the robustness of the performance between independent populations, given the variation in quality attributes of the outer fruit layer (Walsh et al., 2020).

1.5. Operating principles of a hyperspectral camera

A typical HSI lab-scale system consists of a hyperspectral camera equipped with a charge-coupled device (CCD) or complementary metal-oxide semiconductor (CMOS) sensor and spectrograph, a light source that illuminates the sample, usually a conveyor

belt on which the sample flows, and a computer (ElMasry et al., 2012). The hyperspectral camera, similar to a RGB camera, measures and stores the light reflected from the sample. The RGB camera sensor measures only three bands of visible radiation (corresponding to the wavelengths of red, green, and blue light), whereas the hyperspectral camera sensor can measure several hundred wavelength bands in its characteristic spectral range. HSI systems are characterised by high spectral resolution, due to the width of the spectral bands, which is just a few nanometres (nm) (Thomas et al., 2018). Broadband light dispersion in wavelength bands is performed by optical and electro-optical devices (Liu et al., 2015).

1.6. Sensor types in hyperspectral imaging

In HSI systems, three types of sensors are implemented: (1) linear array 'whisk-broom' type with a rotating mirror, (2) linear array 'push-broom' type, (3) and area array. Linear array sensors are based on diodes or CCDs measuring radiance from the sample. Linear array push-broom sensors have some advantages over whisk-broom: they provide a more accurate measurement of the radiant flux from the sample, since no moving mirrors are required; moreover, given the same hyperspectral image acquisition time, the exposure time of the same part of the sample (*e.g.*, a push-broom scan line) is longer. Push-broom sensors take their name from the disposition of the pixel sensor units, which is similar to a line of bristles in a broom (Jensen, 2014). Since a push-broom hyperspectral camera can collect only one line of the sample surface at a time, a conveyor belt is normally used to slide the sample under the lens: therefore, an entire scan of the sample can be captured. Finally, the computer will compose and visualize the whole hyperspectral image (Liu et al., 2015). In case of area array sensors, hyperspectral images are fully captured in a single run: this system does not require movement of the sample or the hyperspectral camera. A filter, either wheel or tuneable, is required to select different wavelengths during the scanning process (ElMasry et al., 2012). The area array sensors are more practical in multispectral imaging, where the number of wavelengths selected is limited (Garini et al., 2006).

1.7. The hyperspectral data

Hyperspectral data consist of volume elements, the voxels, which contain reflectance, absorbance, or transmittance information of each wavelength band of a given spectral range. The spectral signature (or spectral profile) of each point in the hyperspectral

image can be obtained by combining this information; otherwise, the spectral signature can also be measured by a non-imaging hyperspectral system such as a spectrometer, but spatial information would be lost (Thomas et al., 2018). HSI, combining spectroscopy and imaging, measures the spectral signatures and spatial information of a sample at the same time. The output of the hyperspectral data is a stack of narrowband images organised along the spectrum axis, thus generating a 3D hypercube. The hypercube data, the voxels (values on a regular grid in a 3D space), are thus characterised by two spatial dimensions (x, y) and one spectral dimension (λ) (Fig. 1.7.1) (Mishra et al., 2017).

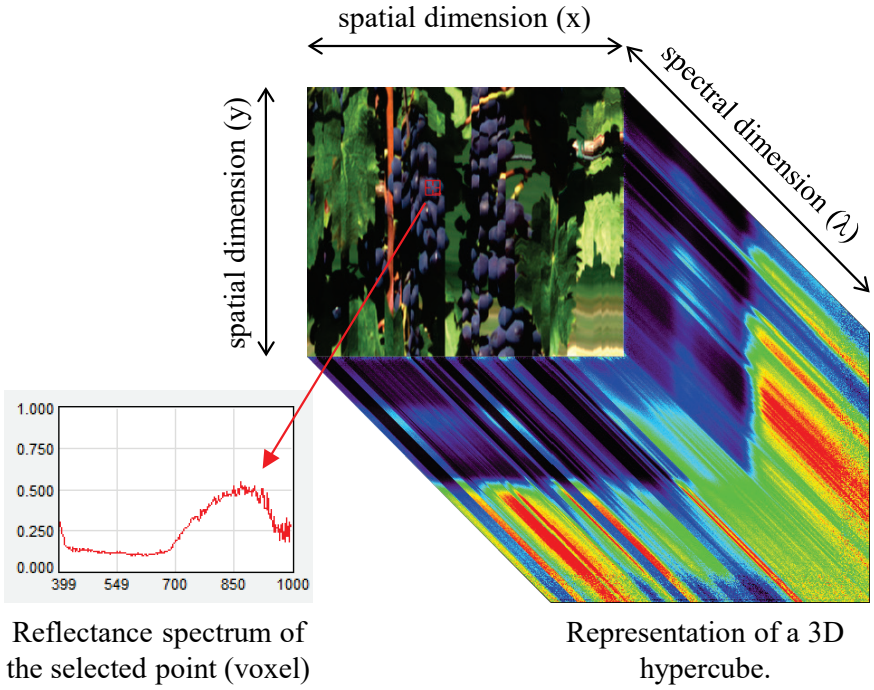

Fig. 1.7.1 – Representation of a 3D hypercube. The hypercube consists of two spatial dimensions (in the figure a RGB representation of a portion of a hyperspectral image of a vineyard section) and a spectral dimension (in the figure in false colours). Each point (voxel) identified in the spatial dimensions is characterised by a spectrum (in the figure a reflectance spectrum).

1.8. Hyperspectral image processing

The whole analytical process of a hyperspectral image can be summarised in three steps: (1) acquisition and calibration of the hyperspectral image; (2) spectral/spatial processing and dimensionality reduction; (3) hyperspectral data processing and development of prediction or classification models (Fig. 1.8.1). In recent years, several hyperspectral image processing techniques in both spectral and spatial dimensions

have been developed, based on chemometric and multivariate analysis. By reducing the dimensionality of the hyperspectral image through the extraction of useful spectral/spatial features, a smaller dimensional space is obtained compared to the original, thus reducing the amount of hyperspectral data. Finally, chemometric and multivariate analysis techniques can be applied on hyperspectral data to estimate a reference parameter (Yoon & Park, 2015).

1.8.1. Hyperspectral image acquisition and calibration

Following the acquisition of the hyperspectral image, a correction is applied to the hyperspectral image through black and white references. The black reference can be obtained by acquiring a hyperspectral image with the cap on the hyperspectral camera lens; the acquisition of the white reference requires the framing of a dedicated high reflectance white panel placed within the field of view of the hyperspectral camera (Ma et al., 2019).

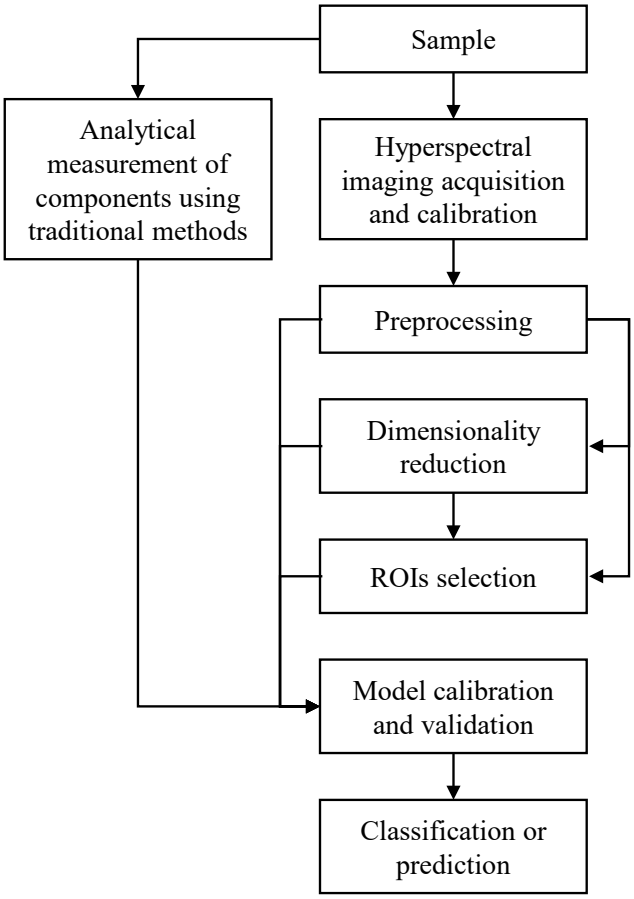

Fig. 1.8.1 – Common steps in hyperspectral imaging: process operations and data analysis. Note: ROIs, regions of interest.

1.8.2. Spectral/spatial processing and dimensionality reduction

Spectral processing, a key step at this stage, includes preprocessing and extraction of spectral features. The most commonly adopted preprocessing techniques include: spectral noise smoothing methods, such as Savitzky-Golay, moving average, median filter; algorithms to refine spectral data, such as derivatives (Norris-Williams and Savitzky-Golay), multiplicative scatter correction (MSC), standard normal variate (SNV); alignment techniques such as correlation optimised warping (COW) (Rinnan et al., 2009; Ma et al., 2019).

To overcome multicollinearity in multivariate analysis, it could be worthwhile to perform variable selection, identifying and removing unnecessary, noisy, and redundant variables. In addition, the dimensionality of the hyperspectral data could be also reduced, which may result in improved model features and performance, helping to simplify further classification and information retrieval processes (Liu et al., 2014). Variable selection methods can be classified as: (1) filter methods, including information gain and correlation-based feature selection (CFS), (2) wrapper methods, including learning algorithms, such as beam search, simulated annealing (SA), and genetic algorithms (GA), and (3) embedded methods, such as support vector machine (SVM) and decision trees. If the variables are wavelengths, as in the case of HSI, common variable selection methods include successive projections algorithm (SPA), stepwise regression (SWR), partial least square regression (PLSR), uninformative variable elimination (UVE), artificial neural network (ANN), SA, GA, competitive adaptive reweighted sampling (CARS), receiver operating characteristic (ROC) analysis, branch and bound (BB) algorithm, and minimum redundancy-maximum relevance (MRMR) (Liu et al., 2014).

1.8.3. Classification and prediction methods

The last stage of HSI processing is related to the development of classification or prediction models. Classification methods based on multivariate classification techniques include: (1) unsupervised methods such as principal component analysis (PCA), clustering (k-means, Jarvis-Patrick, hierarchical), and convolutional neural networks (CNN); (2) supervised methods such as discriminant analysis (linear, quadratic, or regularized DA), soft independent modelling class analogies (SIMCA), partial least squares discriminant analysis (PLS-DA), SVM, and non-parametric k-nearest neighbour (kNN) (Ma et al., 2019). Methods for developing prediction models used to estimate the correlation between spectral information and reference properties measured on samples are divided into linear and non-linear regression. Linear regression methods include multiple linear regression (MLR), principal component

regression (PCR) and PLSR. The most commonly used non-linear regression methods are ANN, such as multilayer perceptron (MLP) or generalised regression neural network (GRNN), SVM and non-linear PLSR (Ma et al., 2019).

1.9. References

Adebayo, S. E., Hashim, N., Abdan, K., & Hanafi, M. (2016). Application and potential of backscattering imaging techniques in agricultural and food processing – A review. *Journal of Food Engineering*, *169*, 155–164. https://doi.org/10.1016/j.jfoodeng.2015.08.006

Camps, C., & Christen, D. (2009). Non-destructive assessment of apricot fruit quality by portable visible-near infrared spectroscopy. *LWT - Food Science and Technology*, *42*(6), 1125–1131. https://doi.org/10.1016/j.lwt.2009.01.015

Chandrasekaran, I., Panigrahi, S. S., Ravikanth, L., & Singh, C. B. (2019). Potential of Near-Infrared (NIR) Spectroscopy and Hyperspectral Imaging for Quality and Safety Assessment of Fruits: an Overview. *Food Analytical Methods*, *12*(11), 2438–2458. https://doi.org/10.1007/S12161-019-01609-1

Delwiche, S. R. (2015). Basics of Spectroscopic Analysis. In B. Park & R. Lu (Eds.), *Hyperspectral Imaging Technology in Food and Agriculture. Food Engineering Series* (pp. 57–79). Springer. https://doi.org/10.1007/978-1-4939-2836-1_3

ElMasry, G., Kamruzzaman, M., Sun, D.-W., & Allen, P. (2012). Principles and Applications of Hyperspectral Imaging in Quality Evaluation of Agro-Food Products: A Review. *Critical Reviews in Food Science and Nutrition*, *52*(11), 999–1023. https://doi.org/10.1080/10408398.2010.543495

ElMasry, G., & Sun, D. W. (2010). Principles of Hyperspectral Imaging Technology. In *Hyperspectral Imaging for Food Quality Analysis and Control* (pp. 3–43). Academic Press. https://doi.org/10.1016/B978-0-12-374753-2.10001-2

ElMasry, G., Wang, N., ElSayed, A., & Ngadi, M. (2007). Hyperspectral imaging for nondestructive determination of some quality attributes for strawberry. *Journal of Food Engineering*, *81*(1), 98–107. https://doi.org/10.1016/j.jfoodeng.2006.10.016

Garini, Y., Young, I. T., & McNamara, G. (2006). Spectral imaging: Principles and applications. *Cytometry Part A*, *69A*(8), 735–747. https://doi.org/10.1002/cyto.a.20311

Goetz, A., Vane, G., Solomon, J., & Rock, B. (1985). Imaging Spectrometry for Earth Remote Sensing. *Science*, *228*(4704), 1147–1153. https://doi.org/10.1126/science.228.4704.1147

Hussain, A., Pu, H., & Sun, D.-W. (2018). Innovative nondestructive imaging techniques for ripening and maturity of fruits – A review of recent applications. *Trends in Food Science & Technology*, *72*, 144–152. https://doi.org/10.1016/j.tifs.2017.12.010

Jensen, J. R. (2014). Multispectral Remote Sensing Systems. In J. R. Jensen (Ed.), *Remote Sensing of the Environment: An Earth Resource Perspective* (2nd ed., pp. 177–242). Pearson Education Limited.

Liu, D., Sun, D.-W., & Zeng, X.-A. (2014). Recent Advances in Wavelength Selection Techniques for Hyperspectral Image Processing in the Food Industry. *Food and Bioprocess Technology*, *7*(2), 307–323. https://doi.org/10.1007/s11947-013-1193-6

Liu, D., Zeng, X.-A., & Sun, D.-W. (2015). Recent Developments and Applications of Hyperspectral Imaging for Quality Evaluation of Agricultural Products: A Review. *Critical Reviews in Food Science and Nutrition*, *55*(12), 1744–1757. https://doi.org/10.1080/10408398.2013.777020

Lu, R., & Park, B. (2015). Introduction. In B. Park & R. Lu (Eds.), *Hyperspectral Imaging Technology in Food and Agriculture. Food Engineering Series* (pp. 3–7). Springer. https://doi.org/10.1007/978-1-4939-2836-1_1

Ma, J., Sun, D.-W., Pu, H., Cheng, J.-H., & Wei, Q. (2019). Advanced Techniques for Hyperspectral Imaging in the Food Industry: Principles and Recent Applications. *Annual Review of Food Science and Technology*, *10*(1), 197–220. https://doi.org/10.1146/annurev-food-032818-121155

Manley, M., Joubert, E., Myburgh, L., Lotz, E., & Kidd, M. (2007). Prediction of soluble solids sontent and post-storage internal quality of Bulida apricots using near infrared spectroscopy. *Journal of Near Infrared Spectroscopy*, *15*(3), 179–188. https://doi.org/10.1255/jnirs.725

McGlone, V. A., & Kawano, S. (1998). Firmness, dry-matter and soluble-solids assessment of postharvest kiwifruit by NIR spectroscopy. *Postharvest Biology and Technology*, *13*(2), 131–141. https://doi.org/10.1016/S0925-5214(98)00007-6

Mishra, P., Asaari, M. S. M., Herrero-Langreo, A., Lohumi, S., Diezma, B., & Scheunders, P. (2017). Close range hyperspectral imaging of plants: A review. *Biosystems Engineering*, *164*, 49–67. https://doi.org/10.1016//j.biosystemseng.2017.09.009

Mollazade, K., Omid, M., Tab, F. A., & Mohtasebi, S. S. (2012). Principles and Applications of Light Backscattering Imaging in Quality Evaluation of Agro-food Products: a Review. *Food and Bioprocess Technology*, *5*(5), 1465–1485. https://doi.org/10.1007/s11947-012-0821-x

Mosca, S., Conti, C., Stone, N., & Matousek, P. (2021). Spatially offset Raman spectroscopy. *Nature Reviews Methods Primers*, *1*(21), 1–16. https://doi.org/10.1038/s43586-021-00019-0

Munera, S., Amigo, J. M., Blasco, J., Cubero, S., Talens, P., & Aleixos, N. (2017). Ripeness monitoring of two cultivars of nectarine using VIS-NIR hyperspectral reflectance imaging. *Journal of Food Engineering*, *214*, 29–39. https://doi.org/10.1016/J.JFOODENG.2017.06.031

Nicolaï, B. M., Beullens, K., Bobelyn, E., Peirs, A., Saeys, W., Theron, K. I., & Lammertyn, J. (2007). Nondestructive measurement of fruit and vegetable quality by means of NIR spectroscopy: A review. *Postharvest Biology and Technology*, *46*(2), 99–118. https://doi.org/10.1016/j.postharvbio.2007.06.024

Pathmanaban, P., Gnanavel, B. K., & Anandan, S. S. (2019). Recent application of imaging techniques for fruit quality assessment. *Trends in Food Science & Technology*, *94*, 32–42. https://doi.org/10.1016/j.tifs.2019.10.004

Pu, H., Liu, D., Wang, L., & Sun, D.-W. (2016). Soluble Solids Content and pH Prediction and Maturity Discrimination of Lychee Fruits Using Visible and Near Infrared Hyperspectral Imaging. *Food Analytical Methods*, *9*(1), 235–244. https://doi.org/10.1007/S12161-015-0186-7

Rinnan, Å., van den Berg, F., & Engelsen, S. B. (2009). Review of the most common pre-processing techniques for near-infrared spectra. *TrAC Trends in Analytical Chemistry*, *28*(10), 1201–1222. https://doi.org/10.1016/j.trac.2009.07.007

Ruiz-Altisent, M., Ruiz-Garcia, L., Moreda, G. P., Lu, R., Hernandez-Sanchez, N., Correa, E. C., Diezma, B., Nicolaï, B., & García-Ramos, J. (2010). Sensors for product characterization and quality of specialty crops—A review. *Computers and Electronics in Agriculture*, *74*(2), 176–194. https://doi.org/10.1016/j.compag.2010.07.002

Salunkhe, D. K., & Kadam, S. S. (1995). Introduction. In D. K. Salunkhe & S. S. Kadam (Eds.), *Handbook of Fruit Science and Technology* (1st ed., pp. 1–6). CRC Press. https://doi.org/10.1201/9781482273458-8

Sikorska, E., Khmelinskii, I., & Sikorski, M. (2019). Fluorescence spectroscopy and imaging instruments for food quality evaluation. In J. Zhong & X. Wang (Eds.), *Evaluation Technologies for Food Quality. Food Science, Technology and Nutrition Series* (pp. 491–533). Woodhead Publishing. https://doi.org/10.1016/B978-0-12-814217-2.00019-6

Thomas, S., Kuska, M. T., Bohnenkamp, D., Brugger, A., Alisaac, E., Wahabzada, M., Behmann, J., & Mahlein, A. K. (2018). Benefits of hyperspectral imaging for plant disease detection and plant protection: a technical perspective. *Journal of Plant Diseases and Protection*, *125*(1), 5–20. https://doi.org/10.1007/s41348-017-0124-6

Walsh, K. B., Blasco, J., Zude-Sasse, M., & Sun, X. (2020). Visible-NIR 'point' spectroscopy in postharvest fruit and vegetable assessment: The science behind three decades of commercial use. *Postharvest Biology and Technology*, *168*, 111246. https://doi.org/10.1016/j.postharvbio.2020.111246

Yoon, S. C., & Park, B. (2015). Hyperspectral Image Processing Methods. In B. Park & R. Lu (Eds.), *Hyperspectral Imaging Technology in Food and Agriculture. Food Engineering Series* (pp. 81–101). Springer. https://doi.org/10.1007/978-1-4939-2836-1_4

Zhang, Z. (2017). Raman Spectroscopic Sensing in Food Safety and Quality Analysis. In X. Lu (Ed.), *Sensing Techniques for Food Safety and Quality Control. Food Chemistry, Function and Analysis Series* (pp. 1–16). Royal Society of Chemistry. https://doi.org/10.1039/9781788010528-00001

2. EXPERIMENTAL SECTION

This section, organized into two parts, introduces the research activity with brief abstracts of the studies carried out.

The first part concerns studies from activities carried out in the laboratory: first, two studies on the application of hyperspectral imaging technology for the determination of quality attributes of apricots and kiwis; then, the application of an optical method for the estimation of procyanidins in red wine; finally, a study on the determination of kiwi hardness using a near-infrared (NIR) sensitive device.

In the second part, studies on activities carried out directly in the field using hyperspectral imaging (HSI) technology are reported: as an introduction to the topic, a review on in-field HSI systems for ground-based proximal sensing has been included, followed by a study on the monitoring of wine grape ripening and finally a study on the automatic selection of regions of interest from hyperspectral images.

2.1. Lab-scale studies by hyperspectral imaging technology and other optical techniques

The fruit industry needs fast, non-destructive and inexpensive techniques to monitor the quality of produce in the post-harvest and storage phases, to identify the proper degree of ripeness for distribution, or to assess shelf-life. In the following studies, the soluble solids content (SSC) and flesh firmness (FF) of apricots (Benelli et al., 2022, under review) and kiwis (Benelli et al., 2021a) were monitored as quality attributes related to the ripeness of the fruit using a HSI lab-scale system.

Then, a study based on a rapid and cost-effective optical method for the determination of procyanidins in red wine is introduced (Ricci et al., 2020). Finally, a brief description of a study involving the application of a sensitive NIR device, with potential in on-line sorting, for the determination of kiwi flesh firmness is reported (Berardinelli et al., 2019).

2.1.1. Hyperspectral imaging to measure apricot attributes during storage (Benelli et al., 2022, accepted for publication) – Paper I

The purpose of the present study was to provide a prediction of the FF and SSC of apricots during storage. A HSI lab-scale system operating in the visible/near-infrared (Vis/NIR) spectral region (400–1000 nm) was used to scan 180 'Farbaly' apricots over 11 days. Partial least square (PLS) regression and artificial neural network (ANN) were used to develop predictive models. From the PLS models, the best results were obtained for the prediction of FF, with R^2_P=0.854 and RMSEP=1.64 N, while R^2_P=0.721 and RMSEP=0.51 °Brix were obtained for the prediction of SSC. From the ANN models, the best results were obtained for the prediction of FF, with R^2_P=0.85 and RMSEP=1.50 N. Accordingly to these results, the study also revealed the potential of the HSI technique for assessing quality attributes of apricots along the supply-chain.

2.1.2. Ripeness evaluation of kiwifruit by hyperspectral imaging (Benelli, et al., 2021a) – Paper II

In the present study, a Vis/NIR (400–1000 nm) hyperspectral imaging lab-scale system was adopted to assess the ripeness of 'Hayward' kiwifruit. PLS models were developed to predict SSC and FF, while two types of partial least square discriminant analysis (PLS-DA), soft and hard, were used to classify samples according to three ripeness classes (unripe, ripe for storage, ripe for consumer), defined according to ranges of SSC and FF values. To reduce the dimensionality of the hyperspectral data, two methods of variable selection were adopted: genetic algorithm (GA) and variable importance in projection (VIP). The results of the SSC prediction ranged from R^2_P values of 0.85 (RMSEP=1.10 °Brix) to 0.94 (RMSEP=0.73 °Brix), while with the FF prediction, R^2_P values from 0.82 (RMSEP=14.51 N) to 0.92 (RMSEP=9.87 N) were obtained. The classification sensitivity reached values of 97% for SSC and 93% for FF models. Prediction and classification performance remained essentially unchanged by reducing the dimensionality of the hyperspectral data through variable selection. Therefore, hyperspectral imaging appears suitable for prediction of kiwifruit quality attributes and classification of kiwifruit into the three classes unripe, ripe for storage, ripe for consumer, defined considering quality attributes.

2.1.3. Rapid optical method for procyanidins estimation in red wines (Ricci et al., 2020) – Paper III

This work describes a reliable and rapid optical method for estimation of tannin content in red wines. The method draws from the ability of tannins to precipitate

proteins from aqueous solutions. The mixing of wine tannins (procyanidins) with gelatine forms a delicate meshwork that sweeps colloidal proteins out of wine (Jackson, 2020). An optical device based on the spectral-sensitive pulsed photometry (SSPP) technique (Ragni et al., 2016) was used to assess the degree of turbidity by measuring the light intensity of a pulsed light source (tungsten lamp) with a wavelength-sensitive photodiode. Twenty-seven red wines were optically measured at room temperature immediately after mixing with a saturated gelatine solution in a model wine buffer (12% ethanol, pH 3.5). The resulting output signal waveform (voltage, V) presents different peak intensity, amplitude, and curvature values as a function of the degree of turbidity and radiation absorption. A significant nonlinear correlation (R^2 up to 0.9657) with tannin content, determined by a reference colorimetric method, was obtained. Hence, the proposed new optical method represents a reliable, rapid, simple, and cost-effective alternative for on-line and off-line analysis of procyanidins in red wine.

2.1.4. Kiwifruit flesh firmness determination by a NIR sensitive device and image multivariate data analyses (Berardinelli et al., 2019) – Paper IV

A prototype based on a NIR-sensitive camera and a xenon lamp was set up and used to capture 8-bit greyscale images (0=black to 255=white) of the radiation passing through kiwifruits. Grey tones and pixel counts were used to build statistical-mathematical models to correlate and predict the FF of the fruit. One hundred and sixteen properly stored fruits (FF range: 0.8–87 N) were subjected to the optical measurements. Simple regression between the prevailing grey tone (the grey tone with the most pixels) and FF revealed an exponential correlation (R^2=0.717). Instead, tone uniformity (the number of pixels of the prevailing grey tone) resulted linearly correlated to FF (R^2=0.687). The PLS algorithm was able to predict FF with R^2=0.777 (RMSE=13 N). ANNs produced similar results. Although the current technique does not fully meet the requirements for accurate selection, it could be considered for on-line applications by improving performance (*e.g.*, acting on lamp spectral emissions and camera detection) and with easy mechanical modifications of the sorting lines (Berardinelli et al., 2019).

2.2. Studies on in-field hyperspectral imaging systems

In the agro-food sector, a large number of works have been published on the use of HSI technology under controlled laboratory conditions. However, studies concerning the application of HSI technology directly in the field, in particular through ground-based systems, are less common. Therefore, an overview of the application of HSI technology directly in the field, considering ground-based systems, has been proposed (Benelli et al., 2020). Afterwards, two studies on the monitoring of the ripening process of wine grapes, from post-veraison to harvest, are reported (Benelli et al., 2021b); hyperspectral images were acquired by a HSI system mounted on a ground-based vehicle.

2.2.1. In-field hyperspectral imaging: an overview on the ground-based applications in agriculture (Benelli et al., 2020) – Paper V

Monitoring vegetation indices that characterise plant health and growth, or the assessment of fruit maturity, defects, and diseases, are key steps to gain high quality products. HSI could fulfil these demands providing a good basis for research and development of fast, cost-effective, and non-destructive systems for direct in-field monitoring of crop production. In this context, the studies reviewed and reported concern in-field applications of ground-based HSI systems, such as high-throughput phenotyping of different types of cereals, vines and cotton, mango ripening, chlorophyll and nitrogen content of cereals, sugar beet and mosses, water stress detection of cereals, weed detection and management, monitoring of corn stubbles in conservation agriculture, monitoring of wheat canopies under uncontrolled conditions.

2.2.2. In-field and non-destructive monitoring of grapes maturity by hyperspectral imaging (Benelli et al., 2021b) – Paper VI

The study describes the development of a rapid, non-destructive method for in-field monitoring of the ripening of ‘Sangiovese’ wine grapes with a HSI Vis/NIR (400–1000 nm) system mounted on a ground-based vehicle. A vineyard row divided into 11 sections was analysed on 13 different days under clear sky conditions between post-veraison and harvest. The analysis focused on the monitoring of SSC. The °Brix of the grapes was measured directly in the field with a portable digital refractometer. Mean spectra of the grapes were extracted from the hyperspectral images of the vineyard sections and used to predict SSC by PLS regression. Afterwards, the grape samples were divided into two classes: the first with °Brix<20 (not-ripe) and the second with °Brix≥20 (ripe). Mean spectra of the grapes were then classified by PLS-DA. SSC was

predicted with R^2_{CV}=0.77 (RMSECV=0.79 °Brix), and samples were correctly classified with a percentage ranging from 86 to 91%. By performing variable selection, the percentages of correctly classified samples fell into the same range. The study highlights the potential of HSI technology for proximal sensing applied directly in the field under daylight conditions to predict grape maturity and harvest time.

2.2.3. Automatic selection of the regions of interest from moving wagon hyperspectral images of grapes and SSC prediction

In the present study, the development process of a method for automatic selection of regions of interest (ROIs) from hyperspectral images was described. For this purpose, the whole dataset from Benelli et al. (2021b) was used, consisting of hyperspectral images of a row of 'Sangiovese' wine grapes acquired directly in the field by means of an HSI Vis/NIR system (400–1000 nm) mounted on a ground-based vehicle. The analyses were carried out on 17 different days, under clear or partly cloudy conditions, in the period between post-veraison and harvest. The vineyard row was divided into 11 sections and a hyperspectral image for each section for each day of analysis was acquired. The ROIs of the hyperspectral images, comprising the areas covered by grapes, were predicted using a PLS-DA-based method. The best PLS-DA model provided excellent results, with sensitivity and specificity values of 0.991 and 0.996, respectively. The mean spectra of the selected ROIs were then used to predict the SSC of grapes by PLS regression. The best results of SSC prediction (R^2_{CV}=0.74 and RMSECV=0.86 °Brix) agree with those obtained by manual ROIs selection (R^2_{CV}=0.73 and RMSECV=0.87 °Brix).

2.3. References

Benelli, A., Cevoli, C., & Fabbri, A. (2020). In-field hyperspectral imaging: An overview on the ground-based applications in agriculture. *Journal of Agricultural Engineering*, *LI*:1030, 129–139. https://doi.org/10.4081/jae.2020.1030

Benelli, A., Cevoli, C., Fabbri, A., & Ragni, L. (2021a). Ripeness evaluation of kiwifruit by hyperspectral imaging. *Biosystems Engineering*. https://doi.org/10.1016/j.biosystemseng.2021.08.009

Benelli, A., Cevoli, C., Ragni, L., & Fabbri, A. (2021b). In-field and non-destructive monitoring of grapes maturity by hyperspectral imaging. *Biosystems Engineering*, *207*, 59–67. https://doi.org/10.1016/j.biosystemseng.2021.04.006

Berardinelli, A., Benelli, A., Tartagni, M., & Ragni, L. (2019). Kiwifruit flesh firmness determination by a NIR sensitive device and image multivariate data analyses. *Sensors and Actuators A: Physical*, *296*, 265–271. https://doi.org/10.1016/j.sna.2019.07.027

Jackson, R. S. (2020). Postfermentation treatments and related topics. In *Wine Science: Principles and Applications* (5th ed., pp. 573–723). Academic Press. https://doi.org/10.1016/B978-0-12-816118-0.00008-8

Ragni, L., Iaccheri, E., Cevoli, C., & Berardinelli, A. (2016). Spectral-sensitive Pulsed Photometry to predict the fat content of commercialized milk. *Journal of Food Engineering*, *171*, 95–101. https://doi.org/10.1016/j.jfoodeng.2015.10.017

Ricci, A., Iaccheri, E., Benelli, A., Parpinello, G. P., Versari, A., & Ragni, L. (2020). Rapid optical method for procyanidins estimation in red wines. *Food Control*, *118*, 107439. https://doi.org/10.1016/j.foodcont.2020.107439

3. RESEARCH OUTCOMES

3.1. Hyperspectral imaging to measure apricot attributes during storage

Scientific publication – Paper I

Benelli, A., Cevoli, C., Fabbri, A., & Ragni, L. (2022). Hyperspectral imaging to measure apricot attributes during storage. *Journal of Agricultural Engineering.* Accepted for publication on April 15th, 2022

Alessandro Benelli[a], Chiara Cevoli[a,b,*], Angelo Fabbri[a,b], Luigi Ragni[a,b]

[a]*Department of Agricultural and Food Sciences, Alma Mater Studiorum, University of Bologna, Piazza Goidanich 60, Cesena, 47521, Italy*

[b]*Interdepartmental Centre for Agri-Food Industrial Research, Alma Mater Studiorum, University of Bologna, Via Quinto Bucci 336, Cesena, 47521, Italy*

[*]*Corresponding author: chiara.cevoli3@unibo.it*

Abstract

Fruit industry needs for rapid and non-destructive techniques to evaluate the products quality in field and during the post-harvest phase. The soluble solids content (SSC), in terms of °Brix, and the flesh firmness (FF) are typical parameters used to measure fruit quality and maturity state. Hyperspectral imaging (HSI) is a powerful technique, combining image analysis and infrared spectroscopy. The aim of this study was to evaluate the potential of application of the Vis/NIR push-broom hyperspectral imaging (400 to 1000 nm) to predict the firmness and the °Brix in apricots (180 samples) during storage (11 days). Partial least squares (PLS) and artificial neural networks (ANN) were used to develop predictive models. For the PLS, R^2 values (test set) up to 0.85 (RMSEP=1.64 N) and 0.72 (RMSEP=0.51 °Brix) were obtained for the FF and SSC, respectively. Concerning the ANN, the best results, in test set, was achieved for the FF (R^2=0.85, RMSEP=1.50 N). The study showed the potential of the HSI technique as a non-destructive tool for measuring apricot quality even along the whole supply chain.

Keywords: apricot, storage, hyperspectral imaging, ANN, PLS.

3.1.1. Introduction

The optimal harvest time or the right degree of ripeness of apricots (*Prunus Armeniaca* L.) intended for the fresh market are typically determined by measuring chemical and physical quality parameters of the fruit, i.e., the ripening indexes. The measurement of the quality parameters of the fruit is traditionally carried out using destructive analytical techniques, which also involve long operating times (Witherspoon & Jackson, 1995). In the last decades, numerous researches have been addressed on the fast and non-destructive estimation of fruit ripening indexes through spectroscopic methods, including near- and mid-infrared spectroscopy (NIR/MIR); in particular, for apricots, have been analysed: soluble solids content (SSC), titratable acidity (TA), flesh firmness (FF), total carotenoids content (TCC), total phenolic content (TPC) and flavonols content (FLC) (Amoriello et al., 2019; Guo et al., 2019; Amoriello et al., 2018; Bureau et al., 2018; Ciacciulli et al., 2018; Buyukcan & Kavdir, 2017; De Oliveira et al., 2014; Bureau et al., 2012; Christen et al., 2012; Berardinelli et al., 2010; Bureau et al., 2009; Camps & Christen, 2009b; Camps & Christen, 2009a; Ruiz et al., 2008; Manley et al., 2007; Carlini et al., 2000). Another spectroscopic technique that has been increasingly applied in the last decade for the determination of fruit and vegetable quality parameters is hyperspectral imaging (HSI). HSI combines image analysis and spectroscopy, in particular Vis/NIR spectroscopy. HSI allows to obtain as many absorbance/reflectance/transmittance spectra as there are single acquired pixels (in this technique called voxels) that form the hyperspectral image; the output is a hypercube, composed of data with two spatial and a spectral dimensions. This method of analysis is fast and non-destructive, without the need for contact with the sample to be analysed. HSI is applied for the determination of quality parameters of fruit and vegetables both directly in the field and in the laboratory. The processing of the acquired hyperspectral images generally requires several steps: the use of hyperspectral image segmentation techniques, in order to reduce the size of the acquired data; the application of a region of interest (ROI) selection method, from which the hyperspectral data required can be derived; finally, the application of spectra pre-treatment techniques for the implementation of multivariate data analysis. Partial least square regression (PLS), supporting vector machines (SVM) and artificial neural networks (ANN), are popular multivariate regression techniques used for hyperspectral imaging.

There are several studies on the determination of fruit quality parameters by means of HSI (Chandrasekaran et al., 2019), but there is only one study concerning apricots (Xue et al., 2015). The authors evaluated the ripeness of the *Shajin* apricot, in terms of 4 ripeness classes (unripe, mid-ripe, ripe, and over-ripe according to the days after harvesting) and SSC, by using the HSI in the band range of 400–1000 nm. Extreme learning machine (ELM) was used as classification technique. The results showed a correct discrimination rate of 93.33%, but regression models able to estimate the SSC have not been developed.

In this study, the potential of HSI technique combined with multivariate data analyses (PLS and ANN) to non-destructively predict quality parameters (SSC and FF) of apricots in post-harvest conditions was investigated. This would allow to assess the degree of ripeness of the fruit suitable for the fresh market.

3.1.2. Materials and methods

3.1.2.1. Samples

180 samples of apricot c.v. *Farbaly* harvested in July 2019 in the Cesena area (Italy) and stored at 4 °C were used for the research. The analyses were carried out after 1 (I), 2 (II), 3 (III), 4 (IV), 5 (V), 8 (VI), 9 (VII), 10 (VIII) and 11 (IX) days of storage at 20 °C, for a total of nine storage times. Twenty apricots for storage time were evaluated. These storage conditions have been chosen to reproduce those in the fresh market.

3.1.2.2. Hyperspectral measurements

The hyperspectral (HS) images of the apricots were obtained through the use of a push-broom linear array hyperspectral camera (HSC) working in the spectral range from 400 to 1000 nm (Nano-Hyperspec VNIR, Headwall Photonics, Inc., Fitchburg, MA, USA) with a 12 mm EFL (effective focal length) lens. The HSC scans one line of voxels at a time, with a spatial resolution of 640 points, each one characterized by 272 spectral bands, with a nominal spectral resolution of 2.2 nm. The HSC has been set with an exposure and frame period of 25 ms: the frame rate is a variable depending on the set exposure time, in this case it was 34.22 frames per second (FPS).

The set-up used during the experimental test is shown in Fig. 3.1.1. Particularly, the HSC has been mounted on a metallic frame with the optical axis perpendicular to the underlying conveyor belt, on which the sample runs, at a height of 54 cm. The conveyor belt speed has been set to 8 $mm \cdot s^{-1}$. On the same frame, two halogen spotlights with 120 W lamp have been mounted, inclined by 15° with respect to the conveyor belt plane and at a height of 32 cm. The analysis was carried out by isolating the apparatus from the external light using a properly assembled box. The

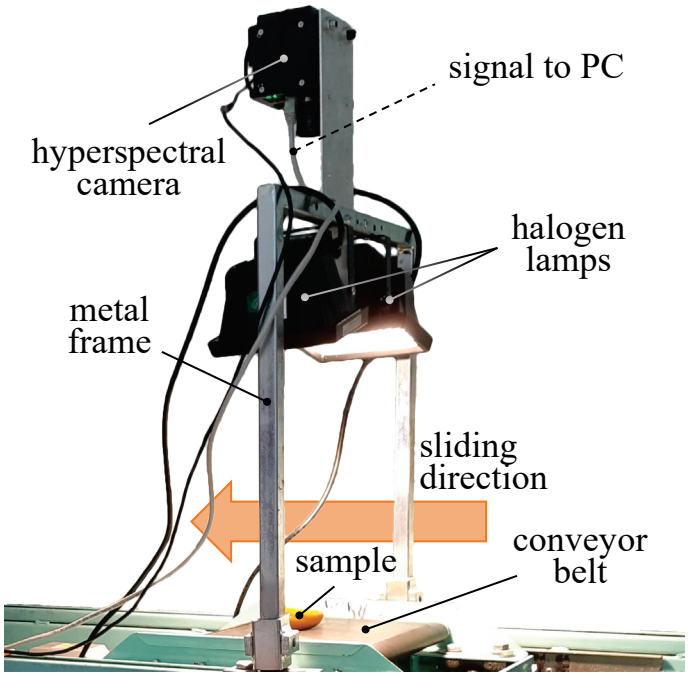

Fig. 3.1.1 – Components of the hyperspectral imaging system developed for the experiment.

hyperspectral image was obtained by progressive scanning of several lines, keeping the HSC fixed and running the sample on a prototype conveyor belt, which simulates an industrial fruit sorting line.

Reflectance spectrum of white reference (R_W) was obtained respectively by means of a white cardboard sheet covering the entire angle of view of the HSC; reflectance spectrum of dark reference (R_D) was obtained placing the cover on the lens. Raw diffuse reflectance spectrum (R_R) was obtained by the scan of the sample. The calibrated diffuse reflectance spectrum (R_C), was calculated by the following equation (Guo et al., 2019):

$$R_C = \frac{R_R - R_D}{R_W - R_D}$$

Each whole apricot was longitudinally scanned twice, one per side. The sample temperature was 23±1 °C.

3.1.2.3. Destructive measurements of quality parameters

The quality parameters (FF and SSC) were measured immediately after the acquisition of the HS images. The apricots were prepared for FF analysis by cutting them in half with a knife along the longitudinal plane, depriving them of the kernel, and finally removing the concavity resulting from the removal of the kernel, in order to obtain a flat support surface. FF (N) was determined on each half portion of the fruit on the equatorial area by a compression test performed with a texture analyser (TA-HDi,

Stable Micro System Ltd., Godalming, UK) during a penetration of 9 mm obtained by a 6 mm diameter flat-headed cylindrical steel probe mounted on a 50 N load cell. The test speed was 0.5 $mm \cdot s^{-1}$. The SSC (°Brix) was measured by means of a digital refractometer (PR-101 Digital Refractometer, ATAGO CO., LTD, Tokyo, Japan), on juice obtained from the pulp in the equatorial area of the fruit side previously analysed with the texture analyser (Witherspoon & Jackson, 1995). An average value of the ripening index was subsequently obtained by averaging the FF and °Brix grade values of the two sides of the fruit. Significant differences between the means of the quality parameters at different storage time were evaluated through analysis of variance (ANOVA with Tukey-HSD post-hoc test, p-level>0.05). In case of non-homogeneity of variance, evaluated by the Levene test, the non-parametric Kruskal-Wallis test (p-level<0.05) with multiple comparison z' post-hoc test (Dunn's test) was applied.

3.1.2.4. Multivariate data analysis

For each side of each sample, a mean spectrum was calculated by averaging the spectra of the region of interest (ROI), a selected equatorial area measuring 30×30 voxels (900 spectra). This operation was done by using HyperCube v. 11.52 software (U.S. Army Engineer Research and Development Center (ERDC), USA). The mean spectra of two sides were averaged and used for the chemometric elaborations. Principal component analysis (PCA) was used as explorative technique to evaluate the spectra variations and to identify sample outliers. Two different statistical techniques were used to predict SSC and FF, the first one (PLS) based on a linear approach, and the second one (ANN) on a non-linear approach. The dataset was split into two sub-sets, one to train and cross-validate the models (80% of the entire dataset) and the other (20%) to external validate it (test set), by using the Kennard-Stone method (selects samples that best span the same range as the original data, but with an even distribution of samples across the same range). The overfitting of the models was avoided monitoring the root mean square error in cross-validation (RMSECV) as a function of the latent variables (PLS) or iterations number (ANN). To identify and select relevant variables, variable importance in the projection (VIP) method was adopted. VIP scores estimate the relevance of each predictor in the projection used in a PLS model: since the mean of squared VIP scores is equal to 1, the 'greater than one' rule is frequently used as a variable selection criterion (Chong & Jun, 2005). Finally, the results were expressed in terms of R^2, root mean square error (RMSE) and residual prediction deviation (RPD), defined as the standard deviation of observed values divided by the RMSE: a good model should have a high R^2, a low RMSE and a high RPD.

PLS regression models were developed by using PLS Toolbox for Matlab2018a®. Spectral bands between 400 and 426 nm (13 spectral bands) and between 980 and 1000

nm (10 spectral bands) were excluded, due to the low signal-to-noise ratio generated by the hyperspectral sensor, as also observed by Wendel et al. (2018). The spectra were pre-treated with standard normal variate (SNV) or Savitzky-Golay first derivative (D1) transformation (10 points) and finally mean centred (MC), to improve the prediction performance.

The ANN models were performed by using the Neural Net Fitting tool for Matlab2018a®. Specifically, two Multi-Layer Perceptron (MLP) neural network were built to predict SSC and FF. For input and output layers, linear activation function was used, while for the hidden layer a logistic activation function was applied. Considering that the ANN ability should be to capture an implicit pre-processing of the spectra (Helin et al., 2022), the raw spectra were only subjected to denoising (Savitzky-Golay method with 15 smoothing points). Min-max normalization is independently applied by the software to speed up learning and leads to faster convergence.

Looking for the best classification ability, different node numbers in the hidden layer and combinations were tested. The ANN were trained by using the Levenberg-Marquardt back propagation method.

3.1.3. Results and discussion

Mean and standard deviation values of SSC and FF are shown in Table 3.1.1. The obtained values are in agreement with those reported by Ciacciulli et al. (2018), Berardinelli et al. (2010), and Manley et al. (2007) for apricots analysed during different days of storage. Significant differences emerged for both FF and SSC between measurements at different storage time.

Table 3.1.1 – Means and standard deviations (in brackets) of maturity indices (SSC and FF) as a function of storage time (n=20 for each storage time).

Storage time	SSC (°Brix)	FF (N)
I	15.0^{a} (1.0)	14.3^{a} (2.8)
II	$15.7^{a,b}$ (0.9)	13.0^{a} (3.4)
III	$16.5^{b,c}$ (1.4)	$10.2^{a,b}$ (1.7)
IV	$16.4^{b,c}$ (0.7)	$8.3^{a,b,c}$ (1.4)
V	$16.6^{b,c}$ (0.8)	$6.6^{b,c,d}$ (0.8)
VI	$16.6^{b,c}$ (0.6)	$4.0^{c,d,e}$ (0.4)
VII	17.0^{c} (0.8)	$3.5^{d,e}$ (0.6)
VIII	$16.5^{b,c}$ (0.7)	3.4^{e} (0.6)
IX	$16.4^{b,c}$ (0.9)	3.0^{e} (0.6)

Note: the differences between means with the same letter are not significant at $p<0.05$.

The range of variation of FF is rather high, with a decrease from day I to day IX of 79%. In the same time period SSC increased by 9%.

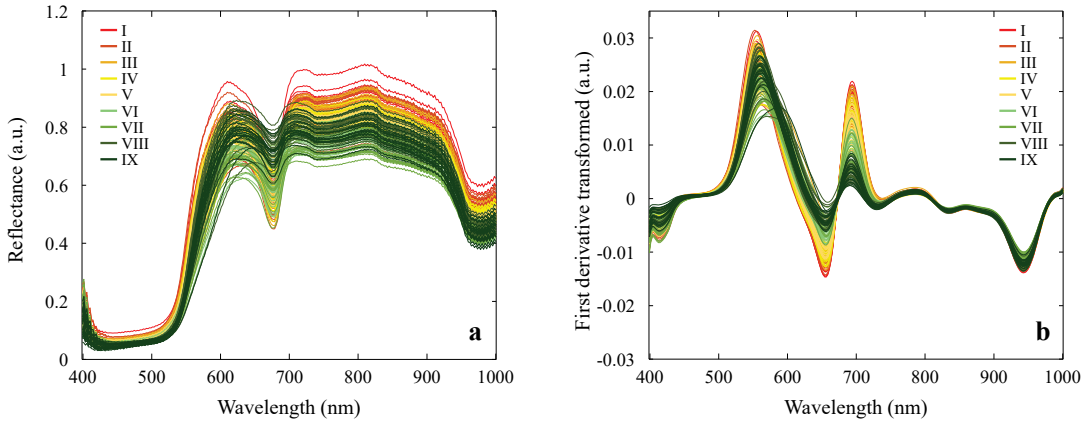

Fig. 3.1.2 – Raw (a) and first derivative (b) spectra of all samples on different days (from I to IX) of analysis.

Raw spectra and pre-treated spectra by the first derivative of all the samples by day of analysis are shown in Fig. 3.1.2. The Vis/NIR region from 400 to 1000 nm is characterized by vibration overtones and combination bands of O–H, C–H and N–H bonds, related to the principal structural organic molecules (Manley et al., 2007). In the visible spectrum (400–700 nm) are present the absorption bands of substances used as ripening indexes of fruit (Manley et al., 2007). The absorption band of anthocyanins is around 500 nm (ElMasry et al., 2007), the range of absorption bands related to carotenoids is between 570 and 590 nm (Munera et al., 2017), and between 680 and 710 nm for chlorophyll-α (Amoriello et al., 2018; Munera et al., 2017; Pu et al., 2016; ElMasry et al., 2007; McGlone & Kawano, 1998).

Absorption bands related to water with overtone of O–H bonds were observed at 760 nm (Nicolaï et al., 2007) and 970 nm (Bureau et al., 2009; Nicolaï et al., 2007). In accordance with the latter statement, a strong absorption band related to water was observed at around 960 nm (Guo et al., 2019; Pu et al., 2016; McGlone & Kawano, 1998), and can be expected to prevail, since the water content of the fresh fruit is 80–90% (McGlone & Kawano, 1998). In general, the water absorption peaks in the spectral region between 700 and 1000 nm are less marked and wide. Therefore, the spectral information from substances present in the fruit at low concentrations will tend to be less covered by the presence of water (Manley et al., 2007). Between 950 and 1000 nm, absorbance peaks were observed for carbohydrates and water, corresponding to the second overtone of O–H and N–H, a combination band of O–H bonds and the third overtone of C–H (Camps & Christen, 2009a). Absorption regions at 840 nm have been indicated as probable sugar absorption bands (Pu et al., 2016). In summary, regions within the 800–1000 nm range have been related to SSC variations, while absorption bands referred to water have been located at 960–970 nm (Camps & Christen, 2009b).

The variance between the spectra acquired at different storage time was evaluated by means of PCA. Two different PCAs were developed, the first one by using the spectra pre-treated by SNV+MC and the second one applying the D1+MC. The scores plots of the first two PCs (76.38% and 13.43%; 62.90% and 17.96%) are reported in Fig. 3.1.3a,b. For both cases, a clear separation of the samples according to all the days of storage is not evident, but the samples are placed from right to left along the PC1 and from bottom to top along the PC2 passing from time one to time nine. The loadings

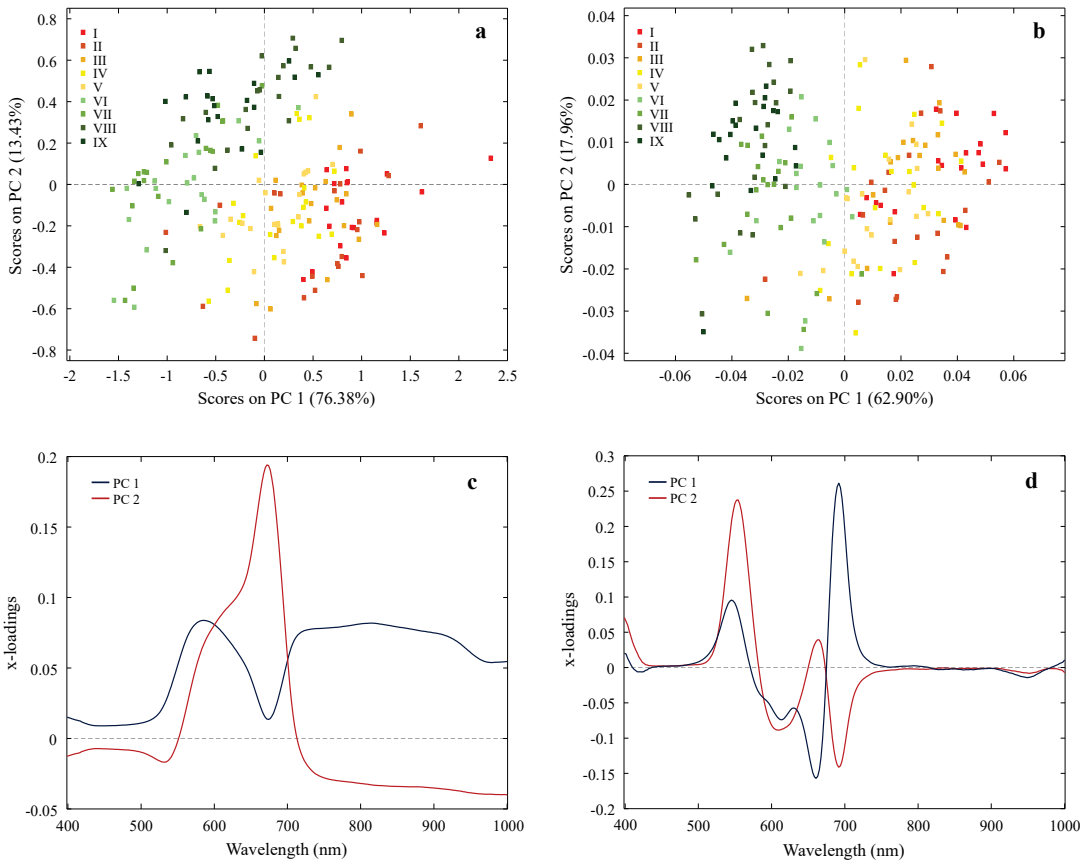

Fig. 3.1.3 – Scores plots (a,b) and loadings plots (c,d) obtained by PCA developed on all the spectra. Spectra pre-treatments: (a,c) standard normal variate and mean centring; (b,d) first derivative and mean centring.

plots (Fig. 3.1.3c,d) suggest that the discrimination might be attributed to absorption bands related to carotenoids (around 560–590 nm) and chlorophyll-α (around 680–690 nm).

PLS and ANN models were developed to predict FF and SSC. PLS results, in terms of R^2, RMSE, RPD, and number of latent variables (LV), in calibration, cross-validation and test set, are reported in Table 3.1.2. For both the quality parameter (FF and SSC), the best models were obtained by treating the spectra with first derivative and mean centring. In particular, for the FF parameter, R^2 in test set ranging from 0.83 (RMSEP=1.98 N) to 0.85 (RMSEP=1.64 N) were achieved. For the prediction of SSC,

Table 3.1.2 – PLS results, in terms of coefficient of determination (R^2), root mean square error (RMSE), residual prediction deviation (RPD) and number of latent variables (LV).

Parameter	Pre-treatment	LV	Calibration set			Cross-validation set			Test set		
			R^2	RMSEC	RPD	R^2	RMSECV	RPD	R^2	RMSEP	RPD
FF (N)	SNV +MC	12	0.93	1.16	3.9	0.81	1.99	2.3	0.83	1.98	2.4
(7.3 ±4.4 N)	D1+MC	12	0.91	1.39	3.2	0.82	1.85	2.4	0.85	1.64	2.6
SSC (°Brix)	SNV +MC	13	0.82	0.42	2.3	0.69	0.58	1.8	0.68	0.59	1.8
(16.3±1.0 °Brix)	D1+MC	13	0.78	0.46	2.1	0.72	0.50	1.9	0.72	0.51	1.9

Note: SNV: standard normal variate; MC: mean centring; D1: first derivative.

the results are less good in terms of R^2, ranging from 0.68 to 0.72, probably due to the small variation of the measured SSC values; however, good RMSEP values, ranging from 0.59 to 0.51 °Brix, were obtained. RPD values above 2 confirm that the PLS

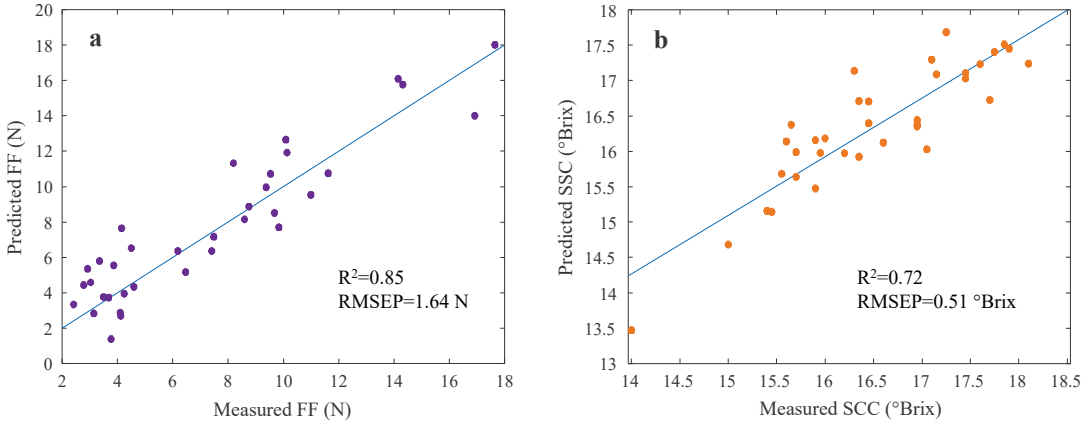

Fig. 3.1.4 – Measured *vs* predicted values of FF (a) and SSC (b) for the test set, obtained by means of PLS regression.

models built to estimate FF are robust, instead the RPD values calculated for the °Brix models are slightly lower. Fig. 3.1.4 shows the best results in terms of measured *vs* predicted values of FF for the test set.

The spectral and spatial information of each pixel in HS images allows the evaluation of quality parameters of each pixel with chemometric models. The pixels having similar spectra showed similar colours in the images, and consequently similar predicted values. Using the best PLS model developed to predict FF, false colour images were obtained. The prediction maps of FF of two representative apricots are shown in Fig. 3.1.5. The colour bars indicate the scales of the reference values (FF in N). Spatial distribution of FF is in alignment with the measured values, particularly passing from 2.74 N to 16.53 N the colour ranges from blue to red. The noise of the HS image, influenced by the fruit curvature and inclination of the light source, especially in the peripheral zone, could affect the spectrum of each pixel, which may result in the underestimation of the FF.

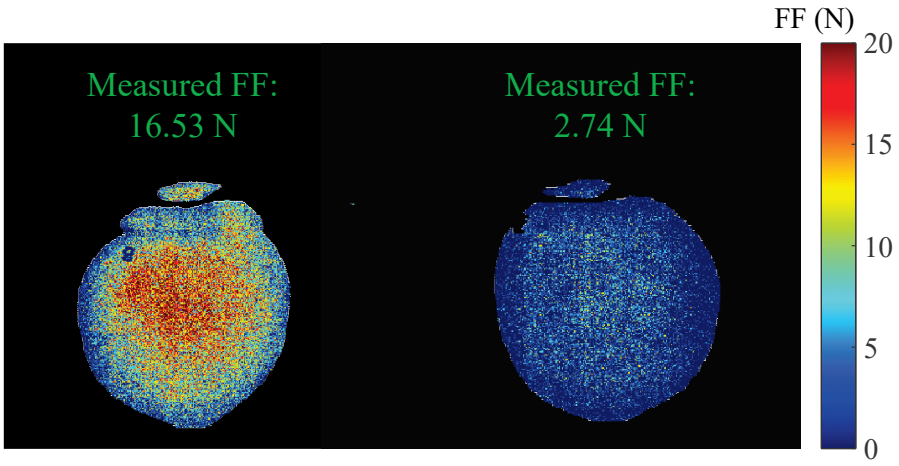

Fig. 3.1.5 – Prediction maps of FF of two representative apricots. Peripheral regions have lower signal intensity in hemispherical samples.

The VIP scores obtained by the PLS models built to estimate FF are reported in Fig. 3.1.6. These scores estimate the importance of each variable in the projection used in a PLS model. A variable with a VIP score close to or greater than one can be considered important in a given model. Considering different spectra pre-treatments (SNV+MC or D1+MC), similar regions with VIP scores higher than one were obtained, suggesting that the wavelengths with the highest contribution to FF prediction range from about 525 to 725 nm. Very similar VIP trends were obtained for PLS models developed by using Vis/NIR data and for measuring FF and IQI ripening index in peaches and nectarine, respectively (Uwadaira et al., 2018; Munera et al., 2017).

Regarding ANN, training was repeated five times and results, in terms of R^2 and RMSE, were averaged, since the convergence is influenced by the initial weight

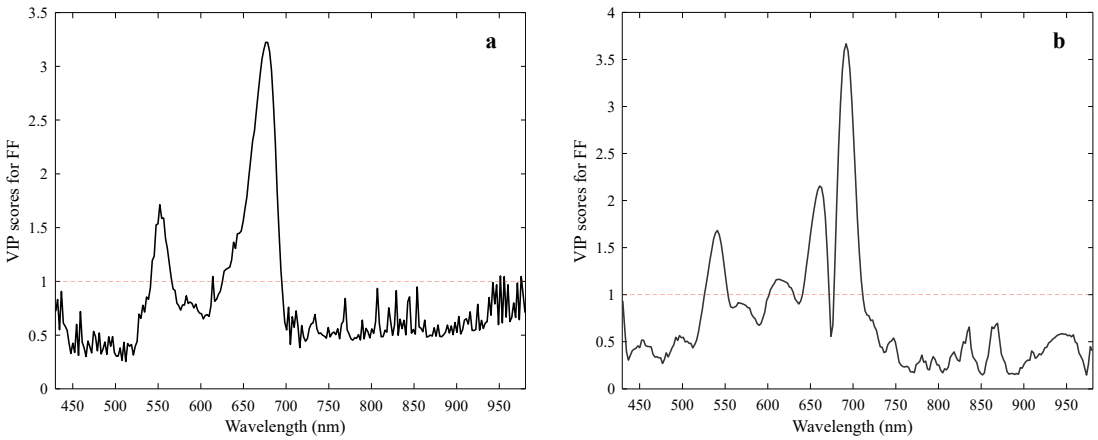

Fig. 3.1.6 – VIP (variable importance in projection) scores of the PLS models to predict FF. Spectra pre-treatments: a) standard normal variate and mean centring; b) first derivative and mean centring.

values. An early stopping technique was used to select the number of training cycles (iterations) to avoid overfitting, using the validation set to monitor the prediction error. Above this point, the error increased further indicating that the ANN tends to overfit. An example of the trend of the errors (training, validation, and external set) as a function of the iteration number is shown in Fig. 3.1.7. The optimal number of iterations (six) was selected corresponding to the minimum value of the validation error. Over this point, the validation error starts to increase.

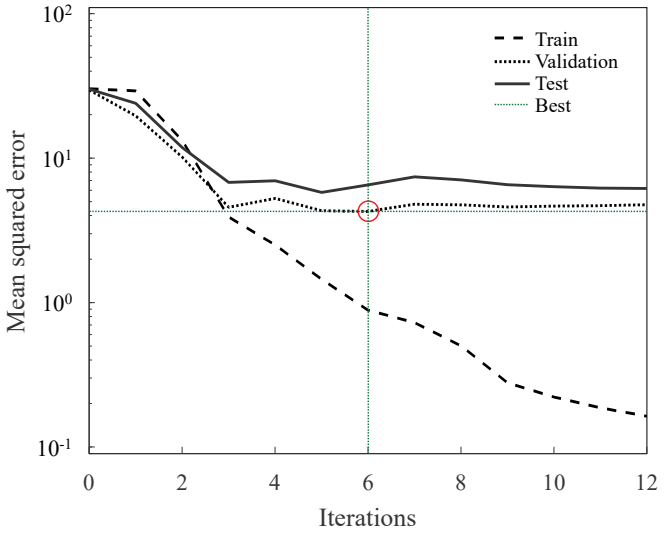

Fig. 3.1.7 – Error graph of training, validation and test set used to stop the ANN model and select the optimal number of iterations.

For both the quality parameter, the best prediction results were obtained with only two nodes in the hidden layer; a larger number of nodes did not increase the network performance. The ANN results, in terms of R^2, RMSE and number of iterations, in training, cross-validation and test set, are reported in Table 3.1.3. As for the PLS, the best result in terms of R^2 was achieved for the FF parameter (R^2=0.85, RMSEP=1.50 N). For the prediction of the SSC, R^2 values (0.65 in test set) lower than those from PLS regression were obtained. A worse performance was also obtained for RMSEP, which was 0.68 °Brix. This is probably due to the small variation of the measured SSC values during the storage. Also in this case, RPD values greater than 2 were reached for the prediction of FF.

Table 3.1.3 – ANN results, in terms of mean coefficient of determination (R^2), root mean square error (RMSE), residual prediction deviation (RPD) and number of iterations.

Parameter	Training set			Cross-validation set			Test set			Iterations
	R^2	RMSEC	RPD	R^2	RMSECV	RPD	R^2	RMSEP	RPD	
FF (N)	0.95	1.14	4.4	0.86	2.01	2.6	0.85	1.50	2.6	5
SSC (°Brix)	0.82	0.43	2.4	0.66	0.67	1.7	0.65	0.68	1.7	6

Comparing the results with those reported in literature and based on the predictive models built considering a spectral range comparable with that of this study, it possible to confirm that R^2 achieved for the FF parameter are higher or in agreement with those reached in previous works. Camps and Christen (2009a) analysed three apricot varieties by using a portable Vis/NIR spectrometer (650–1200 nm) and report R values (in validation) between 0.85 and 0.92, for the prediction of the firmness. Considering the same parameters and spectral range, Camps and Christen (2009b) achieved R value of 0.85 and 0.87, for the *Bergarouge* and *Harostar* variety, respectively. In the former study mentioned (Camps & Christen, 2009a), the SSC prediction resulted in R values between 0.88 and 0.96 (in validation), and RMSECV between 0.67 and 1.00 °Brix. In terms of SSC, the results of the present work are therefore slightly lower; on the contrary, the range of RMSEP from the PLS models is lower (0.51–0.59 °Brix), which means better performance in RMSEP.

3.1.4. Conclusions

The application of HSI technology allowed to estimate the FF and SSC of apricots. Two different multivariate techniques were used to build the predictive models. Particularly a linear method (PLS) and a non-linear method (ANN) were tested.

Good and similar results were achieved for the FF parameter, by using both the statistical techniques, with R^2 values (test set) of 0.85 for both PLS and ANN, and RMSEP of 1.64 N and 1.50 N, for the PLS and ANN, respectively. SSC was characterized by a low level of variation (9%) and an initial level already suitable for retail sale: as a possible consequence, both the prediction models (PLS and ANN) were less able to estimate this quality parameter than the previous one (R^2 up to 0.72), nevertheless RMSEP range obtained by PLS models (0.51–0.59 °Brix) was good. Due to this finding, it would be possible to discriminate and then sort apricots for the fresh market, discarding those with too low FF values therefore undesirable for retail sale. In light of the obtained results, the HSI technology could be implemented in a sorting line of apricots for the fresh market, subject to the improvement of hyperspectral image segmentation techniques, dimensionality reduction, and finally prediction, to automate real-time analysis.

3.1.5. References

Amoriello, T., Ciccoritti, R., & Carbone, K. (2019). Vibrational spectroscopy as a green technology for predicting nutraceutical properties and antiradical potential of early-to-late apricot genotypes. *Postharvest Biology and Technology*, *155*, 156–166. https://doi.org/10.1016/j.postharvbio.2019.03.013

Amoriello, T., Ciccoritti, R., Paliotta, M., & Carbone, K. (2018). Classification and prediction of early-to-late ripening apricot quality using spectroscopic techniques combined with chemometric tools. *Scientia Horticulturae*, *240*, 310–317. https://doi.org/10.1016/j.scienta.2018.06.031

Berardinelli, A., Cevoli, C., Silaghi, F. A., Fabbri, A., Ragni, L., & Giunchi, A. (2010). FT-NIR Spectroscopy for the Quality Characterization of Apricots (Prunus Armeniaca L.). *Journal of Food Science*, *75*(7), 462–468. https://doi.org/10.1111/j.1750-3841.2010.01741.x

Bureau, S., Reich, M., Renard, C. M. G. C., Ruiz, D., & Audergon, J. M. (2012). Rapid Characterization of Apricot Fruit Quality Using Near and Mid-Infrared Spectroscopy: Study of the Model Robustness. *Acta Horticulturae*, *934*, 173–176. https://doi.org/10.17660/ActaHortic.2012.934.20

Bureau, S., Renard, C. M. G. C., Fakhfackh, Z., & Audergon, J. M. (2018). Infrared spectroscopy as a rapid tool to assess apricot fruit quality: Comparison of two strategies for a model establishment. *Acta Horticulturae*, *1214*, 145–149. https://doi.org/10.17660/ActaHortic.2018.1214.24

Bureau, S., Ruiz, D., Reich, M., Gouble, B., Bertrand, D., Audergon, J. M., & Renard, C. M. G. C. (2009). Rapid and non-destructive analysis of apricot fruit quality using FT-near-infrared spectroscopy. *Food Chemistry*, *113*(4), 1323–1328. https://doi.org/10.1016/j.foodchem.2008.08.066

Buyukcan, M. B., & Kavdir, I. (2017). Prediction of some internal quality parameters of apricot using FT-NIR spectroscopy. *Journal of Food Measurement and Characterization*, *11*(2), 651–659. https://doi.org/10.1007/s11694-016-9434-9

Camps, C., & Christen, D. (2009a). Non-destructive assessment of apricot fruit quality by portable visible-near infrared spectroscopy. *LWT - Food Science and Technology*, *42*(6), 1125–1131. https://doi.org/10.1016/j.lwt.2009.01.015

Camps, C., & Christen, D. (2009b). On-tree follow-up of apricot fruit development using a hand-held NIR instrument. *Journal of Food, Agriculture and Environment*, *7*(2), 394–400.

Carlini, P., Massantini, R., & Mencarelli, F. (2000). Vis-NIR measurement of soluble solids in cherry and apricot by PLS regression and wavelength selection. *Journal of Agricultural and Food Chemistry*, *48*(11), 5236–5242. https://doi.org/10.1021/jf000408f

Chandrasekaran, I., Panigrahi, S. S., Ravikanth, L., & Singh, C. B. (2019). Potential of Near-Infrared (NIR) Spectroscopy and Hyperspectral Imaging for Quality and Safety Assessment of Fruits: an Overview. *Food Analytical Methods*, *12*(11), 2438–2458. https://doi.org/10.1007/s12161-019-01609-1

Chong, I. G., & Jun, C. H. (2005). Performance of some variable selection methods when multicollinearity is present. *Chemometrics and Intelligent Laboratory Systems*, *78*(1–2), 103–112. https://doi.org/10.1016/j.chemolab.2004.12.011

Christen, D., Camps, C., Summermatter, A., Gabioud Rebeaud, S., & Baumgartner, D. (2012). Prediction of the pre- and postharvest apricot quality with different VIS/NIRs devices. *Acta Horticulturae*, *966*, 149–154. https://doi.org/10.17660/actahortic.2012.966.23

Ciacciulli, A., Bassi, D., Castellari, L., & Foschi, S. (2018). Fruit ripening evolution in diverse commercial apricots by conventional and non-destructive methods: Preliminary results. *Acta Horticulturae*, *1214*, 165–170. https://doi.org/10.17660/ActaHortic.2018.1214.27

De Oliveira, G. A., Bureau, S., Renard, C. M. G. C., Pereira-Netto, A. B., & De Castilhos, F. (2014). Comparison of NIRS approach for prediction of internal quality traits in three fruit species. *Food Chemistry*, *143*, 223–230. https://doi.org/10.1016/j.foodchem.2013.07.122

ElMasry, G., Wang, N., ElSayed, A., & Ngadi, M. (2007). Hyperspectral imaging for nondestructive determination of some quality attributes for strawberry. *Journal of Food Engineering*, *81*(1), 98–107. https://doi.org/10.1016/j.jfoodeng.2006.10.016

Guo, W., Li, W., Yang, B., Zhu, Z. Z., Liu, D., & Zhu, X. (2019). A novel noninvasive and cost-

effective handheld detector on soluble solids content of fruits. *Journal of Food Engineering*, *257*, 1–9. https://doi.org/10.1016/j.jfoodeng.2019.03.022

Helin, R., Indahl, U. G., Tomic, O., & Liland, K. H. (2022). On the possible benefits of deep learning for spectral preprocessing. *Journal of Chemometrics*, *36*(2), e3374. https://doi.org/10.1002/cem.3374

Manley, M., Joubert, E., Myburgh, L., & Kidd, M. (2007). Prediction of soluble solids content and post-storage internal quality of Bulida apricots using near infrared spectroscopy. *Journal of Near Infrared Spectroscopy*, *15*(3), 179–188. https://doi.org/10.1255/jnirs.725

McGlone, V. A., & Kawano, S. (1998). Firmness, dry-matter and soluble-solids assessment of postharvest kiwifruit by NIR spectroscopy. *Postharvest Biology and Technology*, *13*(2), 131–141. https://doi.org/10.1016/S0925-5214(98)00007-6

Munera, S., Besada, C., Blasco, J., Cubero, S., Salvador, A., Talens, P., & Aleixos, N. (2017). Astringency assessment of persimmon by hyperspectral imaging. *Postharvest Biology and Technology*, *125*, 35–41. https://doi.org/10.1016/j.postharvbio.2016.11.006

Nicolaï, B. M., Beullens, K., Bobelyn, E., Peirs, A., Saeys, W., Theron, K. I., & Lammertyn, J. (2007). Nondestructive measurement of fruit and vegetable quality by means of NIR spectroscopy: A review. *Postharvest Biology and Technology*, *46*(2), 99–118. https://doi.org/10.1016/j.postharvbio.2007.06.024

Pu, H., Liu, D., Wang, L., & Sun, D.-W. (2016). Soluble Solids Content and pH Prediction and Maturity Discrimination of Lychee Fruits Using Visible and Near Infrared Hyperspectral Imaging. *Food Analytical Methods*, *9*(1), 235–244. https://doi.org/10.1007/S12161-015-0186-7

Ruiz, D., Reich, M., Bureau, S., Renard, C. M. G. C., & Audergon, J. M. (2008). Application of reflectance colorimeter measurements and infrared spectroscopy methods to rapid and nondestructive evaluation of carotenoids content in apricot (Prunus armeniaca L.). *Journal of Agricultural and Food Chemistry*, *56*(13), 4916–4922. https://doi.org/10.1021/jf7036032

Uwadaira, Y., Sekiyama, Y., & Ikehata, A. (2018). An examination of the principle of non-destructive flesh firmness measurement of peach fruit by using VIS-NIR spectroscopy. *Heliyon*, *4*(2), e00531. https://doi.org/10.1016/j.heliyon.2018.e00531

Wendel, A., Underwood, J., & Walsh, K. (2018). Maturity estimation of mangoes using hyperspectral imaging from a ground based mobile platform. *Computers and Electronics in Agriculture*, *155*, 298–313. https://doi.org/10.1016/j.compag.2018.10.021

Witherspoon, J. M., & Jackson, J. F. (1995). Analysis of Fresh and Dried Apricot. In H. F. Linskens & J. F. Jackson (Eds.), *Fruit Analysis* (pp. 111–131). Springer-Verlag Berlin Heidelberg. https://doi.org/10.1007/978-3-642-79660-9_7

Xue, J., Zhang, S., & Zhang, J. (2015). Ripeness classification of Shajin apricot using hyperspectral imaging technique. *Transactions of the Chinese Society of Agricultural Engineering (CSAE)*, *31*(11), 300–307. https://doi.org/10.11975/j.issn.1002-6819.2015.11.043

3.2. Ripeness evaluation of kiwifruit by hyperspectral imaging

Scientific publication – Paper II

Benelli, A., Cevoli, C., Fabbri, A., & Ragni, L. (2021a). Ripeness evaluation of kiwifruit by hyperspectral imaging. *Biosystems Engineering*. https://doi.org/10.1016/j.biosystemseng.2021.08.009

Alessandro Benelli[a], Chiara Cevoli[a,b*], Angelo Fabbri[a,b] , Luigi Ragni[a,b]

[a]*Department of Agricultural and Food Sciences, Alma Mater Studiorum, University of Bologna, Piazza Goidanich 60, Cesena, 47521, Italy*

[b]*Interdepartmental Centre for Agri-Food Industrial Research, Alma Mater Studiorum, University of Bologna, Via Quinto Bucci 336, Cesena, 47521, Italy*

[*]*Corresponding author: chiara.cevoli3@unibo.it*

Abstract

Rapid, non-destructive fruit sorting techniques are increasingly being adopted to ensure that producers, industry, and consumers receive products that meet their quality requirements. Quality attributes typically used to assess fruit ripeness include soluble solids content (SSC) and flesh firmness (FF). In this study, hyperspectral imaging operating at 400–1000 nm (Vis/NIR) was adopted to evaluate the ripeness degree of 'Hayward' kiwifruit. Partial least square (PLS) regression models were developed to estimate SSC and FF, while two different types of PLS discriminant analysis (PLS-DA) were used to classify samples according to three repining classes (defined on the base of SSC and FF values). To reduce the computation complexity, and simplify the calibration models, two variable selection methods (genetic algorithm GA, and variable importance in projection VIP) were adopted. For SSC, the prediction R^2 values ranged from 0.85 (RMSE=1.10 °Brix) to 0.94 (RMSE=0.73 °Brix), and for FF from 0.82 (RMSE=14.51 N) to 0.92 (RMSE=9.87 N). Classification sensitivity reached values of 97% and 93%, for the model considering the SSC and FF classes, respectively. Prediction and classification performances remained substantially unchanged by reducing the number of wavelengths. Therefore, hyperspectral imaging appears to be suitable for prediction of kiwi quality attributes and their classification.

Keywords: Hyperspectral, kiwifruit, PLS, PLS-DA, ripening.

3.2.1. Introduction

Most fruits and vegetables are characterised by a short harvest season. Short or long-term storage is therefore necessary to ensure a continuous supply of quality raw material and to extend the processing and marketing periods of fresh produce (Mishra & Gamage, 2020a). Fruit is harvested when threshold values of some quality attributes, expressing their physiological maturity, are reached. With regard to kiwifruits, the soluble solids content (SSC) must reach 6.2–6.5 °Brix (from 7 to 9 °Brix for storage), while the flesh firmness (FF) must be equal to or greater than about 62 N (OECD, 2008; Crisosto & Kader, 1999; Walsh et al., 2020). Regarding commercial ripening, to satisfy consumer taste, SSC should exceed 12.5 °Brix, while FF should fall below approximately 9–13 N (Crisosto & Kader, 1999).

The storage potential of kiwifruit in air at storage sites under semi-optimal conditions of temperature and relative humidity ranges from 4 to 8 weeks (Mishra & Gamage, 2020a). From postharvest to commercial maturity, several changes at the cellular level affect fruit texture, which becomes softer (Mishra & Gamage, 2020b). Composition, water content, turgor pressure and cell wall constituents undergo various transformations. In kiwifruit pulp cells, the structure of the middle lamella and the primary cell wall weakens mainly due to high pectin solubilisation; in addition, a moderate contribution to fruit softening is provided by the loss of pectic arabinan side chains. These phenomena result in cell separation and wall swelling (Watkins, 2017; Mishra & Gamage, 2020b).

Early in ripening, there is often an increase in sugar concentration. In fruits and vegetables, sucrose comes from photosynthetic leaves and/or hydrolysis of starch reserves degraded by amylase, resulting in an increase in SSC. As ripening progresses, glucose and fructose increase due to the action of the enzyme invertase through glycolysis. The amount of sucrose may also increase due to gluconeogenesis of organic acids (Sánchez-Rodríguez et al., 2019). As fruits ripen, the chlorophyll content generally decreases, and other pigments such as carotenoids are usually biosynthesised and accumulated. However, there are some exceptions to this general behaviour: some fruits retain chlorophyll, such as the skin of ‘Granny Smith’ green apples and ‘Conference’ pears and the flesh of ‘Hayward’ green kiwi, in which the accumulation of carotenoids decreases with ripening. Kiwifruits are also very rich in vitamin C (Alós et al., 2019; Mellidou et al., 2019).

The use of the penetrometer and refractometer to measure FF and SSC, respectively, result in destruction of the sample and are time consuming and expensive. To

overcome this problem, several techniques, many of which are non-destructive, have been introduced over the past few decades and generally allow for faster analysis and lower costs.

Near-infrared (NIR) spectroscopy (McGlone & Kawano, 1998; Schaare & Fraser, 2000; X. F. Hu et al., 2016) and portable NIR instruments used directly in the field (Costa et al., 2015; Cantin et al., 2011) have been adopted with good results to predict dry matter , SSC and FF of kiwifruit.

Time-domain diffuse reflectance spectroscopy, a pulsed laser spectroscopic technique, was applied to classify kiwifruits according to FF, sugar content and acidity, obtaining the best result with acidity (Valero et al., 2004). A multifrequency magnetic induction spectroscopy system (156 kHz–2.5 MHz) resulted in a good correlation of the bio-impedance conductivity measurement with SSC and FF (Bauchot et al., 1999; O'Toole et al., 2015). Ragni et al. (2012) adopted waveguide spectroscopy (2–3 GHz and 15–16 GHz) to evaluate SSC and FF of kiwifruit during storage, obtaining the best results by partial least squares (PLS). Using a device consisting of a xenon lamp whose emitted radiation passes through kiwi samples and is captured by a NIR-sensitive camera, 8-bit greyscale images (255 grey tones) have been used to predict the FF and SSC of kiwifruit (Berardinelli et al., 2019).

FF penetrometer measurements correlated with measurements from a non-invasive system called 'intelligent firmness detector', which can detect the FF of a fruit as it rotates on a grading belt (Blanke, 2013). Li et al. (2016) correlated penetrometer measurements with those from four different non-destructive devices. X. G. Hu et al. (2016) observed a correlation between colour change and FF of kiwifruit by adopting a palladium complex-based colorimetric sensor that can be used for real-time monitoring of kiwifruit ripening.

Hyperspectral imaging (HSI) has been increasingly applied in the last decade for determination of quality parameters in fruits and vegetables. This technique combines image analysis and spectroscopy, obtaining absorbance/reflectance/transmittance spectra as single acquired pixels (in this technique called voxels) that form the hyperspectral (HS) image. HSI has been applied for the determination of quality parameters of fruits and vegetables in the laboratory and directly in the field (Chandrasekaran et al., 2019). HSI was implemented by Zhu et al. (2017) for quality attributes prediction of three kiwifruit varieties at commercial maturity. The best results were obtained in the 380–1023 nm range and applying multiple linear regression models, with a R_P=0.981 and a residual prediction deviation (RPD) of 5.17 N cm^{-2} for FF. R_P=0.952 and RPD=3.26 °Brix were obtained for SSC. Serranti et al. (2017) proposed application of HSI (1000–1650 nm) to evaluate kiwifruit ripeness. In particular, HS images of the inner pulp and outer surface of kiwifruit were acquired to

assess the degree of ripening. Fruits, divided into 4 batches, were analysed on the day of harvest and after 7 and 14 days. Using principal component analysis (PCA) false-colour plots of the principal components were obtained, which allowed to discriminate the ripening time of fruits.

In this study, HSI combined with variable selection methods and chemometric techniques was implemented to evaluate quality parameters of kiwifruits in post-harvest conditions. PLS models were developed to predict the SSC and FF, while PLS-discriminant analysis (PLS-DA) and *soft* PLS-DA were used to classify samples into 3 ripening classes defined through observation of SSC and FF.

3.2.2. Materials and methods

3.2.2.1. Samples

130 unconditioned 'Hayward' kiwifruits harvested near Latina (Italy) and delivered on November 11th, 2019 to the storage centre, were adopted for the present research. During the analysis period, kiwis were stored at 15 °C. The analyses were carried out on 5 different days starting from the day following delivery to the storage centre: day I (November 12th), II (November 19th), III (November 26th), IV (December 10th) and V (December 17th). The samples were weighed immediately before being placed in the storage chamber and before being analysed. As the samples were not homogeneous in terms of weight, they were divided into four weight classes (80–100 g, 100–120 g, 120–140 g and 140–160 g), random selected and equally distributed over the days of analysis.

3.2.2.2. Hyperspectral measurements

A push-broom linear array hyperspectral camera working in the 400–1000 nm spectral range (Nano-Hyperspec VNIR, Headwall Photonics, Inc., Fitchburg, MA, USA) was adopted to acquire HS images. The camera was equipped with a 17 mm effective focal length (EFL) lens, characterised by an angular field of view (FOW) of 15.3°.

The scan line has a spatial resolution of 640 points, each with 272 spectral bands and a nominal spectral resolution of 2.2 nm. The sensor exposure time and frame period were set at 28 ms, while the frame rate, which depends on the exposure time set, was 34.2 frames s^{-1} (FPS).

Fig. 3.2.1 illustrates the HSI system adopted for the experimental trials. The camera was installed on a metal frame with the optical axis perpendicular to the underlying conveyor belt, which simulates an industrial fruit sorting line at a height of 540 mm. The speed of the conveyor belt, on which the sample runs, was approximately 8 mm s^{-1}. Two spotlights inclined by 15° and at a height of 320 mm from the conveyor belt

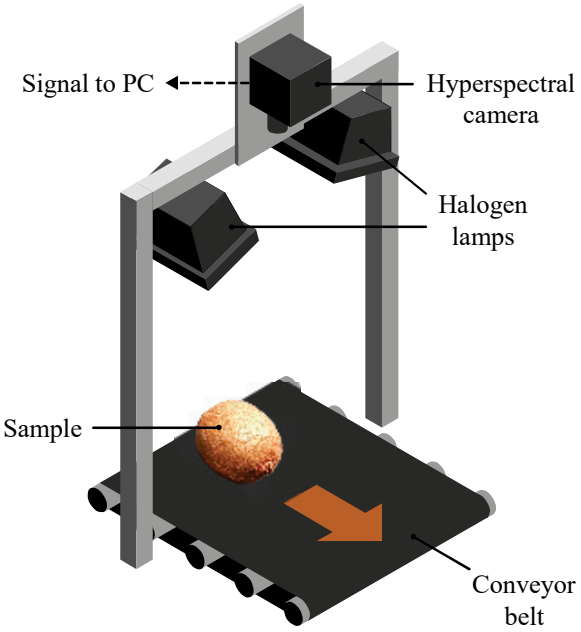

Fig. 3.2.1 – Representation of the lab-scale hyperspectral imaging system used to acquire hyperspectral images of kiwi samples.

plane were installed on the metal frame. The spotlights were equipped with 120 W halogen lamps. Ambient light was isolated using a specific box.

The white (R_W) and dark (R_D) reference reflectance spectra were obtained by acquiring a high-reflectance matte white panel and covering the camera lens with its cup, respectively. The raw diffuse reflectance spectrum (R_R) was obtained by scanning the sample. Each sample was scanned longitudinally at laboratory temperature (22±1 °C). The calibrated diffuse reflectance spectrum (R_C) was calculated by applying the Eq. (1) (Guo et al., 2019):

$$R_C = \frac{R_R - R_D}{R_W - R_D} \quad (1)$$

3.2.2.3. Destructive measurements of quality parameters

The Magness-Taylor FF and SSC of the kiwifruit samples were measured after HS image acquisitions. FF was determined through a compression test performed on kiwi samples with a texture analyser (TA-HDi, Stable Micro System Ltd., Godalming, UK) equipped with a cylindrical steel probe 8 mm diameter with a hemispherical head (ASABE Standard, 2008). Before the analysis, a small portion of skin in the area subjected to the compression test was removed. Tests were performed with a penetration speed of 0.5 mm s^{-1} and a maximum deformation of 8 mm. Kiwi juice was analysed with a digital refractometer (PR-101 Digital Refractometer, ATAGO CO., LTD, Tokyo, Japan) to measure the SSC and expressed in °Brix.

Significant differences between the means of the quality indexes (FF and SSC) at different days of storage were evaluated through analysis of variance (one-way ANOVA with Tukey-HSD post-hoc test, p-level>0.05). Homogeneity of variance was evaluated by the Levene test.

3.2.2.4. Data analysis

3.2.2.4.1. ROI determination

The background was removed from each HS image by k-means clustering, performed using 2 clusters (classification method based on Euclidean distance) on the calibrated spectra (HyperCube v. 11.52, U.S. Army Engineer Research and Development Center (ERDC), USA). Cluster 1 (red in Fig. 3.2.2b) represents the background to be discarded, while cluster 2 (green in Fig. 3.2.2b and Fig. 3.2.2c) is the region of interest (ROI). It can be observed (Fig. 3.2.2c) that the partially shaded edge of the kiwi sample was not included in cluster 2. For each sample, the mean spectrum was calculated considering spectra of the ROI.

Fig. 3.2.2 – (a) RGB representation obtained from a hyperspectral image of a kiwi sample; (b) ROI (green) and background (red) obtained by k-means clustering; (c) ROI overlay (semi-transparent green) on the RGB representation in (a).

3.2.2.4.2. Multivariate analysis

Due to a low signal-to-noise ratio produced by the sensor, spectral bands between 400 and 424 nm were removed from the analysis. The spectra were subsequently smoothed to reduce noise from the spectra and pre-processed by applying the standard normal variate (SNV) method, first derivative (D1) and mean centred (MC). (Rinnan et al., 2009). The data were preliminary visualised according to quality indices (SSC and FF) and days of analysis using PCA.

3.2.2.4.3. Selection of wavelengths

The selection of wavelengths from the original or pre-processed spectra can reduce the computation complexity, improve the predictive ability of calibration models and simplify the calibration models. Furthermore, a limited number of wavelengths can be directly used for developing on-line or portable multispectral equipment. The wavelength selection methods used in this study are variable importance in projection

(VIP) and genetic algorithm (GA). VIP method is a filter method, which estimates the importance of each variable in the projection used in a PLS model. The VIP score calculates the contribution of each variable according to variance explained by each PLS component. The 'greater than one' is conventionally used as the criterion for variable selection; accordingly, only variables with VIP scores greater than one were selected (Wang et al., 2015). This method has been extensively used in different fields and adopted for a variety of data types (Farrés et al., 2015).

GA is a wrapper method implemented by selecting the candidate of sensitive wavelengths and optimising the number of evaluations in each run, while PLS is applied to perform and evaluate the selected wavelengths (Zhu et al., 2017). The computation steps involved have been described by (Mehmood et al., 2012). In this study, 100 runs were set.

3.2.2.4.4. Chemometric models

PLS regression models were developed to estimate the quality indices (SSC and FF), adopting the Onion method to split the dataset (130 samples) in calibration (75% of samples, with venetian blinds as cross-validation method) and validation test set (25% of samples).

The onion method selects a ring of the most unique samples (based on Euclidian distance from the mean, like the outer-most layer of an onion.) These are used in the calibration set. Next, a ring of less unique samples, just inside the first set (the next onion layer), is put into the validation set. This is repeated two more times so that there are three outer rings of the most unique and less unique samples. Finally, all remaining samples are split randomly into calibration and validation (Gallagher et al., 2004; Gallagher & O'sullivan, 2020).

To avoid over-fitting the model, the optimal number of latent variables (LV) were chosen by identifying the global minimum of root mean square error in cross validation (RMSECV).

PLS-DA and multi-class *soft* PLS-DA (Pomerantsev & Rodionova, 2018; Zontov et al., 2020) were developed to classify samples into 3 ripening classes, according to Crisosto & Kader (1999). For the SSC, the following limits were selected: $SSC<6.5$ (unripe), $6.5\leq SSC<12.5$ (ripe for storage) and $SSC\geq12.5$ (ripe for consumer), while for FF the following were used: $FF\geq62$ (unripe), $13\leq FF<62$ (ripe for storage) and $FF<13$ (ripe for consumer). These ranges were chosen since they meet the requirements at both the harvesting stage (unripe to ripe for storage) and by consumers (ripe for storage to ripe for consumer). The dataset was spilt using the Onion method, as described for PLS.

PLS-DA assumes that each sample is assigned to a single class using a probabilistic approach based on Bayes rule. Multi-class *soft* PLS-DA, by adopting PCA of the

matrix T of the predicted response ($\hat{Y}$), classifies samples according to the distance between rows of this matrix and rows of matrix Y (measured response). The procedure can be summarised as:

$$X, Y \xrightarrow{PLS} \hat{Y} \xrightarrow{PCA} T \quad (2)$$

where X is the matrix utilised as a predictor. Furthermore, with multi-class *soft* PLS-DA, the sample can be assigned to one or more classes, or it cannot be assigned to any class (Zontov et al., 2020).

All the chemometric models were developed using PLS Toolbox for MATLAB R2020b, except for multi-class *soft* PLS-DA, where PLS-DA Toolbox for MATLAB R2019a was used.

3.2.2.4.5. Spatial distribution

To reduce calculation time, image resolution was decreased by averaging the spectra of adjacent pixels (3×3). PLS calibration models were developed considering the mean spectra of the ROIs and applied to groups of 3×3 pixels of each image. Consequently, predicted SSC and FF values were obtained for each pixel group. This allows to observe the difference attributes from sample to sample and even within the same sample.

3.2.3. Results

Means and standard deviations of quality attributes (SSC and FF) measured on kiwi samples during the 5 days of analysis are reported in Fig. 3.2.3. Significant differences

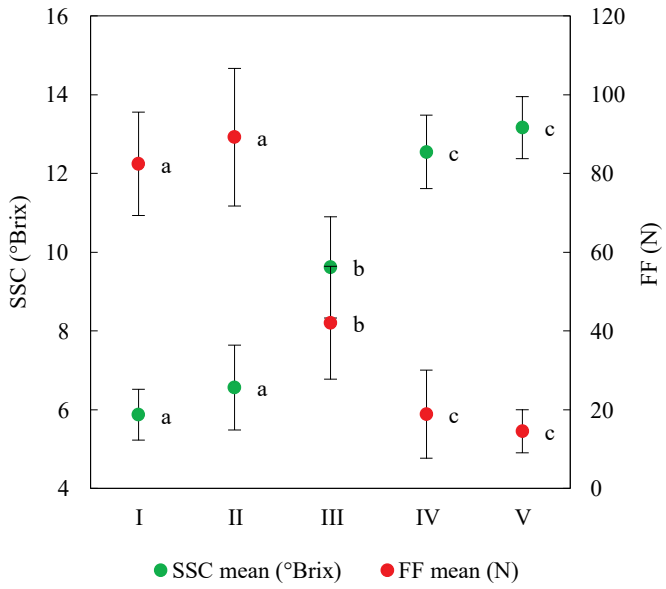

Fig. 3.2.3 – Mean and standard deviation of quality attributes (SSC and FF) of the sample of kiwifruits during the five days of analysis.

were observed for both attributes between the second and third day and between the third and fourth day, whereas no significant differences were found between the first and second day and between the fourth and fifth day. The percentage variation between the first and last day of analysis was 124% and -82% for SSC and FF, respectively. The correlation between FF and SSC was negative, with a probable linear trend (R^2=0.84; FF = -10.22 SSC + 146.72).

Fig. 3.2.4 shows the mean spectra of kiwifruit samples according to SSC and FF, and pre-processed by SNV and D1 filters, respectively. The portion of the spectrum from 400 to 700 nm (visible) is characterised by absorption bands of anthocyanins, carotenoids and chlorophyll-α (ElMasry et al., 2007), which have been adopted as quality attributes to assess fruit ripeness. The NIR part of the spectrum (700–1000 nm) shows absorption bands related to water (Nicolaï et al., 2007) and sugar (Pu et al., 2016). Manley et al. (2007) and Camps & Christen (2009) observed that in the 800–1000 nm range, SSC-related spectral information tends to be less covered by water, whose absorption peaks are broad and not very marked.

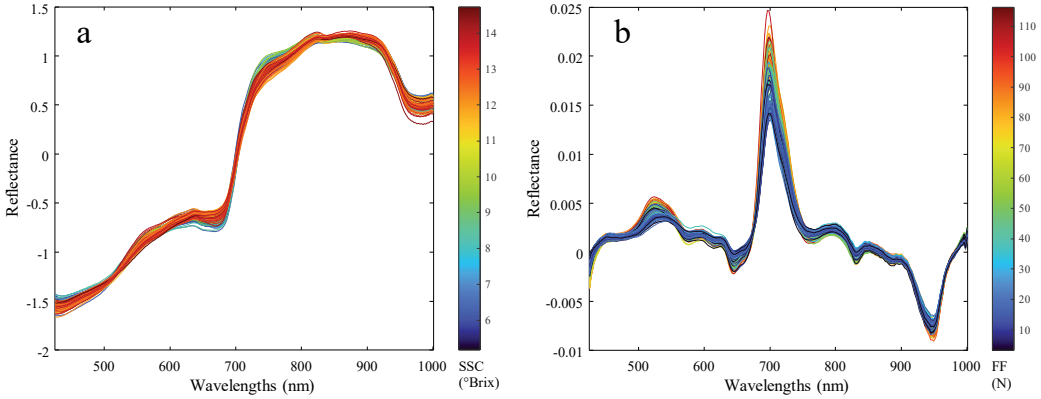

Fig. 3.2.4 – Mean spectra of kiwi samples pre-processed by: (a) SNV (colour scale related to SSC); (b) D1 (colour scale related to FF).

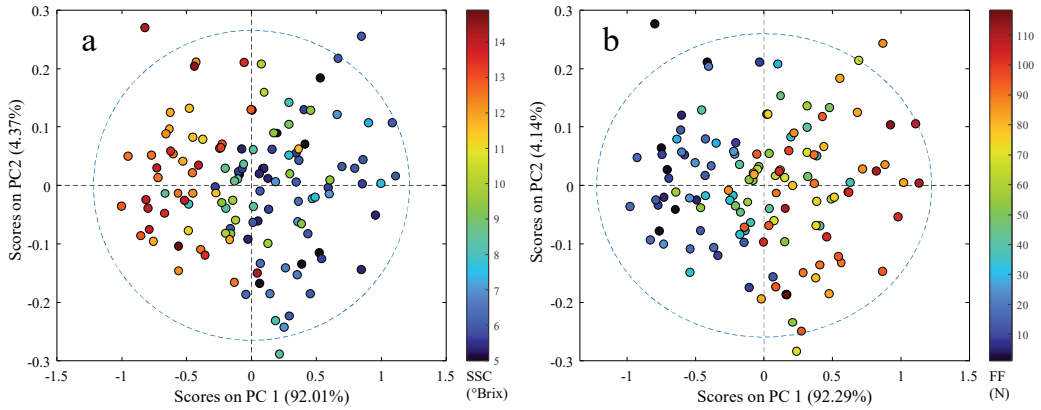

Fig. 3.2.5 – Scores plots obtained by PCA according to: (a) SSC; (b) FF. The colour scales are reported on the right of the relative scores plot.

The scores plots of principal components 1 and 2 resulting from PCA were obtained mean centring the calibrated spectra (Fig. 3.2.5). Subsequently, some outliers were removed. Samples were distributed along PC1 from right to left for increasing SSC values (Fig. 3.2.5a) and decreasing FF values (Fig. 3.2.5b).

The results of the PLS models developed to estimate SSC and FF were reported in Table 3.2.1. Two different pre-processing sequences were adopted: SNV+MC and

Table 3.2.1 – Results of the PLS models developed to estimate SSC e FF.

Qualitative index	Spectra pre-processing	Variable selection (nv)	LVs	Calibration		Cross-validation		Prediction	
				R^2	RMSEC	R^2	RMSECV	R^2	RMSEP
SSC	SNV+MC	All (260)	12	0.96	0.59 °Brix	0.92	0.83 °Brix	0.85	1.10 °Brix
		VIP (104)	10	0.92	0.83 °Brix	0.88	1.03 °Brix	0.86	1.14 °Brix
		GA (47)	11	0.96	0.61 °Brix	0.93	0.81 °Brix	0.94	0.73 °Brix
	D1+MC	All (260)	12	0.95	0.66 °Brix	0.90	0.97 °Brix	0.90	0.94 °Brix
		VIP (58)	6	0.90	0.94 °Brix	0.85	1.12 °Brix	0.88	1.08 °Brix
		GA (78)	7	0.92	0.87 °Brix	0.86	1.13 °Brix	0.90	1.00 °Brix
FF	SNV+MC	All (260)	14	0.93	8.56 N	0.86	12.43 N	0.85	13.10 N
		VIP (97)	13	0.91	9.76 N	0.82	14.17 N	0.82	14.51 N
		GA (72)	14	0.94	7.66 N	0.87	11.50 N	0.92	9.87 N
	D1+MC	All (260)	8	0.90	10.02 N	0.85	12.41 N	0.84	13.62 N
		VIP (41)	10	0.90	10.03 N	0.86	12.30 N	0.86	12.26 N
		GA (75)	10	0.92	9.64 N	0.87	12.26 N	0.89	11.31 N

Note: SSC = soluble solids content; FF = flesh firmness; SNV = standard normal variate; MC = mean centred; D1 = first derivative; nv = number of variables selected; All = all variables; VIP = variable importance in projection; GA = genetic algorithms; LVs = latent variables.

D1+MC, as well as two variable selection methods, namely VIP and GA. For SSC, the prediction R^2 values ranged from 0.85 (RMSE=1.10 °Brix) to 0.94 (RMSE=0.73 °Brix) and the best results were achieved applying D1 pre-processing and selecting the variables by the GA. For FF, the best results, in terms of prediction R^2 (0.92) and RMSE (9.87 N), were obtained with SNV pre-processing and GA variable selection methods. In general, for both quality parameters, reduction of the variable number, especially by using the GA method, positively affected the results in terms of increasing of R^2 and reducing RMSE in prediction. Selected variables by GA method are shown in Fig. 3.2.6 for SSC and FF prediction, respectively. Most are in the NIR region (700–1000 nm), especially for SSC. The spectral regions selected for the model prediction of SSC and FF were quite different. The region from 950 to 1000 nm, typically related to carbohydrate absorption, was selected only for SSC prediction, while the region around 750 nm (band assignments for the major water (O–H) vibration) was defined only for FF prediction. This may suggest that FF prediction is

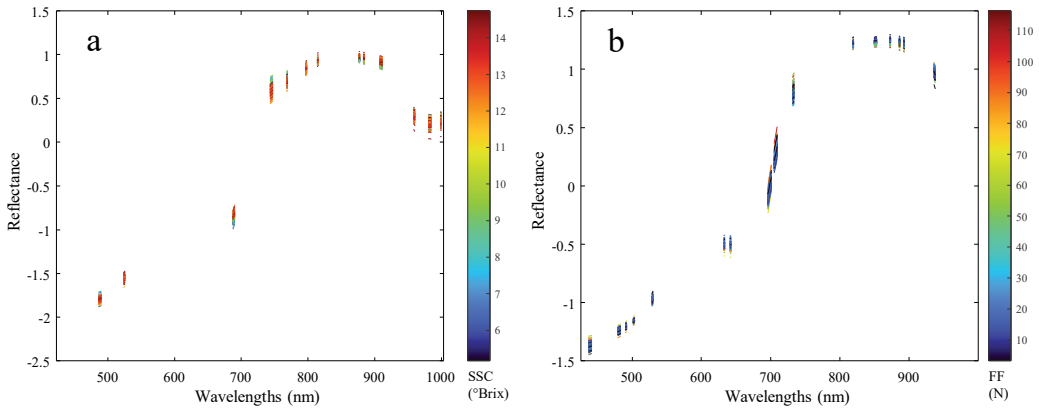

Fig. 3.2.6 – GA selections of mean spectra of kiwi samples pre-processed by SNV related to: (a) SSC and (b) FF.

independent of SSC correlation. Considering the VIP method, the selected variables (VIP>1) were in similar spectral ranges (650–1000 nm) to those for the GA method, even if appreciable differences between the SSC and FF models were not observed (Fig. 3.2.7). Overall, VIP scores obtained by PLS models developed after variable selection, were higher than one for all x-variables. This suggests that the contribution of the selected spectral variables on the model performance, is similar.

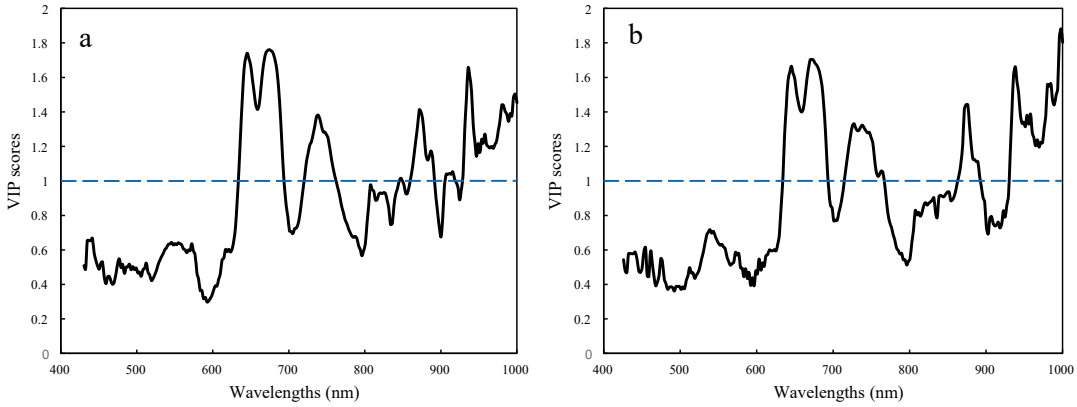

Fig. 3.2.7 – VIP scores of the PLS models developed to predict SSC (a) and FF (b) (spectra pre-processed by SNV).

Measured vs. predicted values of SSC obtained by PLS regression applying SNV+MC pre-processing and GA variable section method are shown in Fig. 3.2.8. These results confirm the feasibility of HSI in the Vis/NIR spectral region for the rapid prediction of kiwi quality parameters, such as SSC and FF; furthermore, they are in good agreement with those reported in the literature (R of 0.9812 and 0.9523 for FF and SSC, respectively) by Zhu et al. (2017) in a very similar wavelength range (380–1023 nm).

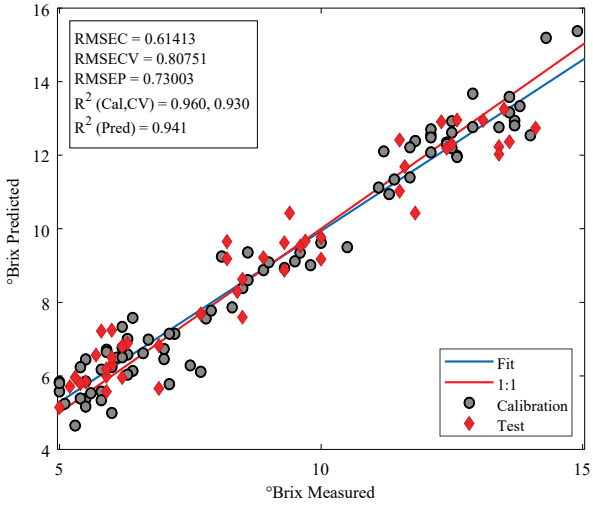

Fig. 3.2.8 – Measured vs. predicted values of SSC obtained by PLS regression (10 LVs) applying SNV+MC pre-processing, and then selecting the variables with GA.

The spectral and spatial information of each pixel in HS images allowed evaluation of quality parameters of each pixel with chemometric models. Using the PLS models developed after the GA variable reduction, false colour images were obtained. The pixels having similar spectra showed similar colours in the images, and consequently

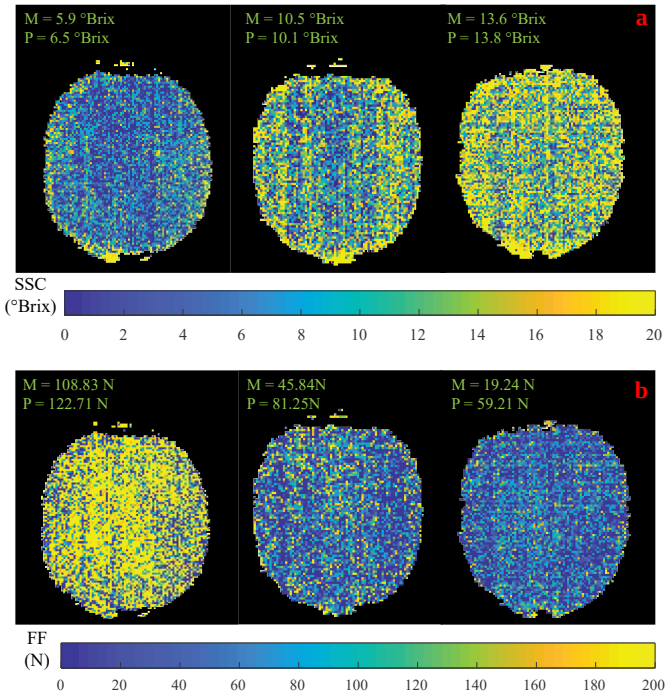

Fig. 3.2.9 – Prediction maps of SSC (a) and FF (b) of three representative kiwifruits. (M: measured value; P: mean predicted value). Peripheral regions have lower signal intensity in hemispherical samples.

the hypercube allowed to visualise the biochemical compounds of a sample in a pixel-wise manner (Zhu et al., 2017). The prediction maps of SSC and FF of three representative kiwifruits (one for each ripening class) are shown in Fig. 3.2.9. The colour bars indicate the scales of the reference values. Measured (M) and mean predicted (P) values are also reported. Spatial distribution of SSC (a) and FF (b) are in alignment with the measured values, particularly passing from 5.9 °Brix/108.83 N to 13.6 °Brix/19.24 N, where the colour ranges from blue/yellow to yellow/blue. As reported by Zhu et al. (2017), the noises of the HS image affected the spectrum of each pixel, which may result in the predicted contents in maps exceeding the range of the calibration set and prediction set.

Results of PLS-DA and *soft* PLS-DA in terms of class sensitivity (percentage of samples correctly recognised as members of the class) are reported in Table 3.2.2 and Table 3.2.3. As for the PLS models, two different pre-processing sequences were adopted, SNV+MC and D1+MC, as well as two variable selection methods, VIP and GA. For both quality parameters, according to Crisosto & Kader (1999), three classes were defined: SSC<6.5, 6.5≤SSC<12.5 and SSC≥12.5; FF≥62, 13≤FF<62 and FF<13.

Considering the PLS-DA models, regardless of pre-processing and variable selection method, lower sensitivity values were achieved for the central classes, reporting values

Table 3.2.2 – Results of PLS-DA and *soft* PLS-DA, in terms of sensitivity, developed to classify the samples according to SSC (class 1 = SSC<6.5; class 2 = 6.5≤SSC<12.5; class 3 = SSC≥12.5).

Spectra pre-processing	Variable selection (nv)	Classes of qualitative index	Sensitivity (%)			
			PLS-DA		*Soft* PLS-DA	
			Calibration	Prediction	Calibration	Prediction
SNV+MC	All (260)	class 1	97	83	97	67
		class 2	79	62	97	92
		class 3	94	75	100	100
	VIP (104)	class 1	97	62	97	77
		class 2	84	77	92	77
		class 3	100	100	100	100
	GA (47)	class 1	93	77	93	100
		class 2	78	58	92	92
		class 3	78	58	92	92
D1+MC	All (260)	class 1	91	100	94	91
		class 2	77	62	100	92
		class 3	93	70	100	100
	VIP (58)	class 1	86	93	97	100
		class 2	78	68	98	100
		class 3	87	89	100	89
	GA (78)	class 1	94	100	94	100
		class 2	72	71	97	88
		class 3	89	82	100	83

Note: SNV = standard normal variate; MC = mean centred; D1 = first derivative; SSC = soluble solids content; nv = number of variables selected; All = all variables; VIP = variable importance in projection; GA = genetic algorithms; PLS-DA = partial least squares discriminant analysis.

Table 3.2.3 – Results of PLS-DA and *soft* PLS-DA, in terms of sensitivity, developed to classify the samples according to FF (class 1 = FF≥62; class 2 = 13≤FF<62; class 3 = FF<13).

Spectra pre-processing	Variable selection (nv)	Classes of qualitative index	Sensitivity (%)			
			PLS-DA		*Soft* PLS-DA	
			Calibration	Prediction	Calibration	Prediction
SNV+MC	All (260)	class 1	100	100	97	100
		class 2	94	86	97	95
		class 3	92	50	100	67
	VIP (97)	class 1	100	95	94	85
		class 2	91	61	94	89
		class 3	100	75	100	100
	GA (72)	class 1	94	100	97	78
		class 2	89	77	97	88
		class 3	83	83	100	100
D1+MC	All (260)	class 1	91	84	100	86
		class 2	72	55	97	94
		class 3	91	93	100	100
	VIP (41)	class 1	97	95	95	89
		class 2	81	77	97	91
		class 3	83	100	92	83
	GA (75)	class 1	100	96	97	78
		class 2	89	83	94	94
		class 3	92	100	100	100

Note: SNV = standard normal variate; MC = mean centred; D1 = first derivative; FF = flesh firmness; nv = number of variables selected; All = all variables; VIP = variable importance in projection; GA = genetic algorithms; PLS-DA = partial least squares discriminant analysis.

from 58 to 77% and from 55 to 86% for SSC and FF, respectively. For both quality parameters, considering the overall sensitivity (SSC=84% and FF=93%), the best models were obtained applying the D1+MC pre-processing and selecting the variables (78 and 75) by GA. PLS-DA prediction plots for FF are presented in Fig. 3.2.10. As shown in Fig. 3.2.10a (Y predicted = FF≥62), there is a clear separation between samples belonging to the FF≥62 class and the other samples. In Fig. 3.2.10b (Y predicted = 13≤FF<62) and Fig. 3.2.10c (Y predicted = FF<13), some samples of classes 13≤FF<62 and FF<13 are overlapping, suggesting that the samples of the two groups, are quite similar. Nevertheless, it can be observed that almost all samples belonging to Y predicted class, were correctly classified.

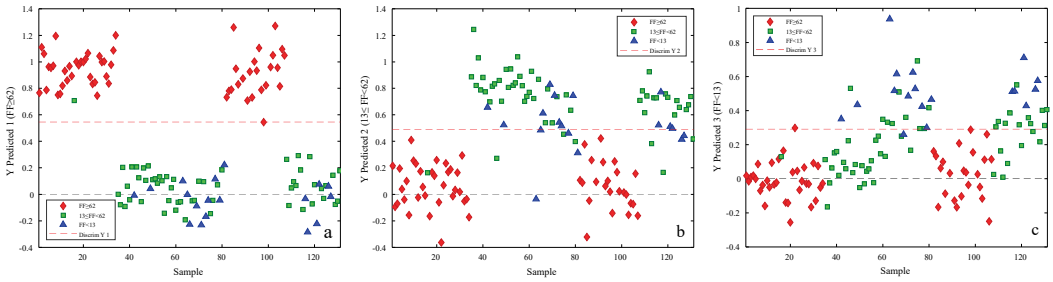

Fig. 3.2.10 – PLS-DA prediction plots for FF applying D1+MC pre-processing and GA variables selection method.

Soft PLS-DA can simultaneously attribute a sample to multiple classes. In addition, a sample may not be attributed at all, if the distance between sample and class is greater than the set critical threshold. In this study, the outlier significance level (γ) was set to 0.01 (Pomerantsev & Rodionova, 2018). Regarding the *soft* PLS-DA models developed to classify the samples according to the SSC, the best results (overall sensitivity = 97%) was obtained applying SNV+MC pre-processing and selecting variables (47) by GA. In prediction, all samples of the classes SSC<6.5 and SSC≥12.5 were correctly classified, while 2 samples of the class 6.5≤SSC<12.5 were not (Fig. 3.2.11a). For FF, the best result (overall sensitivity = 93%) was obtained by considering all the variables and applying D1 pre-processing. In Fig. 3.2.11b, it can be observed that all samples of class FF≥62 were correctly classified. Furthermore, the separation of class FF≥62 from the other two classes is evident, as the acceptance area of the class bound by the ellipsoid is well separated from the others.

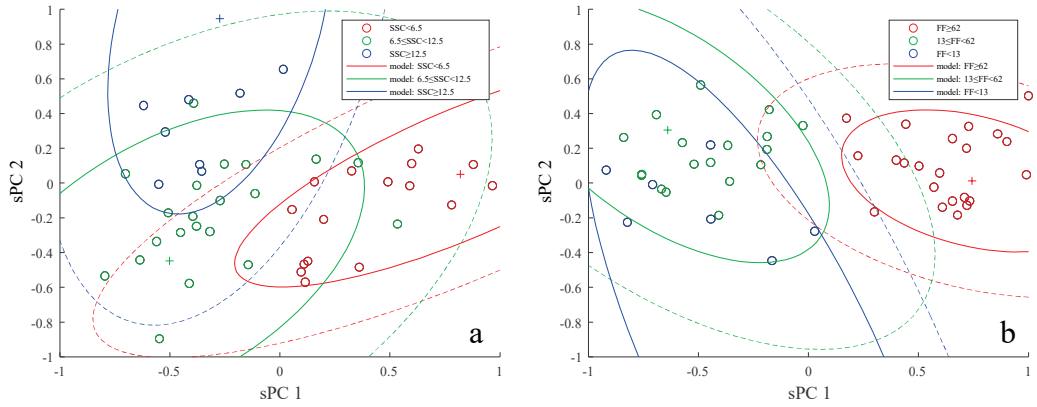

Fig. 3.2.11 – *Soft* PLS-DA prediction plots for: (a) SSC applying SNV+MC pre-processing and GA variable selection method; (b) FF applying D1+MC pre-processing and selecting all variables.

Comparing PLS-DA and *soft* PLS-DA results, it is possible to state that for SSC, regardless of pre-processing and variable selection method, notably higher sensitivity values were achieved by using *soft* PLS-DA. Instead, for FF, the sensitivity values obtained by the two discrimination methods are comparable. Overall sensitivities are higher than those reported in the literature for similar ripening classes defined on green-fleshed kiwifruit (82.0% for SSC and 74.0% for FF) and obtained using a detector working on nine wavelengths from 800 to 1100 nm (Yang et al., 2020).

The results show how the maturity class of kiwifruit can be predicted non-destructively even when limiting the number of wavelengths. Overall, the best models were obtained by applying the GA method, which allowed a decrease of wavelength number by more than 80%. This could be a first step in developing a multispectral equipment to sort kiwifruits directly on-line. In the light of what was observed during laboratory trials,

it is necessary to highlight some choices that affected the success of the experiment. The angle of inclination of the lamps affects the extension of the areas of light reflection and shadows on the surface of the fruit. In the case of the kiwifruit variety under analysis, light reflection is attenuated by the presence of hairs on the skin, so that it is possible to reduce the angle of inclination of lamps with respect to the plane. The black surface of the conveyor belt was useful as it was easy to exclude from HS images by 2-class k-means classification, which also allowed elimination of shaded or poorly illuminated parts of fruits.

3.2.4. Conclusions

The application of HSI combined with chemometric techniques (PLS and PLS-DA), allowed estimation of the FF and SSC of kiwifruit and to classify samples according to ripening classes. Prediction and classification performances remained substantially unchanged by reducing the number of wavelengths, and thus it is expected that a less expensive multispectral camera in the 400–1000 nm range would work just as well. Regarding SSC, the prediction R^2 values ranged from 0.85 (RMSE=1.10 °Brix) to 0.94 (RMSE=0.73 °Brix), and for FF from 0.82 (RMSE=14.51 N) to 0.92 (RMSE=9.87 N). Classification sensitivity reached of 97% and 93% for the model considering the SSC and FF classes, respectively. Considering the results obtained, HSI technology could be implemented in a sorting line of kiwifruit or portable multispectral equipment for the fresh market, but the segmentation techniques, dimensionality reduction, and automated real time analysis need to be improved upon.

3.2.5. References

Alós, E., Rodrigo, M. J., & Zacarias, L. (2019). Ripening and senescence. In E. M. Yahia (Ed.), *Postharvest Physiology and Biochemistry of Fruits and Vegetables* (pp. 131–155). Elsevier. https://doi.org/10.1016/B978-0-12-813278-4.00007-5

ASABE Standard. (2008). ASAE S368.4 DEC2000 (R2008) - Compression Test of Food Materials of Convex Shape. *American Society of Agricultural and Biological Engineers*, *2000*.

Bauchot, A. D., Harker, F. R., & Arnold, W. M. (1999). The use of electrical impedance spectroscopy to assess the physiological condition of kiwifruit. *Postharvest Biology and Technology*, *18*(1), 9–18. https://doi.org/10.1016/S0925-5214(99)00056-3

Berardinelli, A., Benelli, A., Tartagni, M., & Ragni, L. (2019). Kiwifruit flesh firmness determination by a NIR sensitive device and image multivariate data analyses. *Sensors and Actuators, A: Physical*, *296*, 265–271. https://doi.org/10.1016/j.sna.2019.07.027

Blanke, M. M. (2013). Non-invasive Assessment of Firmness and NIR Sugar (TSS) Measurement in Apple, Pear and Kiwi Fruit. *Erwerbs-Obstbau*, *55*(1), 19–24. https://doi.org/10.1007/s10341-013-0181-3

Camps, C., & Christen, D. (2009). On-tree follow-up of apricot fruit development using a hand-held NIR instrument. *Journal of Food, Agriculture and Environment*, *7*(2), 394–400.

Cantin, C. M., Soto, A., Crisosto, G. M., & Crisosto, C. H. (2011). Evaluation of a non-destructive dry matter sensor for kiwifruit. *Acta Horticulturae*, *913*, 627–632. https://doi.org/10.17660/ActaHortic.2011.913.86

Chandrasekaran, I., Panigrahi, S. S., Ravikanth, L., & Singh, C. B. (2019). Potential of Near-Infrared (NIR) Spectroscopy and Hyperspectral Imaging for Quality and Safety Assessment of Fruits: an Overview. *Food Analytical Methods*, *12*(11), 2438–2458. https://doi.org/10.1007/s12161-019-01609-1

Costa, G., Vidoni, S., Rocchi, L., Cellini, A., Buriani, G., Donati, I., & Spinelli, F. (2015). Innovative non-destructive device for fruit quality assessment and early disease diagnosis. *Acta Horticulturae*, *1096*, 69–78. https://doi.org/10.17660/ActaHortic.2015.1096.4

Crisosto, C. H., & Kader, A. A. (1999). Kiwifruit Postharvest Quality Maintenance Guidelines. In *Davis, CA 95616, US: Department of Pomology, University of California*. https://ucanr.edu/sites/kac/files/123823.pdf

ElMasry, G., Wang, N., ElSayed, A., & Ngadi, M. (2007). Hyperspectral imaging for nondestructive determination of some quality attributes for strawberry. *Journal of Food Engineering*, *81*(1), 98–107. https://doi.org/10.1016/j.jfoodeng.2006.10.016

Farrés, M., Platikanov, S., Tsakovski, S., & Tauler, R. (2015). Comparison of the variable importance in projection (VIP) and of the selectivity ratio (SR) methods for variable selection and interpretation. *Journal of Chemometrics*, *29*(10), 528–536. https://doi.org/10.1002/cem.2736

Gallagher, N. B., & O'sullivan, D. (2020). Selection of representative learning and test sets using the onion method. *White Paper Eigenvector*. https://eigenvector.com/wp-content/uploads/2020/01/Onion_SampleSelection.pdf

Gallagher, N. B., Shaver, J. M., Martin, E. B., Morris, J., Wise, B. M., & Windig, W. (2004). Curve resolution for multivariate images with applications to TOF-SIMS and Raman. *Chemometrics and Intelligent Laboratory Systems*, *73*(1), 105–117. https://doi.org/10.1016/j.chemolab.2004.04.003

Guo, W., Li, W., Yang, B., Zhu, Z. Z., Liu, D., & Zhu, X. (2019). A novel noninvasive and cost-effective handheld detector on soluble solids content of fruits. *Journal of Food Engineering*, *257*(March), 1–9. https://doi.org/10.1016/j.jfoodeng.2019.03.022

Hu, X. F., Lin, M., Fu, J. H., Jiao, L., & Liu, H. J. (2016). Nondestructive hardness assessment of kiwi-fruit using near-infrared spectroscopy. *2016 Sixth International Conference on Instrumentation & Measurement, Computer, Communication and Control (IMCCC)*, 69–72.

https://doi.org/10.1109/IMCCC.2016.109

Hu, X. G., Li, X. L., Park, S. H., Kim, Y. H., & Yang, S. I. (2016). Nondestructive monitoring of kiwi ripening process using colorimetric ethylene sensor. *Bulletin of the Korean Chemical Society*, *37*(5), 759–762. https://doi.org/10.1002/bkcs.10745

Li, H., Pidakala, P., Billing, D., & Burdon, J. (2016). Kiwifruit firmness: Measurement by penetrometer and non-destructive devices. *Postharvest Biology and Technology*, *120*, 127–137. https://doi.org/10.1016/j.postharvbio.2016.06.007

Manley, M., Joubert, E., Myburgh, L., Lotz, E., & Kidd, M. (2007). Prediction of soluble solids content and post-storage internal quality of Bulida apricots using near infrared spectroscopy. *Journal of Near Infrared Spectroscopy*, *15*(3), 179–188. https://doi.org/10.1255/jnirs.725

McGlone, V. A., & Kawano, S. (1998). Firmness, dry-matter and soluble-solids assessment of postharvest kiwifruit by NIR spectroscopy. *Postharvest Biology and Technology*, *13*(2), 131–141. https://doi.org/10.1016/S0925-5214(98)00007-6

Mehmood, T., Liland, K. H., Snipen, L., & Sæbø, S. (2012). A review of variable selection methods in Partial Least Squares Regression. *Chemometrics and Intelligent Laboratory Systems*, *118*, 62–69. https://doi.org/10.1016/j.chemolab.2012.07.010

Mellidou, I., Georgiadou, E. C., Kaloudas, D., Kalaitzis, P., Fotopoulos, V., & Kanellis, A. K. (2019). Vitamins. In E. M. Yahia (Ed.), *Postharvest Physiology and Biochemistry of Fruits and Vegetables* (pp. 359–383). Elsevier. https://doi.org/10.1016/B978-0-12-813278-4.00017-8

Mishra, V. K., & Gamage, T. V. (2020a). Postharvest Handling and Treatments of Fruits and Vegetables. In M. S. Rahman (Ed.), *Handbook of Food Preservation* (3rd Ed, pp. 45–60). CRC Press. https://doi.org/10.1201/9780429091483-6

Mishra, V. K., & Gamage, T. V. (2020b). Postharvest Physiology of Fruits and Vegetables. In M. S. Rahman (Ed.), *Handbook of Food Preservation* (3rd Ed, pp. 25–43). CRC Press. https://doi.org/10.1201/9780429091483-5

Nicolaï, B. M., Beullens, K., Bobelyn, E., Peirs, A., Saeys, W., Theron, K. I., & Lammertyn, J. (2007). Nondestructive measurement of fruit and vegetable quality by means of NIR spectroscopy: A review. *Postharvest Biology and Technology*, *46*(2), 99–118. https://doi.org/10.1016/j.postharvbio.2007.06.024

O'Toole, M. D., Marsh, L. A., Davidson, J. L., Tan, Y. M., Armitage, D. W., & Peyton, A. J. (2015). Non-contact multi-frequency magnetic induction spectroscopy system for industrial-scale bio-impedance measurement. *Measurement Science and Technology*, *26*(3). https://doi.org/10.1088/0957-0233/26/3/035102

OECD. (2008). Kiwifruit - International Standardisation of Fruit and Vegetables. In *OECD*. OECD. https://doi.org/10.1787/9789264044272-en-fr

Pomerantsev, A. L., & Rodionova, O. Y. (2018). Multiclass partial least squares discriminant analysis: Taking the right way—A critical tutorial. *Journal of Chemometrics*, *32*(8), 1–16. https://doi.org/10.1002/cem.3030

Pu, H., Liu, D., Wang, L., & Sun, D. W. (2016). Soluble Solids Content and pH Prediction and Maturity Discrimination of Lychee Fruits Using Visible and Near Infrared Hyperspectral Imaging. *Food Analytical Methods*, *9*(1), 235–244. https://doi.org/10.1007/s12161-015-0186-7

Ragni, L., Cevoli, C., Berardinelli, A., & Silaghi, F. A. (2012). Non-destructive internal quality assessment of "hayward" kiwifruit by waveguide spectroscopy. *Journal of Food Engineering*, *109*(1), 32–37. https://doi.org/10.1016/j.jfoodeng.2011.10.002

Rinnan, Å., van den Berg, F., & Engelsen, S. B. (2009). Review of the most common pre-processing techniques for near-infrared spectra. *TrAC Trends in Analytical Chemistry*, *28*(10), 1201–1222. https://doi.org/10.1016/j.trac.2009.07.007

Sánchez-Rodríguez, L., Syd Ali, N., Cano-Lamadrid, M., Noguera-Artiaga, L., Lipan, L., Carbonell-Barrachina, Á. A., & Sendra, E. (2019). Flavors and aromas. In E. M. Yahia (Ed.), *Postharvest Physiology and Biochemistry of Fruits and Vegetables* (pp. 385–404). Elsevier. https://doi.org/10.1016/B978-0-12-813278-4.00019-1

Schaare, P. N., & Fraser, D. G. (2000). Comparison of reflectance, interactance and transmission

modes of visible-near infrared spectroscopy for measuring internal properties of kiwifruit (Actinidia chinensis). *Postharvest Biology and Technology*, *20*(2), 175–184. https://doi.org/10.1016/S0925-5214(00)00130-7

Serranti, S., Bonifazi, G., & Luciani, V. (2017). Non-destructive quality control of kiwi fruits by hyperspectral imaging. *Sensing for Agriculture and Food Quality and Safety IX*, *10217*, 102170O. https://doi.org/10.1117/12.2255055

Valero, C., Ruiz-Altisent, M., Cubeddu, R., Pifferi, A., Taroni, P., Torricelli, A., Valentini, G., Johnson, D. S., & Dover, C. J. (2004). Detection of Internal Quality in Kiwi with Time-Domain Diffuse Reflectance Spectroscopy. *Applied Engineering in Agriculture*, *20*(2), 223–230. https://doi.org/10.13031/2013.15879

Walsh, K. B., McGlone, V. A., & Han, D. H. (2020). The uses of near infra-red spectroscopy in postharvest decision support: A review. *Postharvest Biology and Technology*, *163*, 111139. https://doi.org/10.1016/j.postharvbio.2020.111139

Wang, Z. X., He, Q. P., & Wang, J. (2015). Comparison of variable selection methods for PLS-based soft sensor modeling. *Journal of Process Control*, *26*(2015), 56–72. https://doi.org/10.1016/j.jprocont.2015.01.003

Watkins, C. B. (2017). Postharvest Physiology of Edible Plant Tissues. In S. Damodaran & K. L. Parkin (Eds.), *Fennema's Food Chemistry* (5th Ed, pp. 1017–1085). CRC Press. https://doi.org/10.1201/9781315372914-19

Yang, B., Guo, W., Huang, X., Du, R., & Liu, Z. (2020). A portable, low-cost and sensor-based detector on sweetness and firmness grades of kiwifruit. *Computers and Electronics in Agriculture*, *179*, 105831. https://doi.org/10.1016/j.compag.2020.105831

Zhu, H., Chu, B., Fan, Y., Tao, X., Yin, W., & He, Y. (2017). Hyperspectral Imaging for Predicting the Internal Quality of Kiwifruits Based on Variable Selection Algorithms and Chemometric Models. *Scientific Reports*, *7*(1), 1–13. https://doi.org/10.1038/s41598-017-08509-6

Zontov, Y. V., Rodionova, O. Y., Kucheryavskiy, S. V., & Pomerantsev, A. L. (2020). PLS-DA – A MATLAB GUI tool for hard and soft approaches to partial least squares discriminant analysis. *Chemometrics and Intelligent Laboratory Systems*, *203*, 104064. https://doi.org/10.1016/j.chemolab.2020.104064

3.3. Rapid optical method for procyanidins estimation in red wines

Scientific publication – Paper III

Ricci, A., Iaccheri, E., Benelli, A., Parpinello, G. P., Versari, A., & Ragni, L. (2020). Rapid optical method for procyanidins estimation in red wines. *Food Control, 118,* 107439. https://doi.org/10.1016/j.foodcont.2020.107439

Arianna Ricci[a], Eleonora Iaccheri[b]*, Alessandro Benelli[a], Giuseppina P. Parpinello[a,b], Andrea Versari[a,b], Luigi Ragni[a,b]

[a]*Department of Agricultural and Food Sciences, Alma Mater Studiorum, University of Bologna, P.zza Goidanich 60, 47521 Cesena, FC, Italy*

[b]*Inter-Departmental Centre for Agri-Food Industrial Research, Alma Mater Studiorum, University of Bologna, P.zza Goidanich 60, 47521 Cesena, FC, Italy*

**Corresponding Author: eleonora.iaccheri4@unibo.it*

Abstract

The present work outlines a reliable and rapid optical method to estimate tannin content in red wines. The method originates from the known reactivity of wine tannins (procyanidins) with proteinaceous matter (*i.e.* gelatin) which reaction results in a cloudiness due to the formation of floating procyanidin-protein complexes in solution. An optical device operating with a wavelength-sensitive pulsed electromagnetic source enabled to measure the extent of turbidity, combining the different intensity and spectral emission of a light source (tungsten lamp) with the photodiode wavelength sensitivity. In this experiment, 27 red wines (tannins content range: 6–1904 mg/L) were optically measured at the room temperature immediately after mixing with a saturated solution of gelatin in model wine buffer (12% ethanol, pH 3.5). An output signal waveform (voltage, V) was produced and modified as a function of peak intensity, amplitude and curvature depending on the extent of turbidity. The relationship was fitted obtaining a significant not-linear correlation (R^2 up to 0.9657) with tannins content as determined using a reference colorimetric method. The proposed new optical method is easy and cost-effective and provides a reliable alternative to the time-consuming analyses for fast in-line and off-line analysis of procyanidins in wine.

Keywords: Red wine procyanidins; tannin assay; in-line rapid measurements; decision support system; Spectral-sensitive pulsed photometry.

3.3.1. Introduction

Wine is consumed worldwide with great impact on both production and consumption level. The most recent annual release after the International Organization of Vine and Wine (OIV) highlighted that wine production has reached a record level in 2018, with a global trend of 293 million hectoliters (*State of the vitiviniculture world market, State of the sector in 2018,* released in April 2019). Winemakers aims at improving the quality of their wines to boost the consumer preference (Tempere et al., 2019; Di Vita et al., 2019), and in this view there is a need of new tools to control the process and the products.

Polyphenolic compounds have a great importance on wine composition due to their antioxidant and antimicrobial properties, and their sensory attributes (Santos-Buelga & Freitas, 2009). Natural condensed tannins derived from grapes (*i.e.* procyanidins) are especially abundant in red wines, affecting their mouthfeel properties in terms of bitterness and astringency (Gambuti et al., 2012; Gambuti et al., 2019). Furthermore, procyanidins in wine can be either derived from the grapes and/or added as exogenous processing aids (Harbertson et al., 2012; Versari et al., 2013). A detailed study on tannins involves the use of expensive and/or time-consuming techniques (gravimetric methods, colorimetric methods, vibrational spectroscopy, mass spectroscopy) with intensive sample preparation, periodic instrument calibrations and maintenance in order to obtain satisfactory results, along with qualified personnel for the interpretation of data (Herderich & Smith, 2005; Jensen et al., 2008; Ricci et al., 2017; Nel, 2018; Billerach et al., 2020). This is rarely the case of wine companies that require rapid and reliable analyses and the possibility to monitor the evolution of the industrial process with in-line measurements.

The tannins have traditionally been used in the leather industry for their ability to inhibit the decomposition of collagen protein in the animal tissues, stabilizing it through the formation of hydrogen bonds between phenolic groups and peptides moieties. The reactivity of procyanidins toward proline-like proteins contained in the human saliva is also the basis for the astringency perceived during wine tasting (Maier et al., 2017; Ramos-Pineda et al., 2020).

The formation of procyanidin-protein complexes in the presence of an excess of protein produces a colloidal suspension with the formation of a whitish haze. When a colloidal suspension is irradiated with a light beam in the visible light region (Vis)

there is a balance between part of the light, which is transmitted across the suspension, absorbed, and removed by scattering. The presence of internal interferences due to particles size, concentration and orientation makes hard to reproduce the results in typical UV-Vis and IR transmission/reflectance spectrophotometric experiments (Doty & Steiner, 1950). Recently, an innovative technique named Spectral-Sensitive Pulsed Photometry (SSPP) has been successfully applied to the prediction of fat content in milk; in the experiment, a simple and inexpensive device has been used to exploit key optical properties of commercial milk samples, such as light scattering according to the Mie theory. Theoretical basis for the Spectral-Sensitive Pulsed Photometry are detailed in Ragni et al. (2016). Briefly, while differing from the traditional spectroscopy techniques, the SSPP technique proposed by the authors maintains a sensitivity to the wavelength of the radiation used and the optical response depends on the material under test to a pulsed source of radiation (tungsten filament bulb lamp). When the source is progressively lighted, the output voltage pulse takes a characteristic shape (peak, amplitude, curvature) as function of interposed medium; by exploiting the spectral sensitivity of photodiodes, the device enables to measure the relevant optical phenomena involved in the attenuation of the source intensity, such as light scattering, but also molecular vibrational absorbance (Ragni et al., 2016).

Results obtained in the prediction of fat content in milk has encouraged the application of the SSPP technique in the analysis of the procyanidin content in wine. In this study an innovative tool for the fast quantification of wine procyanidins based on their selective reactivity against proteins is proposed. A selection of commercial red wines from different grape varietals were used for the purposes of this experiment; a voltage/time curve obtained after irradiation in SSPP was processed for the prediction of wine procyanidins and the Adams-Harbertson colorimetric assay (Harbertson et al., 2002).

3.3.2. Materials and methods

3.3.2.1. Chemicals

Working solvents, including absolute ethanol (ACS grade, ≥99.5%) and L(+)-tartaric acid (ACS grade, ≥99.5%) used to prepare the synthetic wine (buffer solution containing 12% ethanol in MilliQ water, 5% tartaric acid, pH 3.5) were purchased from Merck (Merck Millipore, Darmstadt, Germany).

The (+)-catechin monohydrate standard (≥98%) used to calibrate the colorimetric method was purchased from Sigma-Aldrich (St. Louis, MO).

The gelatin used for the optical measurements was a spray-dried powder from bovine skin and it was purchased from Sigma-Aldrich (St. Louis, MO).

3.3.2.2. Wine samples

Twenty-seven red wines, including Cabernet Sauvignon, Merlot, Lambrusco Gasparossa, Sangiovese, Sagrantino di Montefalco, Raboso del Piave, Primitivo di Manduria, Cannonau, Aglianico del Vulture, Teroldego and Nebbiolo (vintages 2016-2018) were selected to cover a wide range of tannin content (Table 3.3.1). Samples were stored at room temperature in glass bottles, capped with different closures (cork, synthetic cork, screw caps, crown caps) and preserved from light and temperature fluctuations. Bottles were opened immediately before the analysis.

Table 3.3.1 – Procyanidin contents measures by the Adams-Harbertson assay and correspondent values of the signal voltage measured with the SSPP photometer.

Sample wine (nr)	Tannins (mg/L CE)		P (V)		BR (V)	
	Mean	SD	Mean	SD	Mean	SD
1	480	22	2.98	0.03	0.124	0.010
2	443	22	2.74	0.03	0.106	0.009
3	97	5	4.08	0.03	0.182	0.012
4	246	18	3.29	0.03	0.139	0.010
5	1786	22	0.95	0.02	0.012	0.004
6	1855	76	0.99	0.01	0.015	0.003
7	1522	20	1.06	0.02	0.021	0.006
8	1005	40	1.94	0.01	0.072	0.005
9	39	1	3.48	0.01	0.156	0.000
10	740	19	2.47	0.02	0.102	0.005
11	618	41	2.92	0.02	0.121	0.008
12	1170	42	1.76	0.01	0.062	0.004
13	699	18	2.81	0.03	0.114	0.011
14	1452	44	1.45	0.02	0.042	0.003
15	976	18	2.12	0.01	0.079	0.006
16	1017	19	1.66	0.02	0.062	0.003
17	970	20	1.91	0.01	0.067	0.005
18	877	46	2.26	0.03	0.088	0.007
19	795	43	2.2	0.03	0.082	0.007
20	1164	18	1.69	0.01	0.056	0.004
21	652	47	2.61	0.01	0.105	0.006
22	820	44	2.09	0.02	0.078	0.008
23	258	17	3.33	0.03	0.146	0.010
24	6	0	3.64	0.03	0.155	0.007
25	538	22	2.65	0.01	0.111	0.002
26	1555	79	1.23	0.00	0.033	0.002
27	1904	100	1.02	0.00	0.018	0.003

Legend: CE, equivalent of (+)-catechin; P, voltage peak value; BR, voltage corresponding to the best R^2 value for quadratic regression.

3.3.2.3. Analysis of procyanidins content in wine

Wines were analyzed in duplicate by the well-known Adams-Harbertson colorimetric assay (Harbertson et al., 2002). Calibration was performed using (+)-catechin as a reference standard and results were expressed as mg/L (+)-catechin equivalents (mg/L CE).

3.3.2.4. Theoretical premises to the optical methodology

To meet winery needs for new rapid tools for tannin analysis it is necessary to overcome the limitations of the classic precipitation-colorimetric assay, including: (i) the need for a preparative step, to isolate tannins from monomeric polyphenolic compounds, and (ii) the long incubation times requested in the stepwise procedure including tannins precipitation, resuspension, and reaction with complexing agents.

In previous experiments, the effectiveness of gelatins to remove polyphenols from wines was investigated, showing their ability to selectively remove condensed tannins (Sarni-Manchado et al., 1999).

At wine pH, these proteins have a positive charge with increasing density in high-molecular weight gelatins or when pH is reduced; these conditions makes gelatin a positively charged polyelectrolyte, producing polar, Van der Waals, H-bonds, London interactions and hydrophobic effects with the negatively charged tannins in wine (Obreque-Slier et al., 2010; Ghanem et al., 2017); a schematic representation of the tannin-protein complex formation is reported in Fig. 3.3.1.

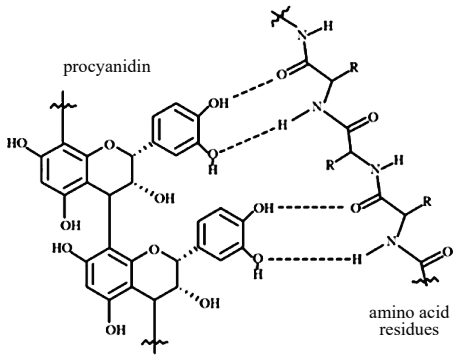

Fig. 3.3.1 – Simplified representation of the chemical interaction occurring between a generic procyanidin molecule and the amino acid residues of a protein.

Binding of ligand to proteins may cause a conformational change in the protein structure, and the same occurs in tannins structure after the formation of protein complexes; these conformational changes result in a diminished solubility (Asquith & Butler, 1986) accompanied by the development of a white haze in solution visible to the naked eye. When adding an excess of gelatin, the number, dimension and extent of such aggregates is regulated by the relative tannin/gelatin ratio (Calderon et al., 1968; Yokotsuka & Singleton, 1987). It follows that the optical properties of the wine sample added with gelatin changes in relation to the tannin content, since the monomeric polyphenols do not display the general property of tannins to form complexes with the amino acid residues of proteins (Haslam, 1998).

Interaction of procyanidins with gelatin in model solution has been previously investigated by Calderon et al. (1968), suggesting that the presence of ethanol and low pH values (3.5 in the study) could maximize the positive charges density and speed up the reaction with rapid formation of flocculates and subsequent precipitation. Similar conditions were applied to dissolve gelatin in the SSPP experiment.

Based on these premises, the proposed SSPP method provides the direct measure of the optical turbidity instantly generated by mixing the red wine with a saturated solution of gelatin dissolved in a hydroalcoholic buffer with fixed pH 3.5 value. The extent of turbidity is efficiently measured with optical infrared sensing, typically operating in the near-infrared (NIR) spectral region; radiations over 700 nm interact with suspended particles, with variable yield according to the particles' dimensions (Filella et al., 1997). To maximize the optical response generated by turbidity and to overcome interferences related to wine color during the analysis, the SSPP was equipped with a photodiode operating in the 650–1200 nm region, with a maximum peak around 875 nm where the red wines do not display absorbance (Fig. 3.3.2).

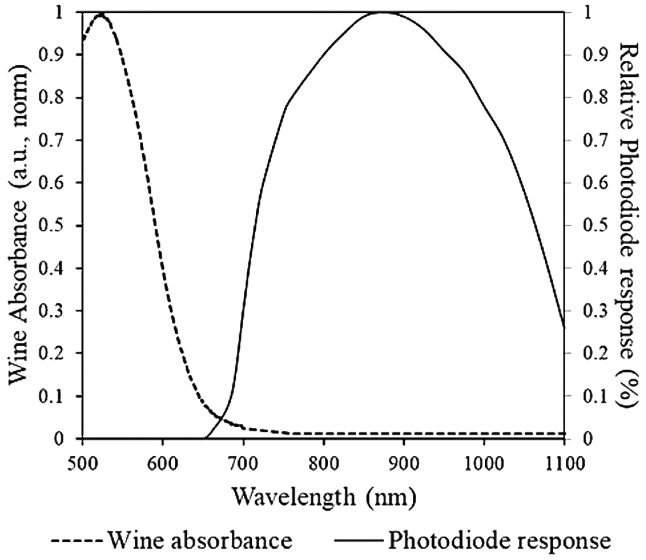

Fig. 3.3.2 – Typical spectral absorption of red wines (dot line) overlapped to the emission spectrum of the photodiode used in the SSPP experiment (black line).

3.3.2.5. SSPP measurements on wines

The prototype and acquisition setting up used in this experiment are detailed in Ragni et al. (2016). Wine samples were directly mixed with a saturated solution of gelatin (30 g/L in model wine buffer) in ratio 1:1 (v/v) to enable the reaction with formation of the colloidal suspension, then immediately inserted in the sample compartment of the optical device and irradiated with the pulsed source, as shown in Fig. 3.3.3. For each wine-gelatin mixture, five subsequent voltage pulses were acquired and averaged.

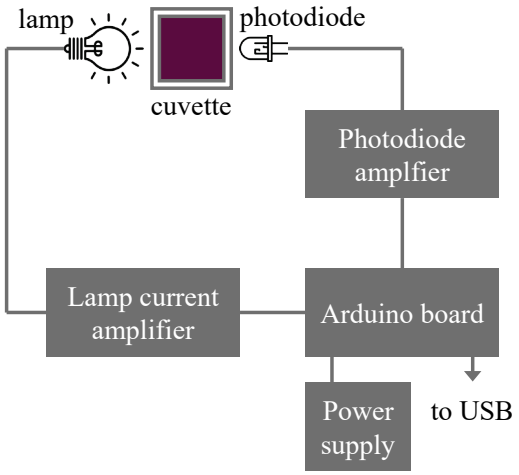

Fig. 3.3.3 – Simplified layout of the used prototype.

3.3.2.6. Statistical analysis

Simple regression was used to analyze the signal waveform. Models with different functions were exploited to fit the data set and estimate tannin contents. Models were built for each of the 187 waveforms points, with signal (V) as x and tannins (mg/L) as f(x). On the whole, the coefficient of determination later shows how the quadratic model is the best suited for data interpolation. The best results in terms of coefficient of determination was selected among all the points of the signal waveform as indicator of the best estimation model. Additional parameters were calculated and reported for a comprehensive regression characterization: adjusted R^2, p-level of each function coefficient, 95% confidence and prediction limits.

3.3.3. Results and discussion

3.3.3.1. Procyanidin content of wines

Average values and standard deviation of the procyanidin content of red wines and the photometric parameters are reported in Table 3.3.1.

The amount of tannins in red wines was highly variable, as expected. The mean red wine contained 877 mg/L CE with a coefficient of variation corresponding to 62.3% of the averaged value. The variation of the tannin's concentration was up to three orders of magnitude.

3.3.3.2. Determination of red wine procyanidins using the SSPP method

The amount of turbidity, as a function of procyanidin concentration, has a clear effect on the pulsed light signal detected by the photometer. The radiation at these

wavelengths strongly interacts with matter giving a response in terms of light scattering, function of the chemical-physical parameters of the analysed samples and allowing the tannins content evaluation. The voltage signals for the different wines with different tannins content, as a function of the lighting time of the lamp (time during which the lamp lights up, becomes brighter and suddenly blow out) are shown in Fig. 3.3.4.

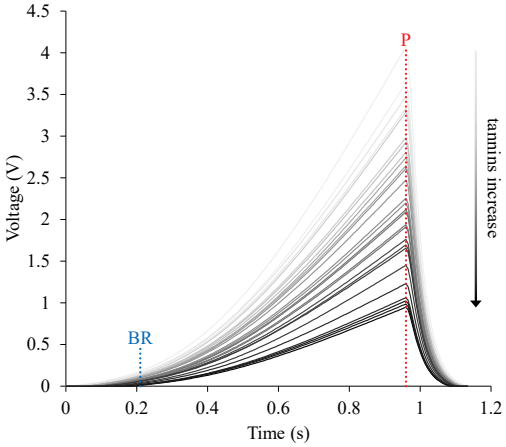

Fig. 3.3.4 – Voltage (V) signals vs. lighting time (s). P: peak time; BR: time corresponding to the highest R^2 for quadratic regression.

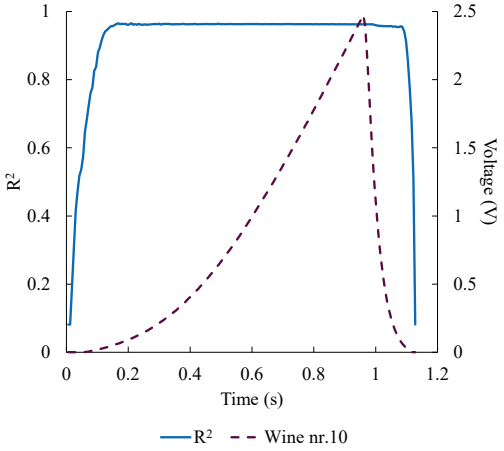

Fig. 3.3.5 – Continuous line: coefficient of determination (R^2) for quadratic regression and for all points of the waveform. Dashed line: voltage (V) signals vs. lighting time (s) of a sample of wine nr. 10 as an example.

The raise of tannins content enhances the turbidity reaction and a less intensity signal was revealed. The maximum peak voltage and the waveforms modifications of different wines, characterized by variable tannins content, are dependent on the spectral component of light, the interaction of light with sample and the spectral sensitivity of the photodiode. The voltage peak values and the voltage at the most

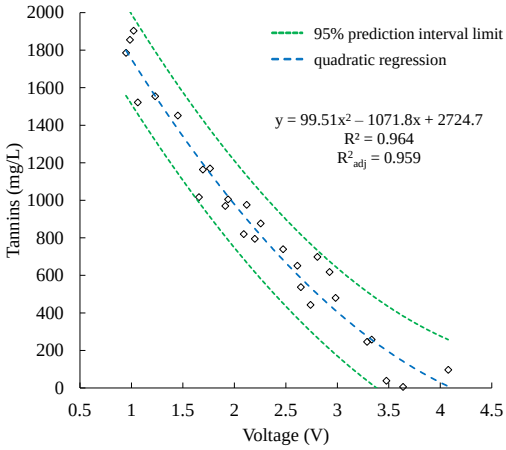

Fig. 3.3.6 – Tannin content vs. voltage at voltage peak value.

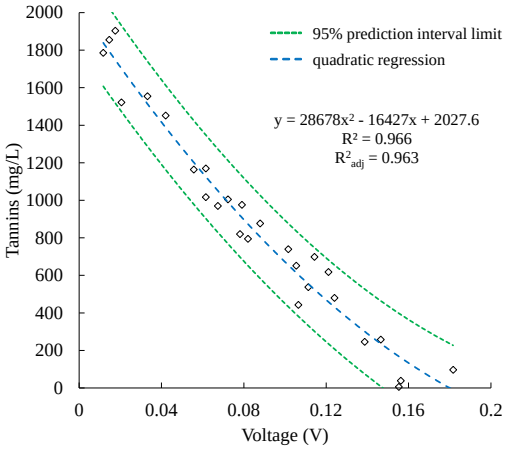

Fig. 3.3.7 – Tannins content vs. voltage at t the time providing the highest R^2 value.

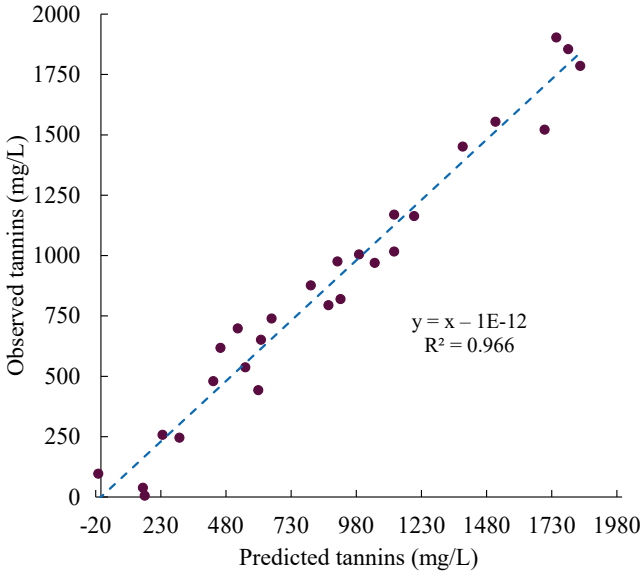

Fig. 3.3.8 – Observed vs. estimated tannins content at the time with the highest coefficient of determination.

sensitive points (at the time giving the highest R^2 value) were used to create models to estimate the tannins content. A quadratic regression was performed between each spectral point and the tannins content. The coefficient of determination values for all the waveform points are shown in Fig. 3.3.5.

From this figure it can be noted that the R^2 is high for a large part of the waveform signal (lamp lighting) with a maximum at 0.21 s (voltage peak is at 0.96 s). Fig. 3.3.6 and Fig. 3.3.7 show the quadratic regression between tannins content and the voltage peak and at the point (time) the highest coefficient of determination was obtained, respectively.

Observed and estimated values by means of equation in Fig. 3.3.7 were regressed in Fig. 3.3.8.

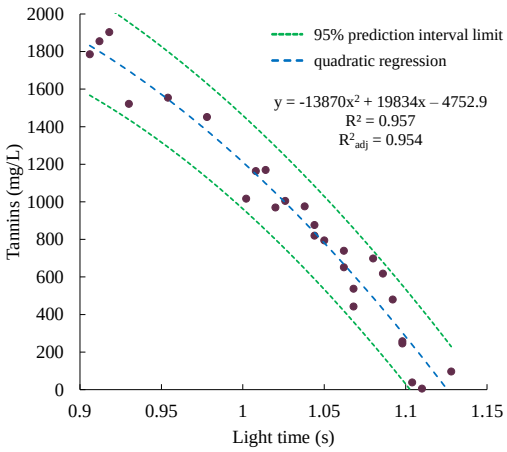

Fig. 3.3.9 – Tannins content vs. light time (quadratic regression).

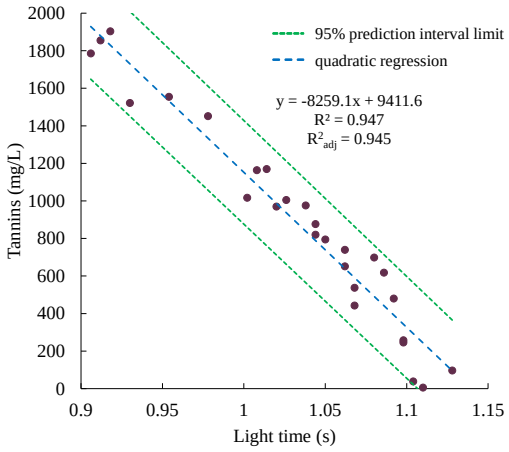

Fig. 3.3.10 – Tannins content vs. light time (linear regression).

A quadratic regression with high R^2 (0.957) was also obtained for the simple light time (time during which the output voltage is not 0). However, not all the coefficients of x and the intercept were significant (see the subsequent analysis in Table 3.3.2), so a linear regression was calculated with very limited loss of correlation. Fig. 3.3.9 and Fig. 3.3.10 show the quadratic and linear regression for the light time. In Table 3.3.2 the main parameters related to the significance of the regression were reported.

Table 3.3.2 – Main statistical parameters for the calculated regressions.

Equation in figure	Equation coefficients	Estimate	Standard error	p-value	95% Lower confidence limit	95% Upper confidence limit
6	a	99.51	27	0.0012	43.39	155.6
	b	-1072.83	130	0.0000	-1340	-804
	c	2725	142	0.0000	2431	3019
7	a	28678	8829	0.0034	10456	46900
	b	-16427	1632	0.0000	-19796	-13058
	c	2028	67	0.0000	1889	21656
9	a	-13870	5797	0.0249	-25833	-1907
	b	19834	11746	0.1042	-4409	44077
	c	-4753	5931	0.4307	-16994	7489
10	b	-8259	391	0.0000	-9065	-7453
	c	9412	405	0.0000	8577	10246

Legend: a, x^2 coefficient; b, x coefficient; c, intercept.

From graphical and tabulated results, it can be observed that the tannins content is correlated to the peak voltage and the most sensitive point voltage with a coefficient of determination of 0.963 and 0.966 (RMSE 104 mg/L and 99 mg/L), respectively. No substantial differences emerged by using one or the other voltage, the R^2 value remains high for most of the signal points (Fig. 3.3.5). The estimation of the tannins content by means of the light time gives a coefficient of determination of 0.947 (RMSE 124 mg/L). The nonlinear correlation between tannins and detected light signal could be attributed to a certain amount of saturation of the turbidity increasing with the tannins content. Previous work also reported nonlinear relation among light signal and quality parameters of dairy products (Ragni et al., 2016).

3.3.4. Conclusion

In light of the results obtained, pulsed photometry, based on the interaction of the spectrally variable light radiation and the interposed wine, reacted with gelatin, has proven to be a technique capable of estimating the tannins content in wine with appreciable precision. The highest R^2 value, obtained with a quadratic regression function, was 0.966 with a RMSE value of 99 mg/L.

Considering the regression calculated with the voltage peak of wine with different procyanidin content, a slightly lower coefficient of determination (0.963) was

obtained, with an RMSE of 104 mg/L. The highest coefficient of determination can be attributed to the initial lighting of the lamp, characterized by a large amount of infrared radiation. In summary, the peak value already provides an estimation of the tannin content. A simple linear regression calculated with the time with the photodiode detect a measurable signal gives R^2 values of 0.947 (RMSE 124 mg/L).

Further samples are mandatory to perform the statistical model implementation in reason to afford the light pulsed contribution in procyanidin content assessment. Multivariate techniques, such PLS and neural network could be used to attempt to improve the model power, which however seems good enough for the estimation of tannins in red wines.

Acknowledgement

The present study has been performed in the context of the PCT patent application titled “System, method and device for detecting tannins in a liquid”, nr PCT/IB2020/051304 filed on 02/17/2020. The patent is still pending.

3.3.5. References

Asquith, T. N., & Butler, L. G. (1986). Interactions of condensed tannins with selected proteins. *Phytochemistry*, *25*(7), 1591–1593. https://doi.org/10.1016/S0031-9422(00)81214-5

Billerach, G., Roumeás, L., Dubreucq, E., & Fulcrand, H. (2020). Furanolysis with Menthofuran: A New Depolymerization Method for Analyzing Condensed Tannins. *Journal of Agricultural and Food Chemistry*, *68*(10), 2917–2926. https://doi.org/10.1021/acs.jafc.9b00497

Calderon, P., Van Buren, J., & Robinson, W. B. (1968). Factors influencing the formation of precipitates and hazes by gelatin and condensed and hydrolyzable tannins. *Journal of Agricultural and Food Chemistry*, *16*(3), 479–482. https://doi.org/10.1021/jf60157a017

Di Vita, G., Caracciolo, F., Brun, F., & D'Amico, M. (2019). Picking out a wine: Consumer motivation behind different quality wines choice. *Wine Economics and Policy*, *8*(1), 16–27. https://doi.org/10.1016/j.wep.2019.02.002

Doty, P., & Steiner, R. F. (1950). Light Scattering and Spectrophotometry of Colloidal Solutions. *The Journal of Chemical Physics*, *18*(9), 1220. https://doi.org/10.1063/1.1747913

Filella, M., Zhang, J., Newman, M. E., & Buffle, J. (1997). Analytical applications of photon correlation spectroscopy for size distribution measurements of natural colloidal suspensions: capabilities and limitations. *Colloids and Surfaces A: Physicochemical and Engineering Aspects*, *120*(1–3), 27–46. https://doi.org/10.1016/S0927-7757(96)03677-1

Gambuti, A., Piombino, P., Pittari, E., Rinaldi, A., Curioni, A., Giacosa, S., Mattivi, F., Parpinello, G. P., Perenzoni, D., Slaghenaufi, D., & Moio, L. (2019). Phenolic parameters explaining different astringency properties in res wines. *ŒnoIVAS 2019: 11th International Symposium of Oenology of Bordeaux and 11th Edition of the Symposium In Vino Analytica Scientia*, 277. https://isvv-events.com/oeno2019-ivas2019/images/pdf/Abstracts book ŒnoIVAS 2019-web.pdf

Gambuti, Angelita, Rinaldi, A., Ugliano, M., & Moio, L. (2012). Evolution of Phenolic Compounds and Astringency during Aging of Red Wine: Effect of Oxygen Exposure before and after Bottling. *Journal of Agricultural and Food Chemistry*, *61*(8), 1618–1627. https://doi.org/10.1021/jf302822b

Ghanem, C., Taillandier, P., Rizk, M., Rizk, Z., Nehme, N., Souchard, J. P., & El Rayess, Y. (2017). Analysis of the impact of fining agents types, oenological tannins and mannoproteins and their concentrations on the phenolic composition of red wine. *LWT - Food Science and Technology*, *83*, 101–109. https://doi.org/10.1016/j.lwt.2017.05.009

Harbertson, J. F., Kennedy, J. A., & Adams, D. O. (2002). Tannin in Skins and Seeds of Cabernet Sauvignon, Syrah, and Pinot noir Berries during Ripening. *American Journal of Enology and Viticulture*, *53*(1), 54–59. https://www.ajevonline.org/content/53/1/54

Harbertson, J. F., Parpinello, G. P., Heymann, H., & Downey, M. O. (2012). Impact of exogenous tannin additions on wine chemistry and wine sensory character. *Food Chemistry*, *131*(3), 999–1008. https://doi.org/10.1016/j.foodchem.2011.09.101

Haslam, E. (1998). *Practical polyphenolics: from structure to molecular recognition and physiological action*. Cambridge University Press.

Herderich, M. J., & Smith, P. A. (2005). Analysis of grape and wine tannins: Methods, applications and challenges. *Australian Journal of Grape and Wine Research*, *11*(2), 205–214. https://doi.org/10.1111/j.1755-0238.2005.tb00288.x

Jensen, J. S., Egebo, M., & Meyer, A. S. (2008). Identification of Spectral Regions for the Quantification of Red Wine Tannins with Fourier Transform Mid-Infrared Spectroscopy. *Journal of Agricultural and Food Chemistry*, *56*(10), 3493–3499. https://doi.org/10.1021/jf703573f

Maier, M., Oelbermann, A. L., Renner, M., & Weidner, E. (2017). Screening of European medicinal herbs on their tannin content—New potential tanning agents for the leather industry. *Industrial Crops and Products*, *99*, 19–26. https://doi.org/10.1016/j.indcrop.2017.01.033

Nel, A. P. (2018). Tannins and anthocyanins: From their origin to wine analysis - A review. *South African Journal of Enology and Viticulture*, *39*(1), 1–20. https://doi.org/10.21548/39-1-1503

Obreque-Slier, E., Lopez-Solis, R., Peña-Neira, Á., & Zamora-Marín, F. (2010). Tannin–protein interaction is more closely associated with astringency than tannin–protein precipitation: experience with two oenological tannins and a gelatin. *International Journal of Food Science & Technology*, *45*(12), 2629–2636. https://doi.org/10.1111/j.1365-2621.2010.02437.x

Ragni, L., Iaccheri, E., Cevoli, C., & Berardinelli, A. (2016). Spectral-sensitive Pulsed Photometry to predict the fat content of commercialized milk. *Journal of Food Engineering*, *171*, 95–101. https://doi.org/10.1016/j.jfoodeng.2015.10.017

Ramos-Pineda, A. M., Carpenter, G. H., Garciá-Estévez, I., & Escribano-Bailón, M. T. (2020). Influence of Chemical Species on Polyphenol-Protein Interactions Related to Wine Astringency. *Journal of Agricultural and Food Chemistry*, *68*(10), 2948–2954. https://doi.org/10.1021/acs.jafc.9b00527

Ricci, A., Parpinello, G. P., Palma, A. S., Teslić, N., Brilli, C., Pizzi, A., & Versari, A. (2017). Analytical profiling of food-grade extracts from grape (Vitis vinifera sp.) seeds and skins, green tea (Camellia sinensis) leaves and Limousin oak (Quercus robur) heartwood using MALDI-TOF-MS, ICP-MS and spectrophotometric methods. *Journal of Food Composition and Analysis*, *59*, 95–104. https://doi.org/10.1016/j.jfca.2017.01.014

Santos-Buelga, C., & Freitas, V. De. (2009). Influence of Phenolics on Wine Organoleptic Properties. *Wine Chemistry and Biochemistry*, 529–570. https://doi.org/10.1007/978-0-387-74118-5_24

Sarni-Manchado, P., Deleris, A., Avallone, S., Cheynier, V., & Moutounet, M. (1999). Analysis and Characterization of Wine Condensed Tannins Precipitated by Proteins Used as Fining Agent in Enology. *American Journal of Enology and Viticulture*, *50*(1), 81–86. https://www.ajevonline.org/content/50/1/81

Tempere, S., Pérès, S., Espinoza, A. F., Darriet, P., Giraud-Héraud, E., & Pons, A. (2019). Consumer preferences for different red wine styles and repeated exposure effects. *Food Quality and Preference*, *73*, 110–116. https://doi.org/10.1016/j.foodqual.2018.12.009

Versari, A., Du Toit, W., & Parpinello, G. P. (2013). Oenological tannins: a review. *Australian Journal of Grape and Wine Research*, *19*(1), 1–10. https://doi.org/10.1111/ajgw.12002

Yokotsuka, K., & Singleton, V. L. (1987). Interactive Precipitation between Graded Peptides from Gelatin and Specific Grape Tannin Fractions in Wine-like Model Solutions. *American Journal of Enology and Viticulture*, *38*(3), 199–206. https://www.ajevonline.org/content/38/3/199

3.4. Kiwifruit flesh firmness determination by a NIR sensitive device and image multivariate data analyses

Scientific publication – Paper IV

A. Berardinelli, A. Benelli, M. Tartagni, L. Ragni, Kiwifruit flesh firmness determination by a NIR sensitive device and image multivariate data analyses, Sensors Actuators A Phys. 296 (2019) 265–271. https://doi.org/10.1016/j.sna.2019.07.027.

A. Berardinelli[a,b*], A. Benelli[c], M. Tartagni[d,e], L. Ragni[c]

[a]*Department of Industrial Engineering, University of Trento, Via Sommarive, 9, 38123 Povo (TN), Italy*

[b]*Centre Agriculture Food Environment, University of Trento, Via E. Mach, 1, 38010 S. Michele all'Adige (TN), Italy*

[c]*Department of Agricultural and Food Science, Alma Mater Studiorum, University of Bologna, Campus of Cesena, Piazza Goidanich 60, 47521 Cesena (FC) Italy*

[d]*Department of Electrical, Electronic and Information Engineering "Guglielmo Marconi" (DEI), University of Bologna, Campus of Cesena, Via dell'Università, 50, 47522 Cesena (FC), Italy*

[e]*Center for Industrial Research on ICT (CIRI ICT), University of Bologna, Via dell'Università, 50, 47522 Cesena (FC), Italy*

Abstract

A prototype based on a NIR sensitive camera and a Xenon lamp was set up and used to capture 8 bit gray scale (from 0=black to 255=white) image of the radiation that passes through the fruit. The count of the pixels with different gray tone was used to build statistical-mathematical models to correlate and predict the kiwifruit flesh firmness. One hundred sixteen fruits conveniently stored to obtain firmness within a range of penetrometric force from 0.8 N to 87 N, were submitted to the optical measurements. Simple regression between the gray tone having the maximum number of pixels and the firmness shown an exponential correlation with R^2 values of 0.717. On the contrary, the tone uniformity (maximum number of the pixels with the same gray tone) resulted linearly correlated with hardness (R^2=0.687). PLS algorithm allowed prediction of the flesh firmness with R^2 of 0.777 (RMSE=13 N). Artificial neural networks given similar results. Although the current technique not fully satisfies the need of an accurate selection, it could be considered for on-line applications by

improving performances (*e.g.,* acting on lamp spectral emissions and camera detection) and with easy mechanical modifications of the sorting lines.

Keywords: Kiwifruit; flesh firmness; infrared-sensitive camera; Partial Least Squares regression (PLS); Artificial Neural Networks (ANN).

3.4.1. Introduction

From 1970 onwards kiwifruit (*Actinidia deliciosa*) has experienced a growing international success largely due to 'Hayward' cultivar selection and commercialization [1]. Kiwifruit has a worldwide production that reached 4,038,871 tons in 2017; Italy is the second largest producer (541,150 tons in 2017, 13.4% of total production) after China (2,024,603 tons in 2017, 50.1% of total production) [2].

Kiwifruits are harvested when 'hardmature', but unripe [3]. It is important to harvest the fruits at the right stage of maturation, as it influences the quality referred to consumption, storage time, fruit management after harvest and disease liability. Kiwifruits are climacteric, hence ripen after picking [4,5]. It has been often observed that, when the harvest is done too early, fruits might undergo a precocious softening during storage, and not reach full-flavour and aroma at ripe [6].

During kiwifruit ripening, an increase in Total Soluble Solids (TSS) can be observed [7]. Kiwi dry matter is mainly composed of carbohydrates and starch, which during ripening gradually transform to soluble solids, such as sugars. For this reason, the percentage of carbohydrates and starch could be taken into account as a kiwi ripeness index [8] and this parameter can be chosen to proceed with harvesting [7].

During storage, kiwi texture changes from hard and crisp to soft and melting. This parameter is important for eating quality, and also for postharvest handling, as storage, grading, and transport [3].

Kiwi firmness can be assessed through destructive techniques, like a penetrometer, and a remarkable variety of non-destructive techniques were proposed.

The correlations between mechanical measurements (compression, impact response and acoustic impulse response) with the penetrometric kiwifruits firmness were investigated and R^2 values from 0.634 to 0.956, depending on the used technique and variety of kiwifruit, were calculated [3].

An impact device equipped with a load cell was set up to measure kiwifruits hardness in a simulated on-line sorting condition. By using multiple regression models with independent variables related to some parameters of the impact force during time (*e.g.,* the peak), R^2 values up to 0.823 were obtained; the use of artificial neural network did not improve the goodness of estimation [9].

A non-destructive instrument, named 'Intelligent Firmness Detector' (IFD), sensing the firmness of peeled fruits with a pressure transducer, was compared with two destructive instruments, an 'ART' and a 'Bareiss' hand-held penetrometer [10]. Correlations (r^2) between kiwifruit firmness measured by means of IFD and destructive instruments were 0.62 and 0.70, respectively. In the same study, a comparison for Total Soluble Solids (TSS, sugar, sweetness, and taste) values was also made adopting a non-destructive VIS-NIR spectrophotometer (five transmission spectra) in the range from 400 to 1100 nm, named 'Intelligent Fruit Analyser' (IFA), and a conventional refractometer.

A non-destructive and low-cost fruit ripeness sensing system named 'FruitSense' was also proposed for kiwi and avocado. It leverages wireless signal emitted by WiFi devices to sense physiological changes related to fruit ripening [8]. The received signals appeared influenced by changes in the physiological compounds of the fruit during ripening. In this study, over the 90% of fruits characterised by four ripeness levels usually implemented by industry (from unripen to over ripen) were correctly classified according to ripening.

Waveguide spectroscopy in two frequency ranges (2−3 GHz and15–16 GHz) was used to predict both soluble solids content and flesh firmness of kiwifruits [11]. Models obtained by partial least squares (PLS) regression algorithms showed test set R^2 values up to 0.804 and 0.806 for the prediction of soluble solids content and Magness-Taylor flesh firmness, respectively.

The non-destructive time-domain diffuse reflectance spectroscopy (TRS) (a pulsed laser spectroscopic technique) was studied to measure kiwifruits quality parameters characterised by optical differences, as firmness, sugar content, and acidity. TRS can be used to estimate, separately and simultaneously, absorbed and scattered light at each wavelength within the sample. It was possible to estimate at the same time firmness and chemical contents. Data obtained from standard methods such as flesh puncture, compression with ball, °Brix (°Bx), total acidity, skin colour, were correlated with non-destructive measures to obtain estimative models, using multivariate analysis. Percentage of correctly classified fruits for firmness into three groups was 75%, 60% for sugar content, and 97% for acidity [12].

The relationship between hardness of kiwifruit, measured by using a HANDPI fruit hardness tester penetrometer, and non-destructive near-infrared diffuse reflectance spectroscopy was studied [13]. The correlation coefficients between predicted and actual hardness values were from 0.896 to 0.977, depending on calibration model (MLR and PLS, respectively).

Costa et al. (2015) [6] set up a portable instrument (Kiwi-Meter) assessing the fruit maturity by means of an index based on the difference in absorbance among specific wavelengths and related to the chlorophyll degradation.

Even a hyperspectral imaging system with a laser as light source was used to predict firmness (R=0.898), sugar (R=0.932) and C vitamin content (R=0.918) of kiwi fruits [14]. Through backscattering imaging, the propagation of laser light in kiwis was measured [15]. Data were modelled with Monte Carlo stochastic method, in order to develop a non-destructive assessment method of kiwis' optical properties. A significant difference, at $p<0.01$, was found between anisotropy of fruits with respect to ripeness grades.

Magnetic resonance imaging (MRI) can be a useful technique to identify minimal changes in fruit texture related to water mobility. The fast softening of kiwifruits during storage at 0◦C appeared related to minimal changes in texture and is probably triggered by ethylene activated at molecular level in response to a wound. Water organisation and mobility affect ripening process, and minimal variation of vapour pressure due to modification in water loss and temperature can alter this organisation inducing textural changes and kiwifruit softening [16]. Kiwifruit is extremely sensitive to minute concentrations of ethylene (5 ppb) [4,5]. Quantitative ^{1}H magnetic resonance (MR) imaging was adopted to detect changes in relaxation times at fixed times intervals during kiwi growth and maturation (*Actinidia deliciosa* var. *deliciosa*). The parameters selected for the analysis were the relaxation times T_1 and T_2 using a Carr-Purcell-Meiboom-Gill pulse sequence (T_2-CPMG). Time trends were found for both the relaxations parameters, and differences between flesh, locule (the seeds have not been taken into account) and core tissue. However, the results obtained by MR did not necessarily reflect the underlying biochemical processes, determined by destructive measurements of free sugars, SSC, macronutrients, and micronutrients [17].

Ethylene gas concentration might be used as an index to establish harvest time of fruit and to control after-harvest ripening of fruits. A colorimetric detection system with commercially available bathophenanthroline-based palladium complex was explored. This sensor changes colour when react with ethylene, which is related to kiwi ripeness [18].

Electronic Nose (EN) combined with a 433 MHz Surface Acoustic Wave Resonator (SAWR) to determine kiwifruit quality in 12 days of storage was tested [19]. Quality predictive models of kiwis based on SAWR, EN and EN combined with SAWR, were developed giving, respectively, R^2 values of 0.865, 0.939, and 0.998. This non-destructive method has some advantages, such as low cost, accuracy, and high analysis speed of fruit quality.

Yen & Yao (2018) [20] considered Volatile Organic Compounds (VOCs) released by in-ripening and over-ripened kiwis. VOCs were detected with a TD-GC/MS (Thermal Desorption Gas Chromatography/Mass Spectrometry) and compared with those detected with a SAW (Surface Acoustic Wave) gas sensor system, coated with four different thin films, which have a specific affinity to VOCs. A database was built up to classify the kiwi fruit during ripeness and over-ripeness.

Information on the properties and cellular structure of a biological sample can be also obtained by measuring its bioimpedance spectra. Fruit ripening is the result of structural and cellular modifications that occur within the fruit itself. These modifications should produce a change in β-dispersion shape, as a result the spectra could be used to indicate the status and evolution of these properties [21]. A multi-frequency magnetic induction spectroscopy (MIS) system designed for industrial-scale was adopted to obtain non-destructive and non-contact spectroscopic bio-impedance measurement, using a bandwidth of 156 kHz–2.5 MHz. The goal is to obtain conductivity spectra of numerous biological test samples, including apples, pears, nectarines, kiwis, potatoes, oranges, tomatoes, and yeast suspensions at different concentrations. This application could be further tested for detection of differences in flesh firmness of kiwifruits based on conductivity spectra.

Most of the above-described methods are difficult to apply in a fruit sorting line, in which the speed is equal to or greater than 10 fruits per second. Without claiming to be an immediate solution, here is presented a simple optical technique that, appropriately developed and improved, could carry out the on-line determination of kiwi hardness.

3.4.2. Materials and methods

3.4.2.1. The device

The main components of the apparatus are a xenon lamp and an infrared-sensitive camera. The lamp is confined in a squared section aluminium tubular container (50×50 mm) having an open end where a fan cooling is housed. In the upper surface of the container, a longitudinal 22×34 mm window has been obtained on which the kiwifruit is positioned. A dark spongy material coats this surface to prevent the light passes through the rough contact between case and fruit. Moreover, a rigid black sheet (210×300 mm) was positioned around to this window to avoid reflections from the aluminium surfaces. A layout of the apparatus is depicted in Fig. 3.4.1. The xenon lamp, for automotive use, was powered by an ignitor for 55 W lamps, supplied at 13 V, 4 A. The emission spectrum of the lamp was detected with a commercialized spectrometer equipped with optic fiber (AvaSpec 2048, Avantes, NL). The camera was

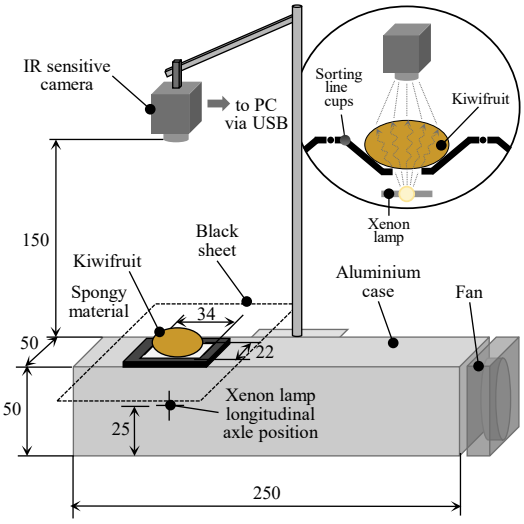

Fig. 3.4.1 – Layout of the assembled device. In the inset a potential on-line application (figure is not to scale).

obtained from a commercialized webcam with 1280×1024 resolution, by replacing the infrared filter with a visible filter. All the apparatus was placed in a shielded container. Images of the kiwifruits were acquired by RGS-AvaCam, v. 3.7.0 software in an 8-bit gray scale (from 0=black to 255=white).

3.4.2.2. Kiwifruits

A sample of 116 kiwifruit (Hayward variety) was picked at commercial harvest in October 2018 in the Romagna area (Italy) to carry out the measurements. About 1/3 of the fruits was stored at 4 °C until test to maintain the flesh firmness high. One third was left to mature at room temperature (22 °C) in the presence of apples, inside a container provided by some openings to avoid excessive accumulation of ethylene. Another third was extracted from the refrigerator after about one day before test and left to ripen in the same conditions of the second batch. This procedure allowed to obtain fruits with a Magness-Taylor flesh firmness (MTf) ranging from about 1 to 90 Newton (N) and a soluble solids content (SSC) from 7 to 16 °Bx.

MTf was measured with a 7.9 mm diameter probe mounted on a compression/traction machine with a load cell conditioned and interfaced with a PC. The SSC was measured by an IR refractometer (PR-1, ATAGO Co. Ltd., Tokyo, Japan). Two measurements, both for MTf and SSC, were carried out on the opposite side of the fruit and the values were averaged.

3.4.2.3. Image analysis

The image analysis, including the distribution (count) of the gray pixels according with the 8-bit scale was carried out with ImageJ software (National Institutes of Health, USA). To avoid or limit possible boundary light effects or other disturbances, only the

oval area inscribed in the kiwifruit was used for image processing. Being the fruits of different size, the number of pixels was normalized before counting.

3.4.2.4. Data analysis

A preliminary statistical analysis was carried out by exploring the correlation between MTf (and SSC) and the main parameters describing the distribution of the gray pixels, such as the tone (from 1 to 255; 0=black was removed being the background) with the maximum number of pixels, and the maximum number of pixels. The first parameter gives information on how much the image is dark or light, the second one gives an index of uniformity of the gray tone.

Multivariate statistical analysis was then carried out on the whole pixel distribution (independent variables) with the aim to improve predictability of the firmness and the soluble solids content (dependent variables) based on the image parameters. Independent variables were arranged in a 116 (samples) × 255 (variables) matrix and two vector columns were created for the dependent variables MTf and SSC.

For Partial Least Squares (PLS) bilinear approach, R^2 and RMSE (Root Mean Square Error) were calculated for calibration and segmented cross validation (15% of samples, randomly selected). The validation residual variance plot was explored to select the optimal number of PLS components (PLScomp) (The Unscrambler ver.9.7, Camo, Oslo, Norway).

In the artificial neural network (ANN) modelling (multilayer perceptron), the dataset was randomly divided into training and testing. Testing samples were characterised by the 15% of the samples. The Levenberg-Marquardt algorithm was used to train the network. The Levenberg-Marquardt algorithm, developed to solve nonlinear least squares problems, combines two minimization methods: the gradient descent method and the Gauss-Newton method [22]. The network was characterised by 255 input nodes, 1 hidden layer (number of hidden neurons = 5) and 1 output node. A sigmoid activation function $f(x)=1/[1+\exp(-x)]$, where x is the input variable, was considered in order to reduce the possibility of overtraining. The network design and the number of processing elements in the hidden layer was empirically obtained by monitoring and analysing the network error progress (MatlabR2016b, Statistics and Machine Learning Toolbox).

3.4.3. Results

3.4.3.1. Descriptive characteristics

The spectral emission of the used Xenon lamp is given in Fig. 3.4.2. From the figure it can be seen a strong emission in the 800–900 nm region. The main characteristics of

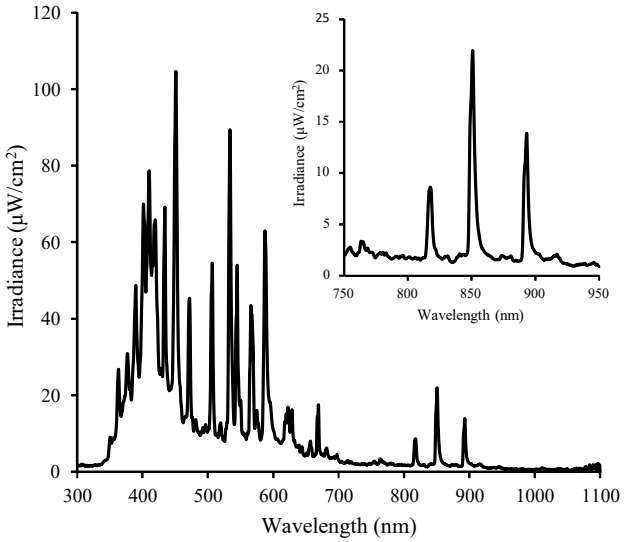

Fig. 3.4.2 – Spectral emission of the used xenon lamp. In the inset a magnification of the spectrum in the NIR region.

the used fruits were summarised in Table 3.4.1. An example of two images of kiwifruits with different MTf, captured by the infrared-sensitive camera and processed in a 8-bit grayscale was reported in Fig. 3.4.3.

In Fig. 3.4.4, the count of the image pixels for each gray tone (from 1 to 255) and for three kiwifruits with different Magness-Taylor flesh firmness (MTf) is given as an example.

Table 3.4.1 – Main characteristics of the kiwifruits used for the experiment.

Mass (g)	Dmin (mm)	Dmax (mm)	L (mm)	MTf (N)	SSC (°Bx)
112(10)	49(2)	55(2)	72(3)	26(26)	11(2)

Legend: Dmin, minimum equatorial diameter; Dmax, maximum equatorial diameter; L, maximum length, MTf, Magness-Taylor flesh firmness; SSC, soluble solids content (standard deviation is in brackets).

3.4.3.2. Data analysis

3.4.3.2.1. Univariate analysis

The dependence of the prevalent gray tone of the image on MTf appears exponential (R^2=0.717), such as reported in Fig. 3.4.5. In any case, this trend shows an absence of linearity between the flesh firmness and the quantity of light passing through it. In particular, only when the fruit is overripe, abundant light emerges from the flesh, while even when the hardness is modest, the radiation absorption is high.

On the contrary, MTf is related with the number of maximum pixels in a linear fashion (R^2=0.687), such as depicted in Fig. 3.4.6. In other words, MTf seems to increase when the uniformity of the image tone increases.

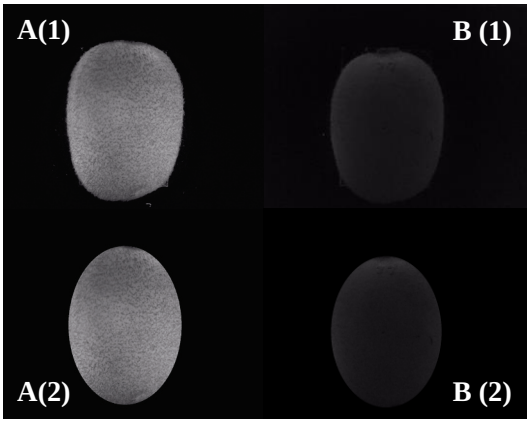

Fig. 3.4.3 – Eight bits gray scale image of an overripe and a kiwifruit with very high Magness-Taylor flesh firmness, MTf. A: MTf=2 N; B: MTf=85 N; (1): whole image; (2): inscribed in an oval area image.

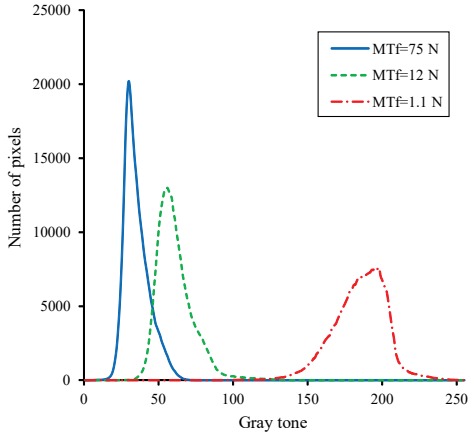

Fig. 3.4.4 – Count of the image pixels for each gray tone (from 1 to 255) and for three exemplifying kiwifruits with different Magness-Taylor flesh firmness, MTf.

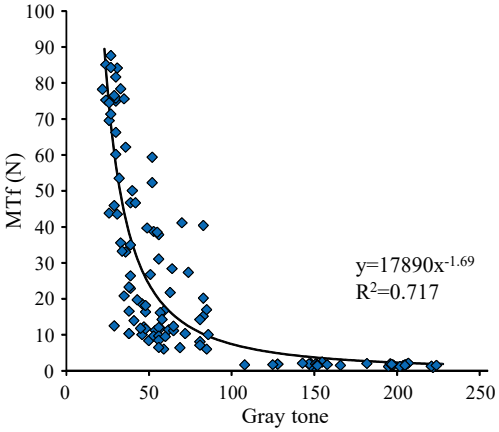

Fig. 3.4.5 – Magness-Taylor flesh firmness, MTf, vs gray tone (from 1 to 255) of the maximum number of pixels.

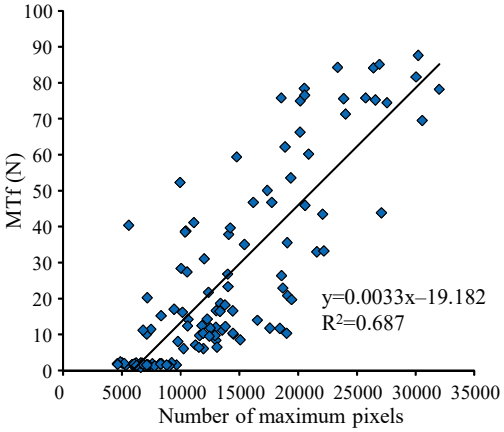

Fig. 3.4.6 – Magness-Taylor flesh firmness, MTf, vs the maximum number of pixels of the same gray tone.

The SSC appears related with the prevalent gray tone (Fig. 3.4.7) and with the maximum number of pixels of the same gray tone (Fig. 3.4.8) according to a logarithmic trend (R^2=0.496 and 0.470, respectively). The correlation (Fig. 3.4.9) between MTf and SSC is negative, with a possible linear trend (R^2=0.649). Generally, the correlations between image parameters and MTf result higher than that for SSC. All constant and coefficients in the functions are significant at p-level>0.05.

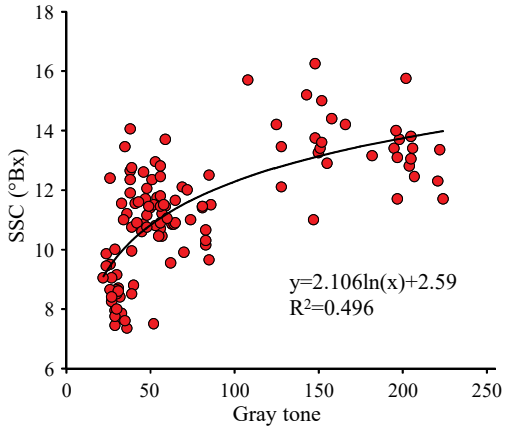

Fig. 3.4.7 – Soluble solids content, SSC (°Bx: degrees Brix), *vs* gray tone (from 1 to 255) of the maximum number of pixels.

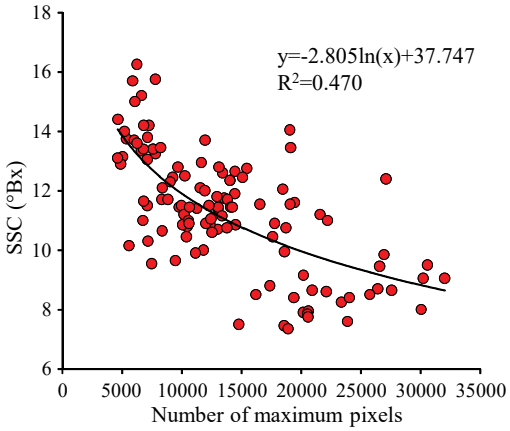

Fig. 3.4.8 – Soluble solids content, SSC (°Bx: degrees Brix), *vs* the maximum number of pixels of the same gray tone.

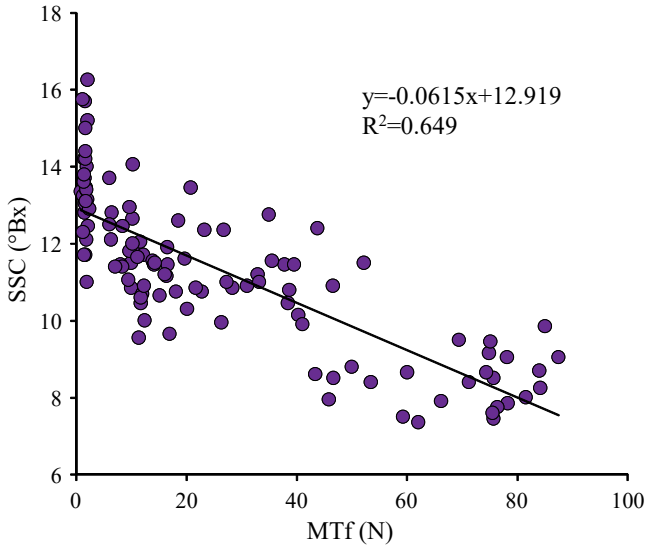

Fig. 3.4.9 – Soluble solids content, SSC (°Bx: degrees Brix), *vs* Magness-Taylor flesh firmness, MTf.

3.4.3.2.2. Multivariate analysis

Main results of the PLS regression analysis are summarised in Table 3.4.2. As can be observed, best results were obtained for the prediction of MTf. In validation, a value of 0.777 was obtained for the coefficient of determination R^2 with a root mean square

Table 3.4.2 – PLS regression main performances.

Qualitative parameters	Calibration			Segmented cross validation		
	PLScomp	R^2	RMSE	PLScomp	R^2	RMSE
MTf (N)	2	0.794	1.2	2	0.777	1.3
SSC (°Bx)	2	0.596	1.3	2	0.550	1.4

Legend: PLScomp, number of PLS components; RMSE, root mean square error.

error (RMSE) of 13 N. As expected from univariate data analysis results, lower accuracies emerged for the model set up for the prediction of the SSC.

Predicted versus observed values for the PLS models built for MTf and SSC are respectively shown in Fig. 3.4.10 and Fig. 3.4.11.

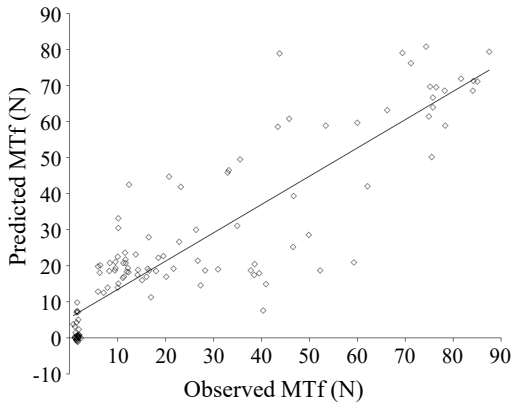

Fig. 3.4.10 – Predicted versus observed values of the Magness-Taylor flesh firmness, MTf (N) (segmented cross validation, R^2=0.777, RMSE=13 N).

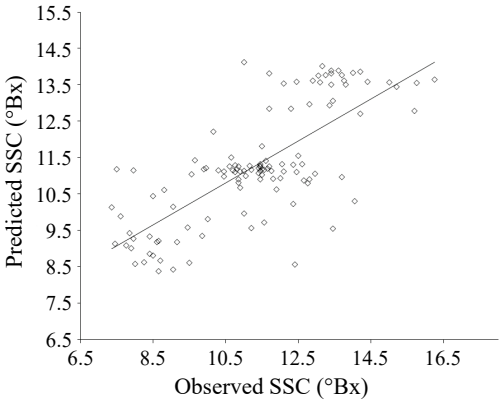

Fig. 3.4.11 – Predicted versus observed values of the soluble solids content, SSC (°Bx), (segmented cross validation, R^2=0.550, RMSE=1.4 °Bx).

X-Loadings describing the contribution to the variance of the individual independent variables (pixel distribution) are in Fig. 3.4.12 and Fig. 3.4.13 respectively for the MTf and SSC. As can be observed, for both qualitative parameters and PLS components, the highest loading values were extracted in the first 100 tones of the gray. In this tone range, the variability in terms of pixel distribution between samples characterised by different maturity indices (MTf and SSC) is the highest, as can be appreciated in the examples in Fig. 3.4.4. Also for ANN models, best performances were obtained for MTf (R^2=0.725, RMSE=14.6 N) respect to SSC (R^2=0.448, RMSE=1.6 °Bx) (test validation). In general, no great differences emerged between PLS and ANN modelling results (Table 3.4.3).

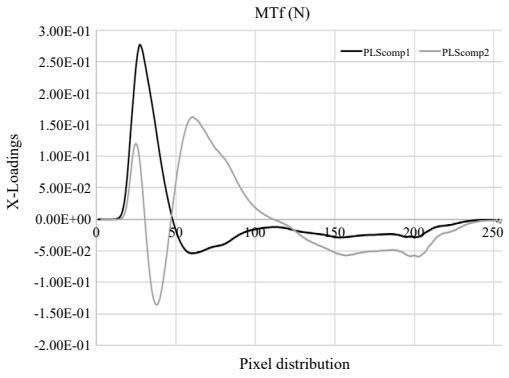

Fig. 3.4.12 – X-Loadings *vs* the pixel distribution for the Magness-Taylor flesh firmness, MTf, PLS model.

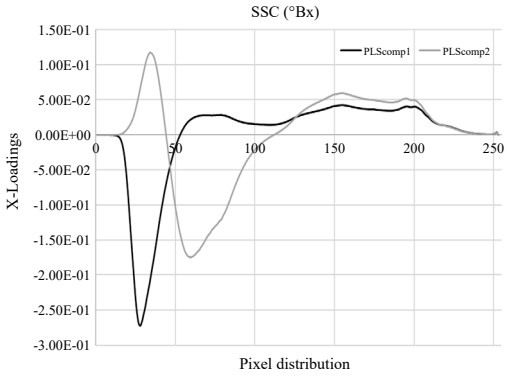

Fig. 3.4.13 – X-Loadings *vs* the pixel distribution for the soluble solids content, SSC, PLS model.

Table 3.4.3 – Artificial neural network main performances.

Parameter	R^2 training	R^2 validation	R^2 test	RMSE test
MTf (N)	0.849	0.733	0.725	14.6
SSC (°Bx)	0.696	0.653	0.448	1.6

Legend: RMSE, root mean square error.

3.4.4. Conclusions

The firmness of the kiwi flesh resulted related to the NIR radiation that emerges from the fruit backlighted by means of a xenon lamp. Basically, the softer the fruit, the more light passes through it. Image data based on a 8-bit gray scale analysed by univariate regressions revealed that there is not a linear, but exponential correlation (R^2=0.717) between gray tone peak and flesh firmness: the radiation plentifully passes through the fruit only when it becomes very soft (penetrometric force < 10 N). On the contrary, the degree of uniformity of the gray tone (amount of pixels of the same tone) was linearly correlated with the firmness (R^2=0.687). Multivariate analysis improved a little the performances of the determination models. Coefficient of determination for PLS regression, in validation, was 0.777 with RMSE value of 13 N. Artificial neural network produced substantially the same or a slight worse average result (R^2=0.725, RMSE=14.6 N). Soluble solids content resulted correlated with flesh firmness, but its correlation with optical parameters is worse than that for flesh firmness confirming that the device is more sensitive for variation in the flesh structure and not for soluble sugar content. Although the current technique has not exceptional performances, it could be improved by using lamps with different spectral emission and power, and predictive models with different algorithms. Installing the lamp under the fruit container in a mechanized sorting line should not be a difficult problem.

3.4.5. References

[1] A.R. Ferguson, New Temperate Fruits: Actinidia chinensis and Actinidia deliciosa, in: J. Janich (Ed.), Perspectives on New Crops and New Uses, ASHS Press, Alexandria, VA, 1999: pp. 342–347. https://www.hort.purdue.edu/newcrop/proceedings1999/pdf/v4-342.pdf.

[2] FAOSTAT Database, Food and Agriculture Organization of the United Nations, FAO Rome, Italy. (2017). http://www.fao.org/faostat/en/#data/QC (accessed March 15, 2019).

[3] H. Li, P. Pidakala, D. Billing, J. Burdon, Kiwifruit firmness: Measurement by penetrometer and non-destructive devices, Postharvest Biology and Technology. 120 (2016) 127–137. https://doi.org/10.1016/j.postharvbio.2016.06.007.

[4] M.M. Blanke, Reducing ethylene levels along the food supply chain: a key to reducing food waste?, Journal of the Science of Food and Agriculture. 94 (2014) 2357–2361. https://doi.org/10.1002/jsfa.6660.

[5] S. Janssen, K. Schmitt, M. Blanke, M.L. Bauersfeld, J. Wöllenstein, W. Lang, Ethylene detection in fruit supply chains, Philosophical Transactions of the Royal Society A: Mathematical, Physical and Engineering Sciences. 372 (2014). https://doi.org/10.1098/rsta.2013.0311.

[6] G. Costa, S. Vidoni, L. Rocchi, A. Cellini, G. Buriani, I. Donati, F. Spinelli, Innovative non-destructive device for fruit quality assessment and early disease diagnosis, Acta Horticulturae. 1096 (2015) 69–78. https://doi.org/10.17660/ActaHortic.2015.1096.4.

[7] R. Ben-Arie, J. Gross, L. Sonego, Changes in ripening-parameters and pigments of the chinese gooseberry (kiwi) during ripening and storage, Scientia Horticulturae. 18 (1982) 65–70. https://doi.org/10.1016/0304-4238(82)90104-2.

[8] S. Tan, L. Zhang, J. Yang, Sensing Fruit Ripeness Using Wireless Signals, in: 2018 27th International Conference on Computer Communication and Networks (ICCCN), IEEE, 2018: pp. 1–9. https://doi.org/10.1109/ICCCN.2018.8487344.

[9] L. Ragni, A. Berardinelli, A. Guarnieri, Impact device for measuring the flesh firmness of kiwifruits, Journal of Food Engineering. 96 (2010) 591–597. https://doi.org/10.1016/j.jfoodeng.2009.09.006.

[10] M.M. Blanke, Non-invasive Assessment of Firmness and NIR Sugar (TSS) Measurement in Apple, Pear and Kiwi Fruit, Erwerbs-Obstbau. 55 (2013) 19–24. https://doi.org/10.1007/s10341-013-0181-3.

[11] L. Ragni, C. Cevoli, A. Berardinelli, F.A. Silaghi, Non-destructive internal quality assessment of “Hayward” kiwifruit by waveguide spectroscopy, Journal of Food Engineering. 109 (2012) 32–37. https://doi.org/10.1016/j.jfoodeng.2011.10.002.

[12] C. Valero, M. Ruiz-Altisent, R. Cubeddu, A. Pifferi, P. Taroni, A. Torricelli, G. Valentini, D.S. Johnson, C.J. Dover, Detection of internal quality in kiwi with time-domain diffuse reflectance spectroscopy, Applied Engineering in Agriculture. 20 (2004) 223–230. https://oa.upm.es/6235/1/Valero_09.pdf.

[13] X.F. Hu, M. Lin, J.H. Fu, L. Jiao, H.J. Liu, Nondestructive hardness assessment of kiwi-fruit using near-infrared spectroscopy, in: 2016 Sixth International Conference on Instrumentation & Measurement, Computer, Communication and Control (IMCCC), IEEE, 2016: pp. 69–72. https://doi.org/10.1109/IMCCC.2016.109.

[14] J. Li, L. Xue, M. Liu, Z. Li, Y. Yang, Application of laser to nondestructive detection of fruit quality, in: Proc. SPIE 7276, Photonics and Optoelectronics Meetings (POEM) 2008: Laser Technology and Applications, 72760R (18 February 2009), 2009: pp. 1–6. https://doi.org/10.1117/12.823295.

[15] L. Baranyai, M. Zude, Analysis of laser light propagation in kiwifruit using backscattering imaging and Monte Carlo simulation, Computers and Electronics in Agriculture. 69 (2009) 33–39. https://doi.org/10.1016/j.compag.2009.06.011.

[16] A. Taglienti, R. Massantini, R. Botondi, F. Mencarelli, M. Valentini, Postharvest structural changes of Hayward kiwifruit by means of magnetic resonance imaging spectroscopy, Food Chemistry. 114 (2009) 1583–1589. https://doi.org/10.1016/j.foodchem.2008.11.066.

[17] C.J. Clark, L.N. Drummond, J.S. Macfall, Quantitative NMR imaging of kiwifruit (Actinidia deliciosa) during growth and ripening, Journal of the Science of Food and Agriculture. 78 (1998) 349–358. https://doi.org/10.1002/(SICI)1097-0010(199811)78:3<349::AID-JSFA125>3.0.CO;2-X.

[18] X.G. Hu, X.L. Li, S.H. Park, Y.H. Kim, S.I. Yang, Nondestructive monitoring of kiwi ripening process using colorimetric ethylene sensor, Bulletin of the Korean Chemical Society. 37 (2016) 759–762. https://doi.org/10.1002/bkcs.10745.

[19] W. Liu, G. Hui, Kiwi fruit (Actinidia chinensis) quality determination based on surface acoustic wave resonator combined with electronic nose, Bioengineered Bugs. 6 (2015) 53–61. https://doi.org/10.1080/21655979.2014.996430.

[20] T. Yen, D. Yao, Freshness Detection of Kiwifruit by Gas Sensing Array based on Surface Acoustic Wave Technique, in: 2018 IEEE 13th Annual International Conference on Nano/Micro Engineered and Molecular Systems (NEMS), IEEE, 2018: pp. 98–101. https://doi.org/10.1109/NEMS.2018.8556907.

[21] M.D. O'Toole, L.A. Marsh, J.L. Davidson, Y.M. Tan, D.W. Armitage, A.J. Peyton, Non-contact multi-frequency magnetic induction spectroscopy system for industrial-scale bio-impedance measurement, Measurement Science and Technology. 26 (2015) 035102 (17pp). https://doi.org/10.1088/0957-0233/26/3/035102.

[22] D.W. Marquardt, An Algorithm for Least-Squares Estimation of Nonlinear Parameters, Journal of the Society for Industrial and Applied Mathematics. 11 (1963) 431–441. https://doi.org/10.1137/0111030.

3.5. In-field hyperspectral imaging: An overview on the ground-based applications in agriculture

Scientific publication – Paper V

Benelli, A., Cevoli, C., & Fabbri, A. (2020). In-field hyperspectral imaging: An overview on the ground-based applications in agriculture. *Journal of Agricultural Engineering, LI:*1030, 129–139. https://doi.org/10.4081/jae.2020.1030

Alessandro Benelli[a], Chiara Cevoli[a,b*], Angelo Fabbri[a,b]

[a]*Department of Agricultural and Food Sciences, Alma Mater Studiorum, University of Bologna, P.zza Goidanich 60, 47521, Cesena, FC, Italy*

[b]*Interdepartmental Centre for Agri-Food Industrial Research, Alma Mater Studiorum, University of Bologna, Via Quinto Bucci 336, Cesena, FC, Italy*

[*]*corresponding author: chiara.cevoli3@unibo.it*

Abstract

The measurement of vegetation indexes that characterise the plants growth, assessing the fruit ripeness or detecting the presence of defects and diseases, is a key factor to gain high quality of fruit or vegetables. Such evaluation can be carried out using both destructive and non-destructive techniques. Among non-destructive techniques, hyperspectral imaging (HSI), combining image analysis and visible/near-infrared spectroscopy, looks particularly useful. Many studies have been published concerning the use of hyperspectral cameras in the agronomic and food field, especially in controlled laboratory conditions. Conversely, few studies described the application of HSI technology directly in field, especially involving ground-based systems. Results suggest that this technique could be particularly useful, even if the role of environmental variables has to be considered (*e.g.,* intensity and incidence of solar radiation, wind or the soil in the background). In this paper, recent in-field HSI applications based on ground systems are reviewed.

Keywords: hyperspectral, fruits, vegetables, in-field application, prediction, classification.

3.5.1. Introduction

The hyperspectral imaging (HSI) concept originated from imaging spectrometry (Liu et al., 2015). In the mid-1980s imaging spectrometry, a new Earth remote sensing technique, was developed at the Jet Propulsion Laboratory (JPL) of the California Institute of Technology in Pasadena, affiliated with the National Aeronautics and Space Administration (NASA). Airborne and spaceborne sensors allowed the identification of surface materials directly and remotely; images of the observed surface were obtained, simultaneously with reflectance values coming from up to 200 contiguous spectral bands in the reflectance spectrum (Goetz et al., 1985).

During the last few decades, numerous imaging and spectroscopic techniques have been developed and implemented by the agricultural and food industries for the evaluation and classification of products based on their intrinsic characteristics and properties (ElMasry & Sun, 2010). In recent years, the integration of imaging and spectroscopy through the development of HSI technology has made it possible to combine their benefits, obtaining results that are difficult to achieve with traditional imaging and spectroscopic technologies (Lu & Park, 2015). As evidence of this, there is a growing interest in research in this field as shown in Fig. 3.5.1 where the number of papers published in Scopus database (January 2020) in the range of years 2000-2018 on hyperspectral imaging in agricultural and biological sciences and engineering

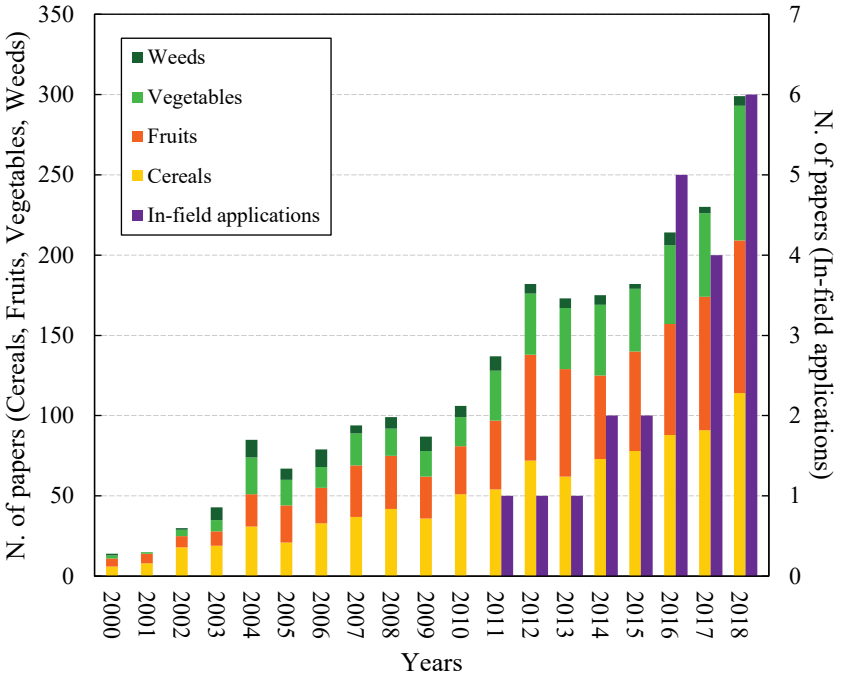

Fig. 3.5.1 – Number of documents published in Scopus database in the range of years 2000–2018 on hyperspectral imaging in agricultural and biological sciences and engineering subject areas.

subject areas are reported. The categories '*Cereals*', '*Fruits*' and '*Vegetables*' have been created from the FAO (Food and Agriculture Organisation of the United Nations) Commodity lists (©FAO 1994); in particular, the '*Vegetables*' category, was obtained by aggregating the FAO categories vegetables, roots and tubers, pulses, and oil-bearing crops.

3.5.1.1. Operating principles of a hyperspectral camera

A HSI lab-scale system (Fig. 3.5.2) typically consists of a light source, a CCD or CMOS camera with a spectrograph (HSI camera), a translation stage composed by a conveyor belt on which the sample flows, and a computer (ElMasry et al., 2012; Liu et al., 2015).

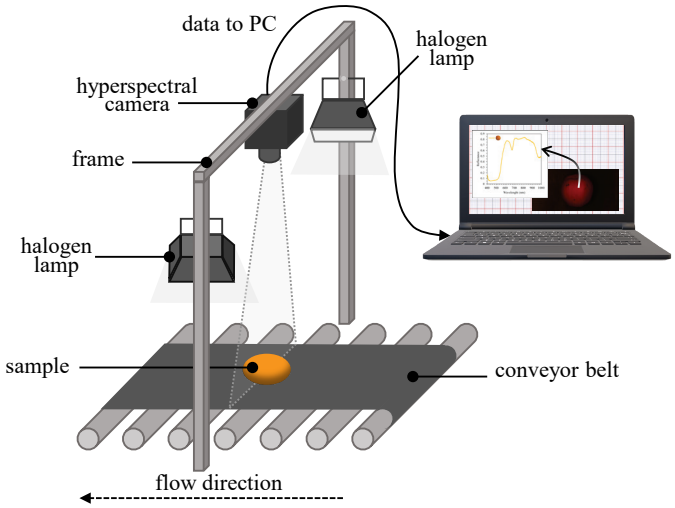

Fig. 3.5.2 – Components of a typical hyperspectral imaging system of the push-broom type.

The operating principle of a HSI camera is comparable to that of an RGB camera: both measure and record the amount of light reflected by the framed object, which reaches the sensor. Both cameras can only partially process the electromagnetic spectrum: the RGB camera sensor measures only three bands of the visible radiation (corresponding to the blue, green, and red light), while the HSI camera sensor can measure a few hundred bands within the characteristic wavelength range of the sensor. The amplitude of a few nanometers of the spectral bands determines a high spectral resolution of the HSI sensor (Thomas et al., 2018). To disperse the light into selected wavelengths, optical and electro optical wavelength dispersion devices are used (Liu et al., 2015).

3.5.1.2. Sensor systems

There are three types of sensor systems (Fig. 3.5.3): a) '*whisk-broom*' linear array with a rotating mirror: b) '*push-broom*' linear array; c) area array. The sensor systems with linear arrays include diodes or charge coupled devices that measure the radiance resulting from the object framed. Linear array sensors are often named *'push-broom*' because their disposition resembles the arrangement of a single line of bristles in a broom (Jensen, 2014). Since the HSI camera captures only one line of the object framed, a translation stage is used to slide the sample below the lens. In this way a whole scan of the surface of the object can be obtained, then the computer creates and displays a complete hyperspectral image (Liu et al., 2015). Respect to whisk-broom detectors, push-broom detectors provide a more accurate measurement of the radiant flux reflected by the sample because: i) there are no moving mirrors; and ii) push-broom linear array sensors are able to stay longer on a specific part of the sample (Jensen, 2014). With the area array detector system, hyperspectral images are acquired entirely, one at a time for each spectral band. This system does not require sample or HSI camera movement. A filter, wheel or tunable, is necessary to select different wavelengths during the scanning process (ElMasry et al., 2012). Area array sensor system is more practical in multispectral imaging techniques, where the number of wavelengths selected is limited (Garini et al., 2006).

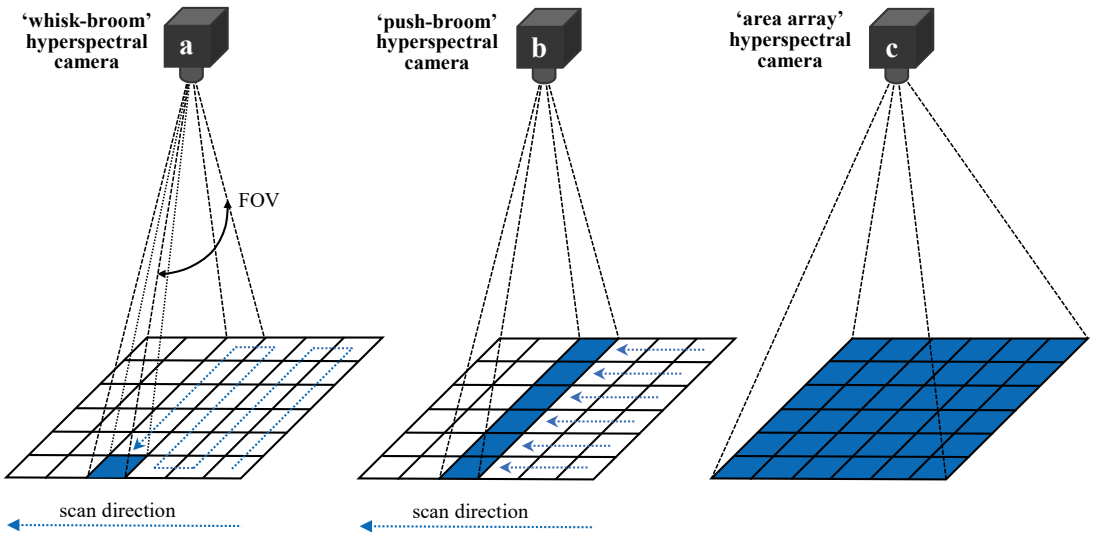

Fig. 3.5.3 – Three types of scanning systems used for multispectral and hyperspectral data collection: a) imaging with a scanning mirror and linear arrays, often referred to as whisk-broom technology; b) hyperspectral imaging with linear arrays, often referred to as push-broom technology; c) digital frame camera based on area arrays. FOV, field of view of the rotating mirror.

3.5.1.3. The hyperspectral image

In a hyperspectral image, each pixel is characterised by the information on reflectance, absorbance, or transmittance from each spectral band selected. The so-called spectral signature (or spectral profile) can be obtained by summing this information, but it can also be measured through a non-imaging hyperspectral sensor like a spectrometer, loosing spatial information (Thomas et al., 2018). HSI, combining spectroscopy and imaging, measures at the same time the spectral signatures and the spatial information from a sample. The HSI data output is a stack of narrow band sub images organised along the reflectance spectrum axis, thus generating a 3-D hypercube (Fig. 3.5.4). The 3-D cube data (named '*voxel*') is characterised by two spatial (x, y) and one spectral dimension (λ) (Mishra et al., 2017).

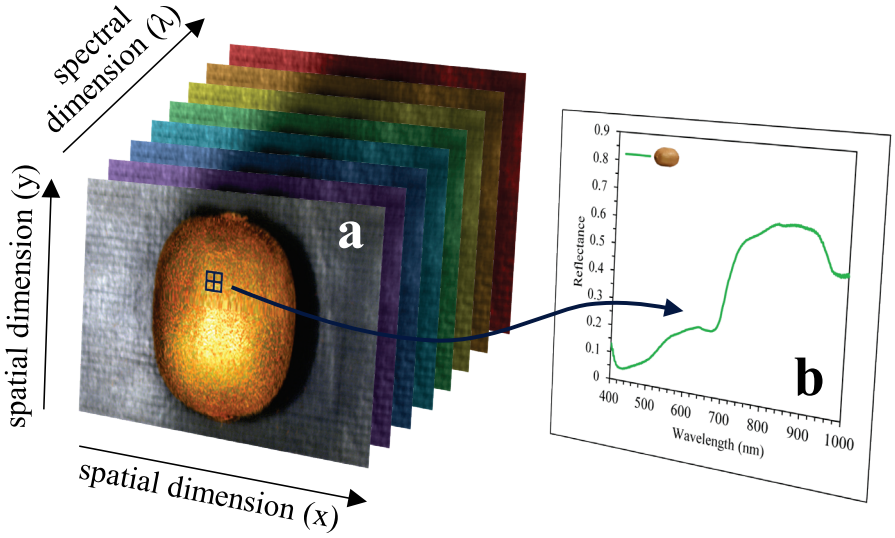

Fig. 3.5.4 – a) representation of a 3D hypercube, composed of a stack of sub-images of a kiwi in contiguous spectral bands; b) reflectance spectrum of one pixel represented in (a) by a blue square.

3.5.1.4. Hyperspectral image processing

A typical hyperspectral image processing consists in the following phases: i) calibration and image acquisition; ii) spectral/spatial processing and dimensionality reduction; iii) data elaboration and development of prediction or classification models. Several techniques have been developed to process both the spatial and spectral dimensions of a hyperspectral image. Dimensionality reduction means reduction in data size and extraction of spatial and/or spectral characteristics in a smaller dimensional space. Subsequently, the data can be classified to identify the pixels/spectra useful for the analysis. Regression techniques can also be applied to estimate a reference parameter; in particular, in recent years techniques of

chemometric and multivariate analysis have been applied to hyperspectral images (Yoon & Park, 2015).

3.5.1.4.1. Calibration and image acquisition

The calibration of the image acquired in reflectance, absorbance or transmittance mode allows to obtain a corrected image considering a black and a white reference image: the black image can be obtained by placing the cap on the lens of the camera, instead the white image is carried out of a high reflectance material placed inside the framing area (Ma et al., 2019).

3.5.1.4.2. Spectral/spatial processing and dimensionality reduction

Spectrum processing includes pre-processing and extraction of spectral characteristics. The most commonly used techniques are smoothing methods of random noise from raw data (*e.g.,* Savitzky-Golay, moving average, median filter), or spectral pre-processing algorithms to refine the spectral data as the derivatives (Norris-Williams and Savitzky-Golay), multiplicative scatter correction (MSC), standard normal variate (SNV), alignment technique (COW) (Rinnan et al., 2009).

Considering the multivariate models, to avoid problem of multicollinearity, it is useful to make a variable selection. This can improve model performance and model characteristics by identifying and removing useless, noisy, and redundant variables (Liu et al., 2014). There are three main variable selection methods: filter methods (information gain and correlation-based feature selection) wrapper methods (learning algorithms, such as beam search, simulated annealing, and genetic algorithms) and embedded methods (SVM and decision tree).

Regarding the wavelength selection the most common methods are successive projections algorithm (SPA), stepwise regression (SWR), PLSR and uninformative variable elimination (UVE). Some other algorithms for applications in HSI analysis have been developed recently and exhaustively described by Liu et al. (2014).

3.5.1.4.3. Classification and prediction methods

Classification methods include multivariate classification techniques, which comprises: i) unsupervised methods as principal component analysis (PCA), clustering (k-means, Jarvis-Patrick, hierarchical), and convolutional neural networks (CNN); ii) supervised methods as discriminant analysis (linear, quadratic or regularised DA), soft independent modelling class analogies (SIMCA), partial least square discriminant analysis (PLS-DA), support vector machines (SVMs), and the non-parametric k-nearest neighbour (kNN) (Ma et al., 2019). Prediction methods used to estimate the relation between spectral information and reference properties measured on the samples are divided into linear and non-linear regression. Linear regression includes multiple linear regression (MLR), principal component regression (PCR), and linear

partial least square regression (PLSR). The most commonly used non-linear regression are artificial neural networks (ANN), *e.g.,* multilayer perceptron (MLP) or generalised regression neural network (GRNN), SVM and nonlinear PLSR (Ma et al., 2019).

3.5.2. HSI application in the field

Recently, due to the rapid development of computer systems with high data processing capacities and the miniaturization of HSI systems, the opportunity of analysing in real time plants and foods, such as fruits and vegetables directly in the field at ground level, has become more interesting. Satellite based systems or airborne systems (manned or unmanned aerial vehicles, tethered balloons) characterised by low spatial resolution are mainly aimed at the study of the plants canopy and terrestrial vegetation. In addition, ground-based systems mounted on agricultural vehicles or fixed platforms have been introduced, due to their high spatial resolution, for the estimation of quality parameters of plants and foods.

In this work, both remotely and directly controlled ground based HSI systems have been considered, which have been used in the field for: i) phenotypic analysis of plants; ii) determination of fruit ripeness, chlorophyll, and nitrogen content of plants; iii) detection of fungal diseases, drought stress, weeds, maize stubble in conservative agriculture; and iv) monitoring of canopies under uncontrolled conditions. The search for the papers was carried out on the abstract and citation database '*Scopus*' on January 29th, 2019: the keywords '*hyperspectral*' and '*field*' were searched; the search was limited to the subject area '*agri*'. Hence, 1069 results were obtained: from the list of results, only the articles that met the purposes of this work were selected (Table 3.5.1).

3.5.2.1. High-throughput phenotyping

The study of different crop genetic varieties and growth related phenomic effects under different environmental conditions is essential to achieve higher productivity in terms of yield per hectare and sustainable use of natural resources (Underwood et al., 2017). High-throughput phenotyping (HTP) is crucial to improve yield as well as quality and it contributes to a better understanding of plant genomics. However, phenotyping techniques mainly rely on manual measurements and visual inspections. In addition, phenotyping techniques are not developed as well as genotyping techniques in terms of throughput, accuracy, and repeatability. This condition hinders the potential use of plant genotyping data for the development of genotype phenotype maps and for the characterisation of the interactions between genotype and environment (Jiang et al., 2018).

Table 3.5.1 – Works cited, in the order in which they are listed in the text, with a brief description of their strengths and weaknesses.

Arguments	References	Applications	Strengths	Weaknesses
3.5.2.1. High throughput phenotyping				
	Underwood et al., 2017	Grains, legumes	Adoption of an unmanned ground vehicle, useful in term of labor saving and accuracy. Moderately good results.	Limitation for the tallest plants (faba beans). Potential for crop damage.
	Jiang et al., 2018	Cotton	Multi-instrumental system. Moderately good results.	The implementation of a cover reduced the amount of incident sunlight, requiring the use of artificial lights.
	Gutiérrez et al., 2018	Grapevine	Real time, on-the-go HSI approach. Good prediction performance.	Nothing to report.
	Deery et al., 2014	Wheat	Multi-instrumental system.	Requires a high degree of expertise.
3.5.2.2. Fruit ripening				
	Wendel et al., 2018	Mango	Adoption of an unmanned ground vehicle. Dry matter prediction of 'on-the-tree' mangoes is possible and repeatable.	The geometry of the trees, the shadows of the fruits and the variation in the intensity and angle of the solar radiation affected the result.
3.5.2.3. Chlorophyll content				
	Wang et al., 2018	Rice canopy	The spectral purification procedure developed contributes to reduce the background impact. Moderately good results.	The method lacks automation.
	Wu et al., 2016	Wheat leaves and canopy	Good results from single wheat plant leaves.	Low precision of canopy spectral data, due to soil in the background.
	Jay et al., 2017	Sugar beet canopy	Good performances achieved with an optimized vegetation index.	Results affected by a great variability of leaf orientation and lighting conditions.
	Al Makdessi et al., 2017	Durum wheat canopy	Development of a light propagation model based on 3D models. Acceptable nitrogen content prediction.	Multiple scattering effects mainly affect the lower leaves, which cannot be discarded due to a significant loss of information.
	Malenovský et al., 2015	East Antarctic dominant mosses	Good chlorophyll a and b, and leaf density estimation.	The prediction of the turf water content was influenced by the selection of the near infrared spectral region, which does not include wavelengths with adequate water absorption.
3.5.2.4. Nitrogen content				
	Onoyama et al., 2015	Rice plant	Good results applying the growing degree-day parameter, related to air temperature, to predict nitrogen content.	The wind has made some of the captured images unusable.
	Onoyama et al., 2018	Brown rice	Good prediction performance adopting 4 regions of interest models.	Exception on good prediction performance for the dark area model. Strong wind affected the capture of two images.
	Vigneau et al., 2011	Wheat leaves	Complications introduced by variable solar lighting and plant architecture were considered. Good prediction performance of leaf nitrogen content.	Models are dataset dependent, probably due to low sample number and growing conditions, in particular with regard to the plant nitrogen supply.
3.5.2.5. Fungal diseases detection				
	Whetton et al., 2018	Wheat, barley	Performance was better in wheat than in barley.	Use of an external light source.
	Zhao et al., 2016	Winter wheat	Able to follow the vertical features of the infestation.	The method lacks automation.

Table 3.5.1 – Continued

Arguments	References	Applications	Strengths	Weaknesses
3.5.2.6. Drought stress detection				
	Römer et al., 2012	Barley, corn	Corn: clear detection of clusters, determined by two irrigation and nitrogen availability regimes.	Barley: the experiment was conducted inside a rain-out shelter.
3.5.2.7. Weeds detection and management				
	Pantazi et al., 2016	Corn	Use of an autonomous platform and information system. Excellent crop recognition performance, using one-class classifications constructed on neural networks.	One-class classifiers based on support vector machine and autoencoders have failed, in most cases, to yield acceptable results.
	Herrmann et al., 2013	Wheat	Detection of four categories, with a good accuracy: weeds (2), wheat and soil.	In most of the cases, shaded classes produced less user's and producer's accuracies than the respective sunlit class.
	Huang et al., 2016	Palmer amaranth, Italian ryegrass, soybeans	On-the-go HSI system. Excellent accuracy obtained on glyphosate resistant and sensitive weeds differentiation.	Wind interference and sensor overheating due to intense solar irradiation had affected the experiment.
	Reddy et al., 2014	Palmer amaranth	Excellent validation accuracy of the field model classification, able to differentiate between glyphosate resistant and sensitive palmer amaranth plants.	Nothing to report.
3.5.2.8. No tillage in conservative agriculture				
	Chen et al., 2017	Corn stubble	Good capacity to detect corn stubble, useful in corn-wheat rotation systems in case of no-tillage sowing.	The study is limited to the selection of optimal wavelengths by means of principal component analysis to optimize image segmentation.
3.5.2.9. Canopy monitoring under uncontrolled conditions				
	Rodriguez-Moreno et al., 2016	Wheat	The error in estimation of crop reflectance was compatible with a proper agronomic interpretation of the images using thresholds, linear functions or combination of both.	The main problem observed is not the accuracy of the measurements, but the precision.

In line with the aforementioned state, (Underwood et al., 2017) used a high-throughput phenotyping system, designed for row crops composed by a set of grains and legumes. The system described, named *Ladybird UGV*, was based on an unmanned ground vehicle (UGV) that allowed autonomous, high resolution, multi modal sensing and data processing. Hyperspectral data were acquired with a visible to near-infrared (VNIR) push-broom camera (Pika II, Resonon); hyperspectral images were of 648 spatial by 244 spectral pixels, with a spectral resolution of 2 nm in the range from 390.9 to 887.4 nm. Data were compared to those obtained by a handheld sensor named *Greenseeker*. Moderate linear relationships characterised by a R^2=0.83 and R^2=0.72, were reported for data acquired in August and September, respectively. *Ladybird UGV* was able to efficiently scan areas of coverage typically used in real world scientific phenotyping studies. This way of operating was faster than optimised traditional manual measurement, and it was able to generate highly repeatable and accurate data (Underwood et al., 2017).

The field-based high-throughput phenotyping (FB-HTP) system developed by Jiang *et al*. (2018), named *GPhenoVision*, consisted of a high-clearance tractor with imaging, environmental and GPS sensors; it was evaluated by field scan of 23 cotton genotypes, to quantify canopy growth and development. Imaging sensors consisted of a conventional RGB-D, a thermal and a hyperspectral camera (MRC-923-001, Middleton Spectral Vision, Middleton, WI, USA). HS camera has a spectral range of 400–1000 nm, an image resolution of 640 (spatial) × 236 (spectral), and a nominal spectral resolution of 2.7 nm. About imaging tests, to reduce the intensity of sunlight and wind effects a cover was adopted, but with this configuration the intensity of the signal recorded by the hyperspectral camera was low due to the reduced amount of incident light. Finally, regarding the hyperspectral camera, three calibration lamps were used to obtain a more accurate regression. In the present study, six phenotypic traits were extracted: plant height, width in-row (WIR), width across-row (WAR), projected leaf area (PLA), canopy volume (CV) and canopy expansion (Tc-Ta). The considered traits had a moderate correlation (r=0.54–0.74). These results suggested that a quantitative genetic analysis could be conducted, and yield prediction models could be developed (Jiang et al., 2018).

Phenotyping of grapevine varieties is important both for producers and for the wine industry (Gutiérrez et al., 2018). Gutiérrez et al. (2018) classified a high number of grapevine varieties under field condition and natural illumination using a hyperspectral camera system (Pika L VNIR hyperspectral imaging camera, Resonon, Inc., Bozeman, MA, USA) mounted on an all-terrain vehicle (ATV). The horizontal movement of the ATV regulated the scanning of the push-broom type line scan hyperspectral camera. Data were processed by using SVM and artificial neural networks (multilayer perceptrons, MLP) testing several spectra pre-processing methods. Recall (the ratio of the number of correctly classified samples to the total number of testing samples), F1 value [2 × (precision × recall) / (precision + recall)] and AUC (area under the receiver operating characteristic curve) were used as performance statistics. The prediction performance of SVM respect to individual varieties resulted in a range from 0.83 (recall) to 0.93 (AUC), while for MLP between 0.95 (recall and F1 score) and 0.99 (recall and F1 score), showing a low variability, in particular the AUC values (Gutiérrez et al., 2018).

To keep up with the development of genomic technologies, fast and accurate crop phenotyping methods are required, in order to meet expected growing demand for food and fibre in the future (Deery et al., 2014). In this perspective, Deery et al. (2014) described the development of a ground based proximal remote sensing buggy named '*Phenomobile*', implementing these sensors: three LiDAR, four RGB stereo cameras, a thermal infra-red camera, three infra-red thermometers and a hyperspectral subsystem. The latter is composed by a full range spectroradiometer (Fieldspec 3, ASD

Inc., Boulder, CO, USA) and a Vis-NIR hyperspectral line scanner camera (Micro-Hyperspec, Headwall Photonics Inc., Fitchburg, MA, USA). Sensors were mounted on a height adjustable bar (max 3 m from the ground). The frame of the *Phenomobile* was designed to traverse a mature wheat crop (1.2 m ground clearance and 1.8 m width) without coming into contact with the canopy, at a typical operating speed of 1 ms^{-1}. Moreover, *Phenomobile* presented a Real Time Kinematic GPS characterised by about 2 cm resolution, and a removable light bank (Deery et al., 2014).

3.5.2.2. Fruit ripening

Fruit should ripen on the tree, to allow accumulation of sugars and starch getting the best harvesting conditions. Fruits would have to reach on-tree physiological maturity, finding a balance between on-tree ripening and characteristics required for transport and storage. Hyperspectral imaging systems implementation directly in-field can help farmers to optimise harvest time, evaluating the grade of ripening of fruits (Wendel et al., 2018). In the study of Wendel et al. (2018), a hyperspectral camera (Resonon Pika II visible to near infrared (VNIR) line scanning hyperspectral camera, with a spectral range of 411.3–867.0 nm), a LiDAR sensor and a navigation system mounted on a ground vehicle contributed to carry out the measure of dry matter (DM) of mango to evaluate maturity. DM resulted from measures performed by a hand-held NIR spectrometer of harvested and on-tree fruit. These data were elaborated by using PLSR and CNN. Considering the cross-validation data set, R^2=0.64 and RMSE=1.08%w/w was achieved by CNN in fruit on tree, while R^2=0.58 and RMSE=1.17%w/w was achieved by PLS. Moreover, PLSDA and a CNN were compared to discriminate non mango pixels from mango pixels, obtaining good classification performance (mean F1 score > 0.97). The described system permitted to predict the maturity of fruits at a distance from trees but presented difficulties due to the geometry of the trees, the shadows of the fruits and the variation of the intensity and angle of solar radiation (Wendel et al., 2018).

3.5.2.3. Chlorophyll content

Determining chlorophyll quantitative variation during plant growth can be useful to monitor the physiological state of the plant, to better understand the growing status and consequently to estimate the yield of the plant (Jay et al., 2017).

Wang et al. (2018) captured rice canopy images with an imaging spectrometer (Cubert S185 Imaging Spectrometer, with a 4 nm of spectral resolution and a spectral range of 450-950 nm). Rice leaf hyperspectral images were obtained, in order to retrieve chlorophyll content from refined leaf spectra resulting from 58 rice canopies and to estimate the yield of paddy rice. Vegetation indices extracted from those hyperspectral

data were correlated with crop chlorophyll density measured with a SPAD meter (soil plant analysis development chlorophyll meter), with the aim to estimate leaf pigment content. Three vegetation indices with the highest correlation were selected and used: photochemical reflectance index (PRI), structural independent pigment index (SIPI) and green normalised difference vegetation index (GNDVI). A PLSR was used, obtaining in cross validation R^2=0.703 before purification, and R^2=0.753 after purification. A commonly used field portable spectroradiometer can only obtain point spectral information. However, the device is not able to obtain spectral and image information at the same time. Usually, canopy spectral data resulting from a spectroradiometer are the average of spectra collected in a specific area and are affected by the weaker part of the plant, which is located under the foliage, and by the environment (Wang et al., 2018).

Wu et al. (2016) analysed canopy and single wheat plant leaves at seedling stage using a spectroradiometer and a planar array visible near infrared hyperspectral camera (VNIR hyperspectral MS4100 high resolution 3 CCD camera, Redlake Inc.) to establish prediction models to monitor plant growth. Data obtained by the two instruments were correlated to plant growth measured factors (chlorophyll SPAD value, nitrogen and water content, dry matter). The hyperspectral camera adopted is more portable, with a higher acquisition rate and without the necessity to move the ground support mounted on a rail, respect to a push-broom hyperspectral camera. Due to the soil in the background, both the spectral data of canopy obtained with the two instruments were characterised by low precision. Instead, spectral data from single wheat plant leaves obtained with the hyperspectral camera were more detailed, gaining a correlation coefficient r of 0.8836, 0.8520 (PLSR) for chlorophyll SPAD and nitrogen content, respectively (Wu et al., 2016).

Jay et al. (2017) studied methods based on reflectance observations for non-destructive leaf chlorophyll content (C_{ab}) estimation at field level in sugar beet canopies. It was adopted a push-broom hyperspectral camera (HySpex VNIR 1600, Norsk Elektro Optikk, Norway) in the 400–1000 nm range, with high spatial resolution (millimetre to centimetre) mounted on a ground-based platform. The push-broom camera was positioned at 1.1 m above the ground and vertically oriented. At this scale, soil reflectance and the shape of canopy structure interact with the scattering properties related to leaf, producing canopy reflectance. Effects of canopy structure and leaf architecture (leaf orientation and spatial distribution) should be carefully straightened out when relating remote sensing observations to foliar biochemistry. The best performances were achieved with an optimised vegetation index named '*modified normalised difference*', $mND[\lambda_1,\lambda_2]$, defined as $(R_{\lambda ref}-R_{\lambda 1})/(R_{\lambda ref}+R_{\lambda 2})$, using a blue reference spectral band λ_{ref}=440 nm (R_λ refers to the reflectance at the given wavelength). Data were computed considering the average reflectance spectra related

to the 50% brightest green pixels, with a spatial resolution equal to 3.5 cm. mND_{blue}[728,850] was correlated with C_{ab} using a linear regression model, obtaining R^2=0.83 and RMSEP=2.45 μg cm^{-2} (Jay et al., 2017).

Leaf radiance variation is strongly induced by the great variability of leaf orientation and lighting conditions (Jay et al., 2017). At this regard, Al Makdessi et al. (2017) implemented the *'Caribu*' light propagation model on 3D models of durum wheat canopy, trying to obtain a picture of the spectra variability induced by the leafy architecture. Spectra were acquired in various phases on leaves completely expanded using a field spectrometer [FieldSpec, Analytical Spectral Devices, Inc. (ASD), Boulder, Colorado, USA] with a leaf clip. A PCA was performed to analyse the distribution of resulting simulated spectra in the spectral feature space. Finally, the performance of PLSR in predicting leaf nitrogen content (LNC) was evaluated. At the plant level, considering only the leaves on the top of the plant, it revealed an acceptable nitrogen content prediction, with an error about 0.5% of dry matter (Al Makdessi et al., 2017).

Near distance imaging spectroscopy was used by Malenovský et al. (2015) to evaluate spatial distribution of three East Antarctic dominant mosses (*Bryum pseudotriquetrum, Ceratodon purpureus* and *Schistidium antarctici*), due to the reduction of liquid water availability caused by latest environmental changes. Three quantitative stress indicators were used: turf chlorophyll a and b (C_{ab}), water content (TWC) and leaf density (LD). Reflectance was measured in the laboratory and outdoors in both poor and abundant water conditions. Field measurements were performed by an imaging push-broom type spectroradiometer (Headwall Photonics Micro-Hyperspec VNIR scanner, Headwall Inc., Fitchburg, MA, USA) mounted to a geodetic tripod on a rotation and tilt platform. In the spectral range of 496–898 nm, ten bands were selected, three in the visible (496–710 nm) and seven in the near infrared (710–848 nm). The best results were obtained estimating the reflectance continuum removal (CR) transformation of C_{ab} applying SVR on reference and remotely sensed spectra trained with all the three species of mosses together and considering the wavelengths between 648–719 nm, specific for chlorophyll absorption [RMSE=238.3 nmol g^{-1} DW (dry weight) and R^2=0.54]. The best LD estimation was achieved on *S. antarctici*, adopting SVR trained with the reflectance between 708 and 782 nm (RMSE=1.8 leaves mm^{-1}, R^2=0.55) (Malenovský et al., 2015).

3.5.2.4. Nitrogen content

Nitrogen nutrition index (NNI) is an expensive, laborious, and destructive method to assess plant nitrogen status during plant cycle. Since nitrogen is an essential nutrient and the main limiting factor of plant growth, many new non-destructive techniques

have been proposed to replace NNI, such as hyperspectral imaging (Vigneau et al., 2011).

Onoyama et al. (2015) developed a ground-based hyperspectral imaging system to estimate rice plants nitrogen content at the panicle initiation stage. In rice cultivation, nitrogen is applied in the form of topdressing in the early stages of panicle development, in order to increase the yield in terms of rice grains. The hyperspectral imaging system adopted consists of a prism-grating-prism (PGP) component and a monochrome camera (ImSpector QE V10E; Specim, Oulu, Finland), with a nominal spectral range between 400 and 1000 nm and a 5 nm nominal spectral resolution. A planetary gearbox rotational stage rotated the camera with the aid of a motor, for push-broom type line scan. Three PLSR models were tested, including both the reflectance and the growing degree days (GDD), to explain the differences in growing temperature conditions over a 3-year period (2008, 2009, and 2010): 1-year model, 2-year model and 2-year model based on GDD. GDD represents a meteorological condition frequently used to describe the timing of biological processes: it was calculated based on air temperature measurements. In order to determine the adaptability of the PLSR models to test data collected in different years, a mutual estimation of the values for the other years was calculated. In 1-year model, the RMSE and relative error (RE) values of the mutual estimation resulted much higher respect to the values of the validation of the same 1-year model (RMSE from 0.49 to 3.95 g/m^2 and RE from 8 to 85% in mutual estimation, RMSE from 0.48 to 0.65 g/m^2 and RE from 7 to 15% in validation), because of underestimation and overestimation. Similar results were obtained by applying the 2-year model, without significant differences in accuracy respect to the 1-year model (mutual estimation RMSE from 1.29 to 3.32 g/m^2 and RE from 21 to 43%). The introduction of GDD in the 2-year model (third model) resulted in a decrease in mutual estimation RMSE and RE values (RMSE from 0.55 to 0.95 g/m^2 and RE from 8.2 to 13%), proving its usefulness for predicting the nitrogen content. Ultimately, it has been shown that the combination of reflectance and temperature data could be used to construct a model that explains the changes in growth conditions of rice plants at the heading stage (Onoyama et al., 2015).

In brown rice production, it is important to consider grain quality as well as grain yield. A ground-based hyperspectral imaging system (ImSpector QE V10E, Specim, Oulu, Finland) with a nominal spectral range from 400 to 1000 nm, and a nominal spectral resolution of 5 nm, was used for the estimation of protein content before harvest. Protein content is related to rice taste quality; furthermore, it is also useful for establishing the application plan of the amount of basal and top-dressing fertiliser for the following year. The use of a spatial scanning hyperspectral camera allowed to obtain three-dimensional data. In spatial scanning, spatial spectral three-dimensional images can be collected line by line through rotational movement of the camera

powered by a motor. Instead, one dimensional data, deriving from a common spectroradiometer and represented by the reflectance of the analysed target, also include unwanted parts, such as soil background. The reflectance of five regions of interest (ROI-I: target area; ROI-II: dark area; ROI-III: canopy area; ROI-IV: leaf area; ROI-V: ear area) were related with protein content according to PLSR analysis. R^2 and RMSE prediction values were similar for each model, with R^2 values between 0.83 and 0.86, and RMSE between 0.27 and 0.30%, but with the exception of the dark area model, where R^2=0.76 and RMSE=0.35%. No significant differences in the magnitude of the estimation error between all models were observed. (Onoyama et al., 2018).

Vigneau et al. (2011) developed a system composed by a push-broom CCD camera (HySpex VNIR 1600-160, Norsk Elektro Optikk, Norway) installed on a tractor mounted motorised rail. The camera operated in the spectral range between 400 and 1000 nm, with a spectral resolution of 3.7 nm (160 wavelength bands). Close range hyperspectral images acquired were used to evaluate leaf nitrogen content in wheat. The study also considered in-field complications introduced by variable solar lighting and plant architecture, such as illumination level variation induced by leaf inclination and specular reflection. Reflectance pre-processing and correction process led to the same quality of results obtained in laboratory. A PLSR model considering nitrogen concentration and reflectance spectra of single leaves was developed; it was obtained by grouping two datasets, related to plants grown in pots in greenhouse or in field conditions. The model predicted leaf nitrogen content for the two growing conditions, with R^2=0.875 (test step), and standard error of prediction corrected of the bias (SEP_c)=0.496% DM (Vigneau et al., 2011).

In summary, hyperspectral images produced spatial nitrogen cartographies, and it was possible to monitor nitrogen dynamics at leaf level. Consequently, these data could be implemented in growing models or nitrogen remobilisation models (Vigneau et al., 2011).

3.5.2.5. Fungal diseases detection

Cereal production can be compromised by the presence of in-field fungal diseases. Due to their spatial variability, it is necessary to acquire high spatial resolution data to perform a detailed site-specific control of the diseases (Whetton et al., 2018).

Whetton et al. (2018) measured two fungal diseases with a mobile measurement system in four fields of wheat and barley: yellow rust (determined by *Puccinia striiformis*), one of the most detrimental foliar diseases of wheat in cool climates, and fusarium head blight (*Fusarium graminearum*), producing mycotoxins in the grain. Such online system consisted of a push-broom hyperspectral camera (HS spectral camera model from Gilden Photonics Ltd., UK) attached to a tractor, with an external

light source; the camera works in the spectral range of 400–1000 nm. The percentage of coverage of the diseases was assessed using two methods, in-field visual assessment (IVA) and photo interpretation assessment (PIA) on the basis of a 100-point grid superimposed on RGB images. The spectral data were analysed by PLSR with leave-one-out cross-validation. Measurements of yellow rust and fusarium head blight were similarly accurate, while performance was better in wheat than in barley. PIA analysis resulted more accurate than IVA for fusarium. Considering PIA analysis, residual prediction deviation (RPD) value was 2.27 and R^2 value was 0.82 for wheat, while RPD was 1.56 and R^2 was 0.61 for barley. On the contrary, IVA analysis was more accurate than PIA in the yellow rust. In barley RPD and R^2 values were 1.67 and 0.72, while in wheat they were 2.19 and 0.78 respectively (Whetton et al., 2018).

The yield and quality of winter wheat grains can also be seriously compromised by yellow rust. For this purpose, a hyperspectral imaging spectrometer (ImSpector V10E, Specim, Spectral Imaging Ltd., Finland) was used to accurately assess wheat yellow rust. The instrument works in the wavelength range between 400 and 1000 nm, with a spectral resolution of 2.8 nm. This ground-based imaging spectrometer system collected images in a push-broom manner. It consisted of a camera, a spectrograph, a mount zoom lens, and a mirror scanner: the system generates a hyperspectral data cube, which simultaneously collected spectral and imaging characteristics of pure yellow rust spores. Three flag leaves (F-1, F-2, and F-3: F = flag leaf) were randomly collected from the inoculated and normal wheat fields. Six region of interest (ROI) from the tip to the bottom of the three samples were analysed, finding a relation between the general trend of chlorophyll content (F-1>F-2>F-3) and the averaged hyperspectral reflectance measured; reflectance values gradually increased (F-1>F-2>F-3) in the visible region selected (520–720 nm) and decreased (F-1<F-2<F-3) in the NIR region (730–1000 nm) (Zhao et al., 2016). Compared to a conventional non-imaging spectrometer, a hyperspectral imaging system is particularly useful to detect the disease development along the leaf layers, following the vertical features of the infestation, in the appropriate growth phases considered. Furthermore, spectral and image data can be collected at once, regularly, and automatically. In this way, it may be decided to spray the fungicides, especially in the initial stages of the infestation (Zhao et al., 2016).

3.5.2.6. Drought stress detection

Hyperspectral imaging sensors were adopted to evaluate early water stress: i) on barley (SOC-700, Surface Optics Corp., San Diego, CA, USA) in controlled drought conditions inside a rainout shelter; and ii) on corn (PS V10E, Spectral Imaging Ltd, Oulu, Finland,) directly in the field, in order to check if the method is applicable both

in controlled conditions and in the field. The linear push-broom hyperspectral camera used on corn (PS V10E) is characterised by a spectral resolution of 2.8 nm in the range between 400 and 1000 nm (Römer et al., 2012).

A deterministic method to analyse data was introduced, named simplex volume maximisation (SiVM). The applicability of this matrix factorization technique was tested for the first time in plant sciences; it was also a new approach for unsupervised learning of relevant patterns. With regard to the corn experiment, plants were grown in an experimental field with two different irrigation regimes (rain-fed and full irrigation) and nitrogen availability. In addition, several vegetation indices (VIs), including the normalised difference vegetation index (NDVI) and the photochemical reflectance index (PRI), were tested. The results have shown that SiVM divided the four treatments into three well separated clusters. Regarding the VIs, the PRI detected a difference in nutrient treatment, but was not able to detect water, while the NDVI detected drought, but was not able to detect nutrient treatment. A combined assessment with PRI and NDVI was effective in successfully detecting all four clusters. In summary, SiVM has given considerable better results than the use of a combination of vegetation indices. In the corn plots, although the effect of the treatments on the foliar and canopy traits was reduced, SiVM managed to separate them (Römer et al., 2012).

3.5.2.7. Weeds detection and management

Ground-based remote sensing techniques (GBRST) provide interesting utilisations for precision agriculture (Huang et al., 2016). Crop production and yield are influenced by the presence of weeds, and the use of herbicides implies high costs and environmental impact. A method based on machine learning, developed by Pantazi et al. (2016), was used to discriminate between corn and weed species considering differences in spectral reflectance; Herrmann et al. (2013) developed a hyperspectral imaging (HSI) system to separate weeds from wheat.

Pantazi et al. (2016) obtained hyperspectral images from a HSI system (ImSpector V9, Specim, Spectral Imaging Ltd., Oulu, Finland) mounted on a robotic platform (autonomous platform and information system). This HSI system consisted of a prism-grating-prism (PGP) line spectrograph with a spectral resolution reduced to 19 nm and a spectral range between 435 and 834 nm, integrated with a monochromatic camera. Subsequently, four discrimination wavebands were selected using a stepwise variable selection. Four novelty detection classifiers have been implemented, based on one-class classification constructed on neural networks: SVM, autoencoder, mixtures of Gaussians (MOG) and self-organising maps (SOM). The best results were obtained using the SOM and MOG classifiers. The crop recognition performance was 100% for both MOG and SOM classifiers. For the MOG classifier, the correct recognition of the

different weed species ranged from 31% to 98%. For the SOM classifier, the correct recognition rate ranged between 53% and 94% (Pantazi et al., 2016).

Herrmann et al. (2013) adopted a ground-level image spectroscopy, characterised by high resolution at spatial and spectral level, in order to increase efficiency in weed control in wheat fields. Hyperspectral images were obtained by a push-broom type hyperspectral camera (ImSpector V10E, Specim, Spectral Imaging Ltd., Oulu, Finland) mounted on a tripod. The hyperspectral camera works in the NIR and visible regions, with a spectral range between 400 and 1000 nm and a spectral resolution of 2.8 nm. PLSDA was applied to classify four categories and not for specific species of weeds: i) category BLW (broadleaf weeds) included the species *Chenopodium, Mallow* and potato; ii) category GW (grass weeds) included *Lolium rigidum* and *Hordeum plaucum*, the third and fourth categories corresponded to iii) wheat and iv) soil. The models developed considered a combination of some or all of the categories, even if the spectra were obtained from sunlight pixels and shaded pixels. The best model was the one that included the 4 categories described, but without discriminating between sunlight and shaded pixels. This model was chosen by comparing the cross-validation confusion matrices in terms of variances and the Cohen's Kappa values: K was 0.79 and the total accuracy was 85%. In addition, it was found that the red edge is the most important spectral region for vegetation classes through the application of the variable importance in projection method. The authors concluded that due to high spectral and spatial resolutions it was possible to obtain a separation between wheat and weeds on the basis of their spectral data. This approach could lead to a reduction in herbicides needing and consequently to an improvement both from an environmental and economic point of view so, without diminishing weed control efficiency, to a benefit for farmers and consumers. In addition, reduction of herbicides amount can limit the development of weed resistance to herbicides (Herrmann et al., 2013).

Regarding weed management, it is also useful to detect lesions caused to crops by the spread of a herbicide in the fields next to the one treated, as in the case of dicamba, or the differentiation between resistance and sensitivity to herbicides in weeds, in the case of glyphosate (Huang et al., 2016). For this purpose, Huang et al. (2016) adopted three instruments: i) a handheld spectroradiometer, to quickly measure in-field plant canopy spectra; ii) a push-broom hyperspectral camera (Resonon Pika II, Resonon, Bozeman, MT) with two lamps as a light source for laboratory use, and iii) an on-the-go hyperspectral camera, the same used in laboratory, mounted to a 3-point hitch installed on the back of a standard tractor, for in-field study of plant canopy. The hyperspectral camera works in the range between 400 and 900 nm, providing 240 wavelength bands. The in-field hyperspectral system allowed obtaining an over 90% accuracy on glyphosate-resistant (GR) and glyphosate-sensitive (GS) weeds differentiation. Wind

interference on the linear scanning sensor and sensor overheating due to intense solar irradiation had affected in-field experiment. According to this, the authors reported the needing to remove data artefacts and minimize environmental and systemic interference (Huang et al., 2016).

Reddy et al. (2014) reported that some populations of Palmer amaranth (*Amaranthus palmeri* S. Wats.), weeds present in the southern United States, have developed resistance to glyphosate. Spectra of GR and GS plants were recorded, and the potential of hyperspectral sensors to differentiate GR from GS plants were explored. The study was conducted both in greenhouse and in the field. In greenhouse, a push-broom type hyperspectral camera (Resonon Pika II, Resonon, Bozeman, MT) was mounted on a stand, and two incandescent light bulbs were used as artificial light source. In the field, the same hyperspectral camera was mounted on a three-point hitch, with the capacity to move horizontally and vertically, and with the sun acting as a natural source of light; in turn, the tripod was installed on a tractor. Spectral data were randomly assigned to training and testing groups, and sensitive hyperspectral bands were selected using a forward selection algorithm. Fisher's linear discriminant analysis (FLDA) was used to reduce the dimensionality of the sensitive bands related to the plant set and the maximum likelihood (ML) to classify the plants. Finally, amaranth plants were classified with confusion matrix with predictive accuracy, through leave-one-out validation. Authors observed that four distinct regions of the spectrum (400–500 nm, 650–690 nm, 730–740 nm and 800–900 nm) were able to separate GR from GS plants. Considering fourteen wavebands within or close to these four spectral regions, the validation accuracy of the field model classification was 96.4% and was comparable with that of the greenhouse model, which was 93.8%. In conclusion, it can be stated that hyperspectral imaging has a potential application to differentiate between GR and GS Palmer amaranth plants, without subjecting them to a glyphosate treatment. For this reason, the technique described could have future implications for glyphosate resistance management (Reddy et al., 2014).

3.5.2.8. No tillage in conservative agriculture

Among basic principles of conservation agriculture (CA) are included zero tillage and permanent soil organic cover, which contribute decreasing soil degradation and increasing fertility (Chen et al., 2017; FAO, 2017).

Chen et al. (2017) reported that in North China Plain, where annual maize wheat rotation is commonly implemented, the standing maize stubble, and consequently their extensive root system, stays in the field. These materials can hardly decompose during the short period between maize harvesting and wheat sowing, causing the block of the next no till sowing. To address the above problem, a vision-based guide was

developed. It consisted of a HSI system mounted on a pedestal. The HSI system comprised a spectrograph (1003B-20001 Micro-Hyperspec VNIR A-Series, Headwall Photonics Inc.) with a spectral range between 347.4 and 952.8 nm (Vis-NIR) and a spectral resolution of 1.846 nm, thus providing 329 wavebands; the spectrograph was coupled to a CCD camera, a zoom lens, and a tilt-shift motion control system (PTU-D48E, FLIR). The HSI system was positioned forward during wheat sowing to avoid the standing maize stubble and consequently the underground root system. From the hyperspectral images of the standing maize stubble left in the field, three images with optimal wavebands (484, 561 and 580 nm) were selected by PCA. The three selected images were then enhanced by means of median filter, Sobel filter, Gaussian lowpass filter, band fusion method. In summary, the enhanced images demonstrated the capacity of the selected optimal wavebands to detect maize stubble (Chen et al., 2017).

3.5.2.9. Canopy monitoring under uncontrolled conditions

Rodriguez-Moreno et al. (2016) tested the quality of spectral images acquired under uncontrolled and consequently not optimal circumstances. Multispectral images were acquired from a multispectral camera (DuncanTech MS3100 camera, Auburn, CA, USA) mounted on an on-ground platform without a system to control: i) lighting; ii) the geometry existing between the sun, the target, and the sensor; and iii) interferences (dew, dust, *etc.*). Multispectral images were compared with spectral data obtained from a field radiometer and with hyperspectral images acquired by an airborne hyperspectral sensor. In this way, it was possible to measure the error occurring in crop reflectance as well as to evaluate the consequences of the uncontrolled conditions. It was observed that the error in estimation of crop reflectance was compatible with a proper agronomic interpretation of the images using thresholds, linear functions, or combination of both (Rodriguez-Moreno et al., 2016).

3.5.3. Conclusions

Hyperspectral imaging technology for non-destructive analysis by means of high-resolution proximal sensing of plants directly in the field is currently not widely adopted but promising. HSI can be considered in the field of precision agriculture: it is useful for high-throughput phenotyping, for determining the ‘harvest maturity’ of fruit, for monitoring the physiological state of the plant, parasite attacks, weeds, and consequently for the estimation of the production yield. Some factors complicate the analysis, such as variations in the level of intensity of sunlight, the angle of inclination of the incident solar radiation, overheating of the sensor due to intense solar radiation, the plant architecture that includes the inclination of the leaves and specular reflection,

the wind. Future research should focus on studying solutions to these problems and on automating the process of acquiring and processing the enormous amount of data obtained from the analysis.

3.5.4. References

Al Makdessi, N., Jean, P. A., Ecarnot, M., Gorretta, N., Rabatel, G., & Roumet, P. (2017). How plant structure impacts the biochemical leaf traits assessment from in-field hyperspectral images: A simulation study based on light propagation modeling in 3D virtual wheat scenes. *Field Crops Research*, *205*, 95–105. https://doi.org/10.1016/j.fcr.2017.02.001

Chen, W., Li, H., Niu, Q., & Hongnan, H. (2017). Hyperspectral image segmentation for maize stubble in no-till field. *2017 ASABE Annual International Meeting*, 6. https://doi.org/10.13031/aim.201700963

Deery, D., Jimenez-Berni, J., Jones, H., Sirault, X., & Furbank, R. (2014). Proximal Remote Sensing Buggies and Potential Applications for Field-Based Phenotyping. *Agronomy*, *4*(3), 349–379. https://doi.org/10.3390/agronomy4030349

ElMasry, G., Kamruzzaman, M., Sun, D.-W., & Allen, P. (2012). Principles and Applications of Hyperspectral Imaging in Quality Evaluation of Agro-Food Products: A Review. *Critical Reviews in Food Science and Nutrition*, *52*(11), 999–1023. https://doi.org/10.1080/10408398.2010.543495

ElMasry, G., & Sun, D.-W. (2010). Principles of Hyperspectral Imaging Technology. In D.-W. Sun (Ed.), *Hyperspectral Imaging for Food Quality Analysis and Control* (pp. 3–43). Academic Press. https://doi.org/10.1016/B978-0-12-374753-2.10001-2

FAO (Food and Agriculture Organization of the United Nations). (2017). *Conservation Agriculture* (Factsheet). FAO, Plant Production and Protection Division. http://www.fao.org/3/i7480en/I7480EN.pdf

Garini, Y., Young, I. T., & McNamara, G. (2006). Spectral imaging: Principles and applications. *Cytometry Part A*, *69A*(8), 735–747. https://doi.org/10.1002/cyto.a.20311

Goetz, A., Vane, G., Solomon, J., & Rock, B. (1985). Imaging Spectrometry for Earth Remote Sensing. *Science*, *228*(4704), 1147–1153. https://doi.org/10.1126/science.228.4704.1147

Gutiérrez, S., Fernández-Novales, J., Diago, M. P., & Tardaguila, J. (2018). On-The-Go Hyperspectral Imaging Under Field Conditions and Machine Learning for the Classification of Grapevine Varieties. *Frontiers in Plant Science*, *9*(July), 1–11. https://doi.org/10.3389/fpls.2018.01102

Herrmann, I., Shapira, U., Kinast, S., Karnieli, A., & Bonfil, D. J. (2013). Ground-level hyperspectral imagery for detecting weeds in wheat fields. *Precision Agriculture*, *14*(6), 637–659. https://doi.org/10.1007/s11119-013-9321-x

Huang, Y., Lee, M. A., Thomson, S. J., & Reddy, K. N. (2016). Ground-based hyperspectral remote sensing for weed management in crop production. *International Journal of Agricultural and Biological Engineering*, *9*(2), 98–109. https://doi.org/10.3965/j.ijabe.20160902.2137

Jay, S., Gorretta, N., Morel, J., Maupas, F., Bendoula, R., Rabatel, G., Dutartre, D., Comar, A., & Baret, F. (2017). Estimating leaf chlorophyll content in sugar beet canopies using millimeter- to centimeter-scale reflectance imagery. *Remote Sensing of Environment*, *198*, 173–186. https://doi.org/10.1016/j.rse.2017.06.008

Jensen, J. R. (2014). Multispectral Remote Sensing Systems. In J. R. Jensen (Ed.), *Remote Sensing of the Environment: An Earth Resource Perspective* (2nd ed., pp. 177–242). Pearson Education Limited.

Jiang, Y., Li, C., Robertson, J. S., Sun, S., Xu, R., & Paterson, A. H. (2018). GPhenoVision: A ground mobile system with multi-modal imaging for field-based high throughput phenotyping of cotton. *Scientific Reports*, *8*, *1213*(1), 1–15. https://doi.org/10.1038/s41598-018-19142-2

Liu, D., Sun, D.-W., & Zeng, X.-A. (2014). Recent advances in wavelength selection techniques for hyperspectral image processing in the food industry. *Food and Bioprocess Technology*, *7*(2), 307–323. https://doi.org/10.1007/s11947-013-1193-6

Liu, D., Zeng, X.-A., & Sun, D.-W. (2015). Recent Developments and Applications of Hyperspectral Imaging for Quality Evaluation of Agricultural Products: A Review. *Critical Reviews in Food*

Science and Nutrition, *55*(12), 1744–1757. https://doi.org/10.1080/10408398.2013.777020

Lu, R., & Park, B. (2015). Introduction. In B. Park & R. Lu (Eds.), *Hyperspectral Imaging Technology in Food and Agriculture. Food Engineering Series* (pp. 3–7). Springer, New York, NY. https://doi.org/10.1007/978-1-4939-2836-1_1

Ma, J., Sun, D.-W., Pu, H., Cheng, J.-H., & Wei, Q. (2019). Advanced Techniques for Hyperspectral Imaging in the Food Industry: Principles and Recent Applications. *Annual Review of Food Science and Technology*, *10*(1), 197–220. https://doi.org/10.1146/annurev-food-032818-121155

Malenovský, Z., Turnbull, J. D., Lucieer, A., & Robinson, S. A. (2015). Antarctic moss stress assessment based on chlorophyll content and leaf density retrieved from imaging spectroscopy data. *New Phytologist*, *208*(2), 608–624. https://doi.org/10.1111/nph.13524

Mishra, P., Asaari, M. S. M., Herrero-Langreo, A., Lohumi, S., Diezma, B., & Scheunders, P. (2017). Close range hyperspectral imaging of plants: A review. *Biosystems Engineering*, *164*, 49–67. https://doi.org/10.1016//j.biosystemseng.2017.09.009

Onoyama, H., Ryu, C., Suguri, M., & Iida, M. (2015). Nitrogen prediction model of rice plant at panicle initiation stage using ground-based hyperspectral imaging: growing degree-days integrated model. *Precision Agriculture*, *16*(5), 558–570. https://doi.org/10.1007/s11119-015-9394-9

Onoyama, H., Ryu, C., Suguri, M., & Iida, M. (2018). Estimation of rice protein content before harvest using ground-based hyperspectral imaging and region of interest analysis. *Precision Agriculture*, *19*(4), 721–734. https://doi.org/10.1007/s11119-017-9552-3

Pantazi, X. E., Moshou, D., & Bravo, C. (2016). Active learning system for weed species recognition based on hyperspectral sensing. *Biosystems Engineering*, *146*, 193–202. https://doi.org/10.1016/j.biosystemseng.2016.01.014

Reddy, K. N., Huang, Y., Lee, M. A., Nandula, V. K., Fletcher, R. S., Thomson, S. J., & Zhao, F. (2014). Glyphosate-resistant and glyphosate-susceptible Palmer amaranth (Amaranthus palmeri S. Wats.): Hyperspectral reflectance properties of plants and potential for classification. *Pest Management Science*, *70*(12), 1910–1917. https://doi.org/10.1002/ps.3755

Rinnan, Å., van den Berg, F., & Engelsen, S. B. (2009). Review of the most common pre-processing techniques for near-infrared spectra. *TrAC Trends in Analytical Chemistry*, *28*(10), 1201–1222. https://doi.org/10.1016/j.trac.2009.07.007

Rodriguez-Moreno, F., Zemek, F., Kren, J., Pikl, M., Lukas, V., & Novak, J. (2016). Spectral monitoring of wheat canopy under uncontrolled conditions for decision making purposes. *Computers and Electronics in Agriculture*, *125*, 81–88. https://doi.org/10.1016/j.compag.2016.05.002

Römer, C., Wahabzada, M., Ballvora, A., Pinto, F., Rossini, M., Panigada, C., Behmann, J., Léon, J., Thurau, C., Bauckhage, C., Kersting, K., Rascher, U., & Plümer, L. (2012). Early drought stress detection in cereals : simplex volume maximisation for hyperspectral image analysis. *Functional Plant Biology*, *39*(12), 878–890. https://doi.org/10.1071/FP12060

Thomas, S., Kuska, M. T., Bohnenkamp, D., Brugger, A., Alisaac, E., Wahabzada, M., Behmann, J., & Mahlein, A. K. (2018). Benefits of hyperspectral imaging for plant disease detection and plant protection: a technical perspective. *Journal of Plant Diseases and Protection*, *125*(1), 5–20. https://doi.org/10.1007/s41348-017-0124-6

Underwood, J., Wendel, A., Schofield, B., McMurray, L., & Kimber, R. (2017). Efficient in-field plant phenomics for row-crops with an autonomous ground vehicle. *Journal of Field Robotics*, *34*(6), 1061–1083. https://doi.org/10.1002/rob.21728

Vigneau, N., Ecarnot, M., Rabatel, G., & Roumet, P. (2011). Potential of field hyperspectral imaging as a non destructive method to assess leaf nitrogen content in Wheat. *Field Crops Research*, *122*(1), 25–31. https://doi.org/10.1016/j.fcr.2011.02.003

Wang, B., Zhang, X., Dong, Y., Zhang, J., Zhang, J., & Zhou, X. (2018). Retrieval of Leaf Chlorophyll Content of Paddy Rice with Extracted Foliar Hyperspectral Imagery. *2018 7th International Conference on Agro-Geoinformatics (Agro-Geoinformatics)*, 1–5. https://doi.org/10.1109/Agro-Geoinformatics.2018.8476024

Wendel, A., Underwood, J., & Walsh, K. (2018). Maturity estimation of mangoes using hyperspectral imaging from a ground based mobile platform. *Computers and Electronics in Agriculture*, *155*, 298–313. https://doi.org/10.1016/j.compag.2018.10.021

Whetton, R. L., Waine, T. W., & Mouazen, A. M. (2018). Hyperspectral measurements of yellow rust and fusarium head blight in cereal crops: Part 2: On-line field measurement. *Biosystems Engineering*, *167*, 144–158. https://doi.org/10.1016/j.biosystemseng.2018.01.004

Wu, Q., Wang, C., Fang, J. J., & Ji, J. W. (2016). Field monitoring of wheat seedling stage with hyperspectral imaging. *International Journal of Agricultural and Biological Engineering*, *9*(5), 143–148. https://doi.org/10.3965/j.ijabe.20160905.1707

Yoon, S.-C., & Park, B. (2015). Hyperspectral Image Processing Methods. In B. Park & R. Lu (Eds.), *Hyperspectral Imaging Technology in Food and Agriculture. Food Engineering Series* (pp. 81–101). Springer, New York, NY. https://doi.org/10.1007/978-1-4939-2836-1_4

Zhao, J., Zhang, D., Huang, L., Zhang, Q., Liu, W., & Yang, H. (2016). Vertical features of yellow rust infestation on winter wheat using hyperspectral imaging measurements. *2016 Fifth International Conference on Agro-Geoinformatics (Agro-Geoinformatics)*, 1–4. https://doi.org/10.1109/Agro-Geoinformatics.2016.7577620

3.6. In-field and non-destructive monitoring of grapes maturity by hyperspectral imaging

Scientific publication – Paper VI

Benelli, A., Cevoli, C., Ragni, L., & Fabbri, A. (2021b). In-field and non-destructive monitoring of grapes maturity by hyperspectral imaging. *Biosystems Engineering*, *207*, 59–67. https://doi.org/10.1016/j.biosystemseng.2021.04.006

Alessandro Benelli[a], Chiara Cevoli[a,b*], Luigi Ragni[a,b], Angelo Fabbri[a,b]

[a]*Department of Agricultural and Food Sciences, Alma Mater Studiorum, University of Bologna, Piazza Goidanich 60, Cesena, 47521, Italy*

[b]*Interdepartmental Centre for Agri-Food Industrial Research, Alma Mater Studiorum, University of Bologna, Via Quinto Bucci 336, Cesena, 47521, Italy*

[*]*Corresponding author: chiara.cevoli3@unibo.it*

Abstract

Monitoring the quality attributes of grapes is a practice that allows the state of ripeness to be checked and the optimal harvest time to be identified. A non-destructive method based on hyperspectral imaging (HSI) technology was developed. Analyses were carried out directly in the field on a 'Sangiovese' (*Vitis vinifera* L.) vineyard destined for wine production, by using a Vis/NIR (400–1000 nm) hyperspectral camera. One vineyard row was analysed on 13 different days during the pre-harvest and harvest time. The soluble solids content (SSC) expressed in terms of °Brix was measured by a portable digital refractometer. Afterwards, the grape samples were split in two classes: the first one composed by the samples characterised by a °Brix lower than 20 (not-ripe), while the second one by the samples with a °Brix higher than 20 (ripe). Grape mean spectra were extracted from each hyperspectral image and used to predict the SSC by partial least squares regression (PLS), and to classify the samples into the two classes by PLS discriminant analysis (PLS-DA). SSC was predicted with a R^2=0.77 (RMSECV=0.79 °Brix), and the samples were correctly classified with a percentage from 86 to 91%. Even if the number of wavelengths was limited, the percentages of correctly classified samples were again within the above-mentioned range. The present study shows the potential of the use of HSI technology directly in the field by proximal

measurements under natural light conditions for the prediction of the harvest time of the ‘Sangiovese’ red grape.

Keywords: hyperspectral, in-field, grape, wine, harvest, classification

3.6.1. Introduction

Italy is the largest wine producer in the world, with a production in 2018 of 5,480 million litres (18.8% of world production) (OIV, 2019). In an industrialised wine growing system, monitoring the quality attributes, such as soluble solids content (SSC), acidity and anthocyanin content of grapes is extremely important: well-planned monitoring allows to check the growth and ripening of the grapes, and finally to decide when to proceed with the harvest (Delrot et al., 2010). For instance, by managing irrigation through the use of techniques such as the regulated deficit irrigation, significant increases in SSC and anthocyanins can be achieved which together with a decrease in yield and berry size can lead to substantial improvements in grape quality (Acevedo-Opazo et al., 2010; Pellegrino et al., 2005).

Monitoring of grape quality attributes can be carried out directly in the field using traditional destructive techniques. Alternatively, quality attributes can be estimated by non-destructive techniques, such as near-infrared (NIR) spectroscopy. Portable NIR instruments were used to determine the following quality attributes of grapes: water content, SSC, reductant sugars, pH, titratable acidity, maturity index (sugar/acidity ratio), extractable anthocyanins, potential anthocyanins (Teixeira Dos Santos et al., 2013).

Over the last two decades the use of HSI technology in the quality assessment of fruits and vegetables has become of increasing interest (Chandrasekaran et al., 2019; Liu et al., 2015). HSI was initially limited to controlled environments such as laboratories but gradually, thanks to the miniaturisation and improved computing and data storage capabilities, it began to be used directly in the field (Benelli et al., 2020). Hyperspectral images can be captured either remotely by airborne vehicles and unmanned aerial vehicles (Ishida et al., 2018; Matese & Di Gennaro, 2015; Zarco-Tejada et al., 2013) or by ground vehicles (Deery et al., 2014; Gutiérrez et al., 2018; Huang et al., 2016; Jay et al., 2017; Underwood et al., 2017; Wendel et al., 2018; Whetton et al., 2018), which produces proximal hyperspectral images with high spatial resolution. Proximal HSI could therefore allow non-destructive, contactless, and automated monitoring of grape quality attributes. Moreover, the acquisition of hyperspectral images can be performed continuously, enabling the rapid scanning of large areas. Hyperspectral data

is characterised by two spatial and one spectral dimension, therefore only specific regions of interest (ROIs) can be selected, and the residual regions can be excluded. In this sense, hyperspectral analysis is useful to guide the choice of true multispectral less expensive solutions.

Concerning in-field grape studies, Gutiérrez et al. (2018) adopted an on-the-go HSI system for the classification of 30 grapevine varietals directly acquired in the field. Through the development of classification models based on support vector machines (SVM) and multilayer perceptron (MLP), prediction performance (F1 score) up to 0.99 was achieved. The same on-the-go HSI system described above, combined with SVM, was adopted to estimate SSC and anthocyanin concentration of wine grapes (Gutiérrez et al., 2019). Determination coefficients (R^2) of 0.92 (RMSE=1.274 °Brix) and 0.83 (RMSE=0.211 mg g^{-1}) were obtained for the prediction of SSC and anthocyanin concentration, respectively. These two studies highlight the potential of HSI to monitor the indices of grape ripening directly in the field and therefore to improve vineyard decisions and management. Non-linear statistical methods were used in both studies. Considering the results just mentioned, it would be interesting to investigate whether, even combining HSI with linear methods and reducing the number of wavelengths, it is possible to monitor the degree of grape maturity directly in the field. Furthermore, considering a possible application of this technique, a simple binary model able to simply determine whether grapes are ripe for harvesting could be interesting.

Thus, the present study aims to identify the proper degree of ripeness, suitable for harvesting wine grapes, through the observation of the SSC evolution by means of HSI technology applied directly in the field. The mean spectra were extracted from each hyperspectral image and used to predict the SSC and to classify the samples into the two classes (not-ripe and ripe), by partial least squares regression (PLS) and discriminant analysis (PLS-DA), respectively.

3.6.2. Materials and methods

3.6.2.1. Samples

One side of a row of ‘Sangiovese’ (*Vitis vinifera* L.) grape vineyards, located near Cesena, Italy, was analysed on 13 different days in the period between August 20th and October 4th, 2019 (from pre-harvest to harvest time). The row was divided into 11 sections; from each section 3, grapes were taken for each day of analysis, for a total of 429 samples.

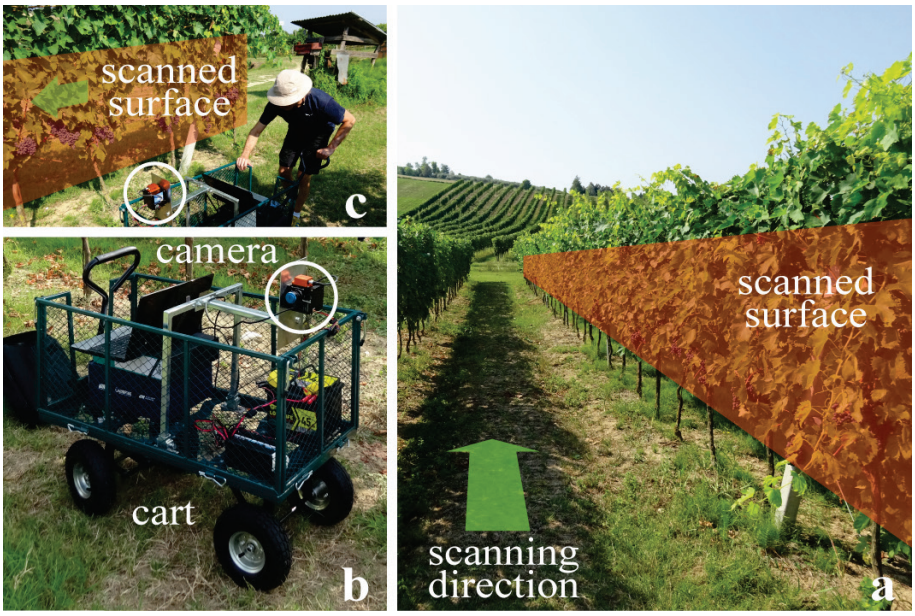

Fig. 3.6.1 – (a) Vineyard row, highlighted by the purple surface, scanned with the Vis/NIR hyperspectral camera; the red arrow indicates the direction of scanning; (b) Garden cart on which the hyperspectral camera is mounted. (c) In field hyperspectral imaging to measure soluble solids content of wine grape berries during ripening.

3.6.2.2. Hyperspectral acquisitions

The adopted push-broom hyperspectral camera (Nano-Hyperspec VNIR, Headwall Photonics, Inc., Fitchburg, MA, USA) scans single lines in a sequence, each one consisting of 640 voxels: the image is created by moving the camera along the scanning direction (Fig. 3.6.1a). Each voxel contains, in addition to the two spatial dimensions, a Vis/NIR spectrum (400–1000 nm) characterized by 272 spectral bands, with a nominal spectral resolution of 2.2 nm. The mounted lens has an effective focal length of 17 mm, with the optical axis perpendicular to the side of the vineyard row (scanned surface) analysed (Fig. 3.6.1c). The camera was installed on a garden cart (Fig. 3.6.1b) 120 cm above the ground and it was powered by a 12 V, 45 Ah automotive battery through a DC to AC power inverter. The scans were performed at about 1.6 m from the side of the vineyard row.

Direct sunlight with clear sky conditions, was used as a light source. To reduce the fluctuation of the sample temperature, all the acquisitions were carried during the same period of the day, from 10:30 a.m. to 12:00 p.m.

The frame rate was set to approximately 100 frames·s^{-1}. The exposure time was set from 6 to 8 ms, depending on the light intensity, and was achieved through calibration, by framing a white high-reflectance matter panel, placed at the same distance as the vineyard row, to cover the entire angle of view of the camera. Given the clear sky conditions and the short time required, about 10 min, acquisition of hyperspectral images of the 11 vineyard row sections and calibration was carried out only once per day.

The raw diffuse reflectance spectrum (R_R) was extracted from the HS images. The calibrated diffuse reflection spectrum (R_C) was calculated by applying the following equation (Guo et al., 2019):

$$R_C = \frac{R_R - R_D}{R_W - R_D} \quad (1)$$

where R_D is the reflectance spectrum of dark reference, obtained by applying the cap on the lens; R_W is the reflectance spectrum of white reference, obtained by means calibration with the white high-reflectance matte panel reported above.

A hyperspectral image from each of the 11 sections obtained from the vineyard row, was acquired per day of analysis (Fig. 3.6.1c): therefore, during the 13 days of analysis, a total of 143 vineyard row sections were scanned.

3.6.2.3. Soluble solids content measurement

After the acquisition of the images, the SSC, expressed in °Brix, was measured on 3 grape berries (randomly selected) from each of the 11 sections by using a portable digital refractometer (PR-101 Digital Refractometer, ATAGO CO., LTD, Tokyo, Japan). Subsequently, the mean for each section was calculated.

One-way analysis of variance (ANOVA) with Tukey-HSD post-hoc test (p-level<0.05) was applied to evaluate significant differences between SSC means over the different days of analysis.

3.6.2.4. Hyperspectral images elaboration

ROI selection was made using the software HyperCube, v. 11.52 (U.S. Army Engineer Research and Development Center (ERDC), USA). For each image, 5 points and a maximum of a further 120 adjacent points (11×11 voxels matrix, with the selected point in the centre of the matrix) were selected on 5 different berries directly illuminated by the sun, not in the shade. The (reference) points included in the classification were characterized by a metric distance from the mean (signature) spectrum of the manually selected points within the range (tolerance threshold) [0,0.04] (Fig. 3.6.2). The metric distance (d) was calculated by applying the absolute difference (Manhattan) function (Eq. (2)) (Deborah et al., 2015) and normalised in the range [0,1]:

$$d(R_1, R_2) = \sum_{\lambda} \left| R_{1,\lambda} - R_{2,\lambda} \right| \quad (2)$$

where R_1, R_2 are two reflectance spectra.

From the spectra of the classified points, the mean spectrum for each hyperspectral image was calculated.

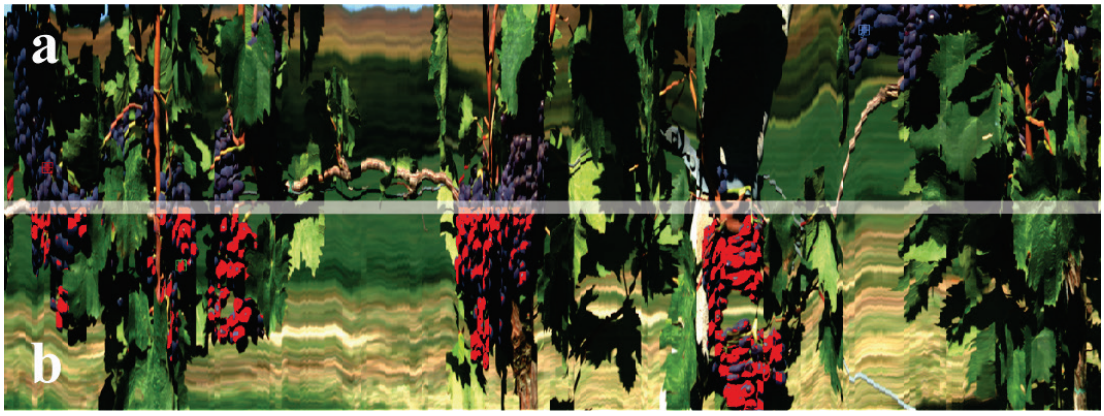

Fig. 3.6.2 – (a) RGB image from hyperspectral image of a scanned vineyard row section. (b) Representation of the ROI (in red) resulting from the classification obtained by the Manhattan function.

The spectral bands between 400–424 nm were omitted as a result of the low signal-to-noise ratio produced by the sensor, as reported in Wendel et al. (2018). The spectra were smoothed (Savitzky-Golay method; polynomial order: 2; smoothing points: 15) to reduce noise from the spectra and following pre-treated by the standard normal variate (SNV) method, first derivative (D1) and finally mean centred (MC). The SNV is one of the most common pre-processing methods used to correct spectra for changes in optical path length and light scattering, while the derivatives have the capability to remove both additive and multiplicative effects in the spectra (Rinnan et al., 2009). After SNV, each spectrum will have a mean of 0 and a standard deviation of 1.

Principal component analysis (PCA) was applied to the mean spectra as exploratory technique to visualize the data according to °Brix and time evolution. Subsequently, a preliminary PLS regression model was built to estimate the SSC. The validation was carried out by the venetian blind cross-validation method (segments: 10).

PLS-DA models were built to classify the samples according to °Brix. In particular, classification models with 2 categories (not-ripe and ripe) were developed: according to Bucelli et al. (2010), the first class was composed by the samples characterized by a °Brix lower than 20 (0), while the second one by the samples with a °Brix equal or higher than 20 (1).

The sample dataset (n=143) was split in calibration (venetian blinds cross-validation, including 75% of the samples) and external validation set (25% of the samples) by using the Onion method (Gallagher & O'sullivan, 2020). The threshold value, able to identify the belonging category of each sample into one of the groups, was defined by using a probabilistic approach based on Bayes's rule. To avoid the model over-fitting, the optimal number of latent variables were chosen by plotting the root mean square error of cross-validation (RMSECV) as a function of the number of components and by identifying where the curve reaches a local minimum. The receiver operating

characteristic (ROC) curves in prediction were evaluated to assess the goodness of the models.

All the chemometrics models were developed by using PLS Toolbox for Matlab2018a.

3.6.3. Results and discussion

Means and standard deviation of the °Brix measured during the 13 days of analysis are reported in Table 3.6.1. The increase between the first and last day was of 27.5%, from 17.8 °Brix (day I) to 22.7 °Brix (day XIII). Several significant differences between the °Brix mean values were achieved over the different days of analysis. The whole data set was characterized by a mean value of 20.6±1.7 °Brix, which make suitable to split it in two subsets with a threshold of 20 °Brix.

Table 3.6.1 – Mean and standard deviation values of soluble solids content (°Brix) as a function of days of analysis.

Day of analysis	Mean (°Brix)	SD (°Brix)
I	17.8^{a}	1.05
II	$19.0^{a,b}$	0.81
III	$19.2^{b,c}$	0.75
IV	$19.9^{b,c,d}$	1.1
V	$20.1^{b,c,d}$	1.16
VI	$20.2^{b,c,d,e}$	0.95
VII	$20.5^{c,d,e,f}$	1.11
VIII	$20.7^{d,e,f}$	0.82
IX	$21.5^{e,f,g}$	0.76
X	$21.6^{e,f,g}$	0.89
XI	$21.7^{f,g}$	1.17
XII	22.7^{g}	0.94
XIII	22.7^{g}	0.88

Note: means with the same letter are not significant different at p-level<0.05.

Raw and pre-treated (smoothing and SNV) mean spectra of all the samples by day of analysis are presented in Fig. 3.6.3. In the Vis/NIR region (400–1000 nm), the visible spectrum (400–700 nm) presents the absorption bands of some substances used as ripening indexes of fruit: anthocyanins at around 500 nm, carotenoids at 570–590 nm, and chlorophyll *a* at 680–710 nm (ElMasry et al., 2007; Munera et al., 2017). In the NIR region (700–1000 nm), absorption bands of water at 760 nm and 960–970 nm are characterised by the overtone of O–H bonds (McGlone & Kawano, 1998; Nicolaï et al., 2007): since the water content of a ripe wine grape is 70–80% (FAO, 2009), it can be expected that the water related absorption band will prevail. Absorption band around 840 nm was associated with sugar (Pu et al., 2016); moreover, peaks observed in the 950–1000 nm region were related to both water and carbohydrates, as the second overtone of O–H and N–H, a combination band of O–H bonds and the third overtone

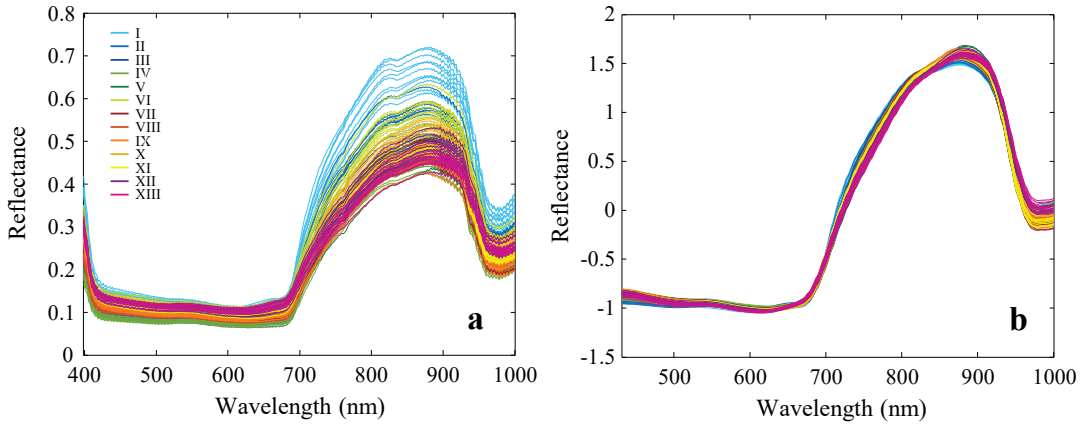

Fig. 3.6.3 – Raw (a) and pre-treated by smoothing and SNV (b) spectra of all samples on different days of analysis (from I to XIII).

of C–H, were found in the region (Camps & Christen, 2009). As observed, the water absorption peaks in the NIR (700–1000 nm) spectral region are not very marked and wide. Therefore, spectral information from SSC in the 800–1000 nm range will tend to be less covered by water (Camps & Christen, 2009; Manley et al., 2007).

The scores plot of the first two principal components (PC1: 59%; PC2: 28%) resulting from PCA shows the samples distribution according to the day of analysis. A tendency to place the samples from left to right can be observed on PC1, starting from day I (quadrant III) to day XIII (quadrant IV) (Fig. 3.6.4a).

A similar distribution can be observed according to the SSC: the samples are distributed along PC1, mainly on the left those with SSC<20 °Brix (quadrants II and III), on the right those with SSC≥22 °Brix (quadrants I and IV) (Fig. 3.6.4b).

The best PLS results were obtained pre-treating the spectra by SNV+MC. Particularly, R^2=0.768 and RMSECV=0.79 °Brix were achieved in cross-validation with 7 latent

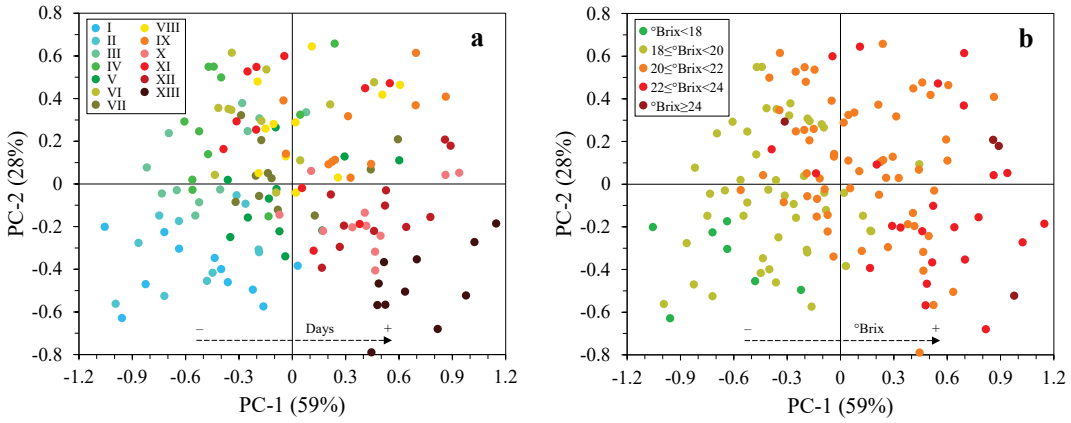

Fig. 3.6.4 – Scores plots obtained by the PCA according to: (a) days of analysis (from I to XIII); (b) soluble solids content (°Brix).

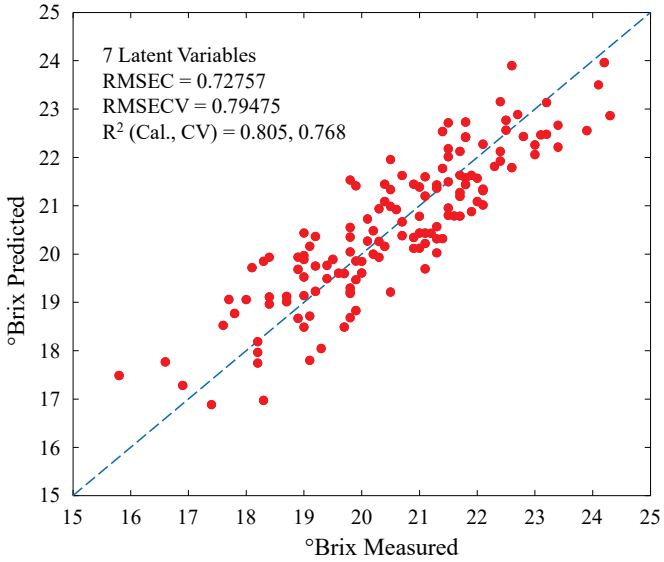

Fig. 3.6.5 – Measured vs predicted values of soluble solids content (°Brix) obtained by PLS regression (cross-validation).

variables. Fig. 3.6.5 shows the predicted versus measured °Brix values. These results agree with those present in literature and developed by using spectra in the same wavelength range and acquired directly in-field. Furthermore, regardless of the R^2 values, the RMSE is substantially lower. Diezma-Iglesias et al. (2008) predicted SSC on 480 samples of 'Cabernet Sauvignon' by using a portable hand-held spectrometer (590–1090 nm), reporting a R^2=0.72, while Guidetti et al. (2010) working with a simple Vis/NIR system in the range from 400 to 1000 nm, obtained in prediction r=0.82 (R^2=0.67) and RMSEP=1.48°Brix. Gutiérrez et al. (2019) used the HSI technique (400–1000 nm) to measure SSC in wine grapes in real time. R^2 of 0.91 (RMSE=1.358 °Brix) and 0.92 (RMSE=1.274 °Brix) were achieved in cross-validation and prediction, respectively, by using the SVM techniques.

PLS-DA results, in terms of percentage of correctly classified samples, are reported in Table 3.6.2. The percentages ranged from 86 to 91%. Considering the prediction set, the best result was obtained applying as pre-treatment the SNV+MC. The results obtained with the hyperspectral technique improved those achieved by Guidetti et al. (2010) by using of a portable contact system. The authors combined Vis/NIR

Table 3.6.2 – PLS-DA results in terms of percentages of correctly classified samples (whole spectral range).

Spectra pretreatment	Class	Calibration (n=107)	Cross-validation (n=107, 10 segments)	Prediction (n=36)	LV
SNV+MC	°Brix<20	89%	89%	91%	4
	°Brix≥20	91%	91%	91%	
SNV+D1+MC	°Brix<20	91%	89%	86%	4
	°Brix≥20	91%	91%	91%	

Note: SNV=Standard Normal Variate; MC=Mean Centred; D1=first derivative, LV=Latent Variable.

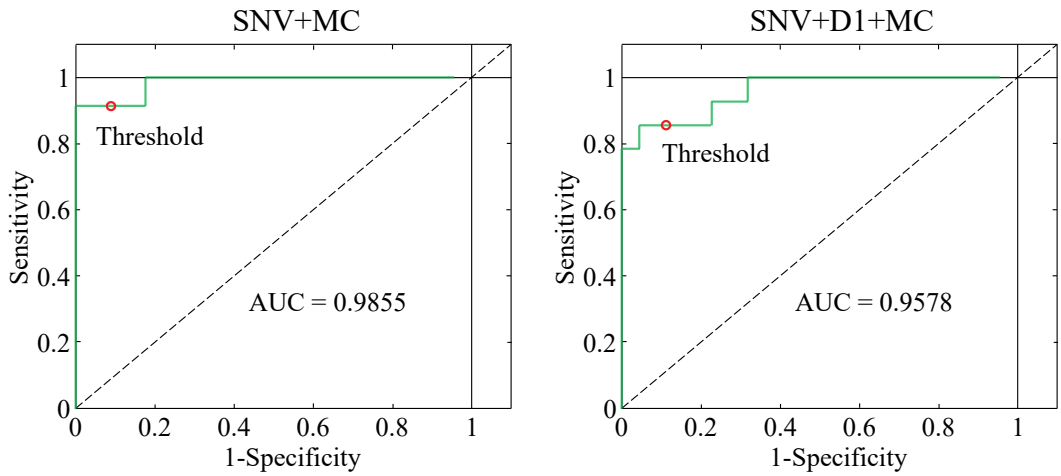

Fig. 3.6.6 – ROC curve of the PLS-DA models in prediction.

spectroscopy in the wavelength range 450–980 nm with PLS-DA to classify grape samples in two groups based on SSC (threshold=21 °Brix), obtaining a percentage of samples correctly classified (in prediction) of 77.1% (Guidetti et al., 2010).

The ROC curves in prediction (Fig. 3.6.6) summarise the trade-off between specificity (number of samples predicted to not be in the class divided by the actual number not in the class) and sensitivity (number of samples predicted to be in the class divided by number actually in the class) for the PLS-DA classification models. The area under the curves (AUC=0.9855 for SNV+MC and AUC=0.9578 for SNV+D1+MC) suggest that the models were characterised by a high degree of discrimination, confirming that the best model was those developed considering only the SNV+MC as pre-treatment.

Results, in terms of probability (Bayes's rule) of belonging to the class °Brix<20, are shown in Fig. 3.6.7. The higher a sample is placed, the higher the probability that it will be classified as a member of the °Brix<20 class. Consequently, samples classified as members of the other class (°Brix≥20) are placed at the bottom of the graph. The

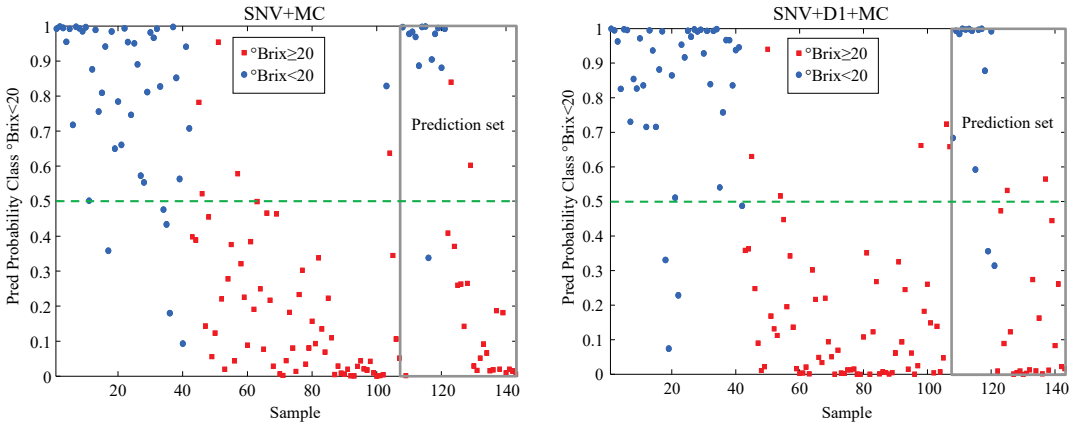

Fig. 3.6.7 – Probability values of belonging to the class °Brix<20.

threshold value (dotted red line) was set at 0.5 (probability of 50%); samples with a probability lower than this value are considered improperly classified.

Considering the SNV+MC and SNV+D1+MC pre-treatments, 89% and 77% of the samples (in prediction) were classified with a probability higher than 70%.

Fig. 3.6.8 shows the VIP (variable importance in projection) scores obtained by the PLS-DA models. These scores estimate the importance of each variable in the projection used in the PLS-DA model. A variable with a VIP score close to or higher than 1 can be considered important in a given model. For both the pre-treatments, similar regions with VIP score higher than 1 were obtained, suggesting that the wavelengths with the highest contribution are in the NIR region of the spectrum (from 700 to 1000 nm). Consequently, the variable selection method based on the VIP scores higher than 1 was used to reduce the original data set.

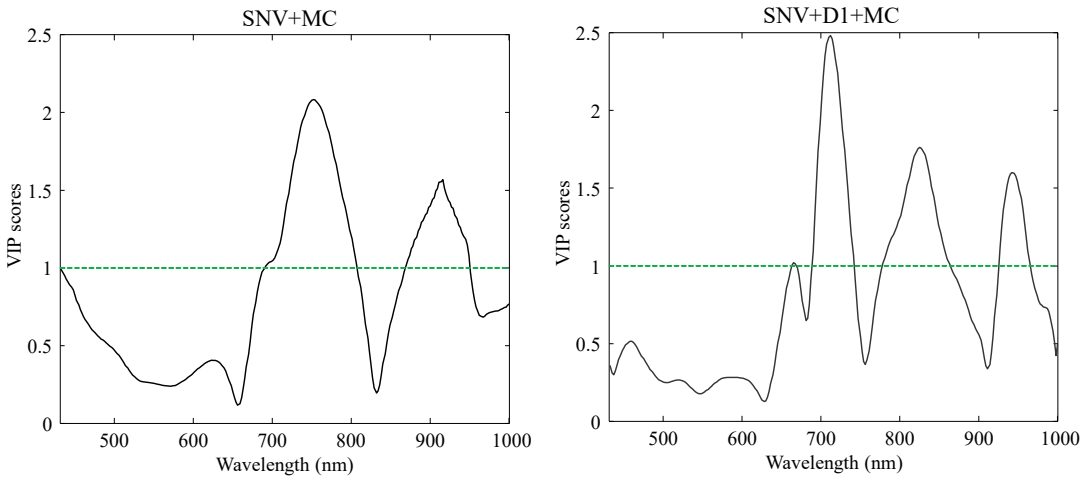

Fig. 3.6.8 – VIP scores of the PLS-DA models.

PLS-DA results (percentage of correctly classified samples) obtained by using the reduced number of variables (wavelengths), are reported in Table 3.6.3. In particular, 93 (SNV+MC) and 88 (SNV+D1+MC) x-variables were used to develop the new PLS-DA. The percentages of correctly classified samples are slightly lower (from 86 to 91%) than those obtained considering the whole spectrum. However, the results are

Table 3.6.3 – PLS-DA results in terms of percentages of correctly classified samples (reduced spectral range).

Spectra pretreatment	Class	Calibration (n=107)	Cross-validation (n=107, 10 segments)	Prediction (n=36)	LV
SNV+MC	°Brix<20	84%	83%	86%	4
	°Brix≥20	93%	92%	91%	
SNV+D1+MC	°Brix<20	89%	89%	88%	3
	°Brix≥20	90%	87%	87%	

Note: SNV=Standard Normal Variate; MC=Mean Centred; D1=first derivative, LV=Latent Variable.

still completely acceptable. This confirms also by the high AUC values (0.939 and 0.942).

This work presents a solution for in-field and non-destructively determination of grape maturity degree by using HSI combined with linear chemometric techniques. Particularly, the results confirm the suitability for estimating the soluble solids content of red grapes.

The positioning of the vineyard row did not create any obstacles regarding the direct solar lighting of the grape bunches. The images along the vineyard row were acquired in the NNE-SSO direction, with the row on the right-hand side of the scanning direction. Consequently, the suitable period for analysis was during the late morning and not later than midday. To scan the other side of the row, it would have been necessary to proceed after midday. Shadows also did not present any problems, as the sun was behind the camera at the time of the acquisitions. To correctly acquire hyperspectral images, the vines should be stripped to ensure that the upper leaves do not overshadow the grapes below. Grapes often had reflection and shaded areas, which need to be excluded during the selection of the ROIs, along with fully or partially shaded grape bunches. In the presence of clouds or even just a slight cloud cover, a significant variation in light intensity was observed: this means that the camera would need to be recalibrated every time a section of the row was scanned. In addition, it is possible that the brightness conditions change soon after calibration, so it would be necessary to recalibrate and immediately proceed with the scan of the row section.

The variability grape of a vineyards, in terms of SSC, often is quite high. This depends on many factors, such us the vineyards orientation, unevenness of the land and meteorological phenomena. For this reason, the grapes are harvested at different times even along the same row. Consequently, to optimise the harvest, a technique that allows to have a mapping of the SSC for all grapes, would certainly be an advantage.

3.6.4. Conclusions

Hyperspectral imaging technology, usually adopted in laboratories with auxiliary artificial lighting, was used in-field under natural lighting conditions to monitor the maturity degree of ‘Sangiovese’ (*Vitis vinifera* L.) grapes. The results achieved confirm that it is possible to predict the soluble solids content and to classify grape samples into two classes (not-ripe and ripe) using a linear technique to elaborate the spectral data. Furthermore, the classification performance remained substantially unchanged by reducing the number of wavelengths, so it is expected that a less expensive multispectral camera in the 400–1000 nm range can work just as well. The implementation of a hyperspectral imaging system on an agricultural vehicle coupled

to a gimbal stabilisation system, together with the development of hyperspectral image segmentation techniques, would allow on-the-go analysis of large vineyard extensions. Attention should be paid to the presence of water on the surface of the sample under analysis, to the presence of variable cloudiness and, if the leaves are analysed, to the presence of wind.

3.6.5. References

Acevedo-Opazo, C., Ortega-Farias, S., & Fuentes, S. (2010). Effects of grapevine (Vitis vinifera L.) water status on water consumption, vegetative growth and grape quality: An irrigation scheduling application to achieve regulated deficit irrigation. *Agricultural Water Management*, *97*(7), 956–964. https://doi.org/10.1016/j.agwat.2010.01.025

Benelli, A., Cevoli, C., & Fabbri, A. (2020). In-field hyperspectral imaging: An overview on the ground-based applications in agriculture. *Journal of Agricultural Engineering*, *LI*:1030, 129–139. https://doi.org/10.4081/jae.2020.1030

Bucelli, P., Costantini, E. A. C., & Storchi, P. (2010). It is possible to predict sangiovese wine quality through a limited number of variables measured on the vines. *Journal International Des Sciences de La Vigne et Du Vin*, *44*(4), 207–218. https://doi.org/10.20870/oeno-one.2010.44.4.1473

Camps, C., & Christen, D. (2009). On-tree follow-up of apricot fruit development using a hand-held NIR instrument. *Journal of Food, Agriculture and Environment*, *7*(2), 394–400.

Chandrasekaran, I., Panigrahi, S. S., Ravikanth, L., & Singh, C. B. (2019). Potential of Near-Infrared (NIR) Spectroscopy and Hyperspectral Imaging for Quality and Safety Assessment of Fruits: an Overview. *Food Analytical Methods*, *12*(11), 2438–2458. https://doi.org/10.1007/s12161-019-01609-1

Deborah, H., Richard, N., & Hardeberg, J. Y. (2015). A Comprehensive Evaluation of Spectral Distance Functions and Metrics for Hyperspectral Image Processing. *IEEE Journal of Selected Topics in Applied Earth Observations and Remote Sensing*, *8*(6), 3224–3234. https://doi.org/10.1109/jstars.2015.2403257

Deery, D., Jimenez-Berni, J., Jones, H., Sirault, X., & Furbank, R. (2014). Proximal remote sensing buggies and potential applications for field-based phenotyping. *Agronomy*, *4*(3), 349–379. https://doi.org/10.3390/agronomy4030349

Delrot, S., Medrano, H., Or, E., Bavaresco, L., & Grando, S. (2010). Preface. In *Methodologies and Results in Grapevine Research* (pp. 1–448). Springer, Dordrecht. https://doi.org/10.1007/978-90-481-9283-0

Diezma-Iglesias, B., Barreiro, P., Blanco, R., & García-Ramos, F. J. (2008). Comparison of robust modeling techniques on NIR spectra used to estimate grape quality. *Acta Horticulturae*, *802*, 367–372. https://doi.org/10.17660/ActaHortic.2008.802.48

ElMasry, G., Wang, N., ElSayed, A., & Ngadi, M. (2007). Hyperspectral imaging for nondestructive determination of some quality attributes for strawberry. *Journal of Food Engineering*, *81*(1), 98–107. https://doi.org/10.1016/j.jfoodeng.2006.10.016

FAO (Food and Agriculture Organization). (2009). *Grapes Wine - Agribusiness Handbook*. http://www.fao.org/3/al176e/al176e.pdf

Gallagher, N. B., & O'sullivan, D. (2020). Selection of representative learning and test sets using the onion method. *White Paper Eigenvector*. https://eigenvector.com/wp-content/uploads/2020/01/Onion_SampleSelection.pdf

Guidetti, R., Beghi, R., & Bodria, L. (2010). Evaluation of grape quality parameters by a simple VIS/NIR system. *Transactions of the ASABE*, *53*(2), 477–484. https://doi.org/10.13031/2013.29556

Guo, W., Li, W., Yang, B., Zhu, Z. Z., Liu, D., & Zhu, X. (2019). A novel noninvasive and cost-effective handheld detector on soluble solids content of fruits. *Journal of Food Engineering*, *257*, 1–9. https://doi.org/10.1016/j.jfoodeng.2019.03.022

Gutiérrez, S., Fernández-Novales, J., Diago, M. P., & Tardaguila, J. (2018). On-the-go hyperspectral imaging under field conditions and machine learning for the classification of grapevine varieties. *Frontiers in Plant Science*, *9*. https://doi.org/10.3389/fpls.2018.01102

Gutiérrez, S., Tardaguila, J., Fernández-Novales, J., & Diago, M. P. (2019). On-the-go hyperspectral

imaging for the in-field estimation of grape berry soluble solids and anthocyanin concentration. *Australian Journal of Grape and Wine Research*, *25*(1), 127–133. https://doi.org/10.1111/ajgw.12376

Huang, Y., Lee, M. A., Thomson, S. J., & Reddy, K. N. (2016). Ground-based hyperspectral remote sensing for weed management in crop production. *International Journal of Agricultural and Biological Engineering*, *9*(2), 98–109. https://doi.org/10.3965/j.ijabe.20160902.2137

Ishida, T., Kurihara, J., Viray, F. A., Namuco, S. B., Paringit, E. C., Perez, G. J., Takahashi, Y., & Marciano, J. J. (2018). A novel approach for vegetation classification using UAV-based hyperspectral imaging. *Computers and Electronics in Agriculture*, *144*(December 2017), 80–85. https://doi.org/10.1016/j.compag.2017.11.027

Jay, S., Gorretta, N., Morel, J., Maupas, F., Bendoula, R., Rabatel, G., Dutartre, D., Comar, A., & Baret, F. (2017). Estimating leaf chlorophyll content in sugar beet canopies using millimeter- to centimeter-scale reflectance imagery. *Remote Sensing of Environment*, *198*, 173–186. https://doi.org/10.1016/j.rse.2017.06.008

Liu, D., Zeng, X. A., & Sun, D. W. (2015). Recent Developments and Applications of Hyperspectral Imaging for Quality Evaluation of Agricultural Products: A Review. *Critical Reviews in Food Science and Nutrition*, *55*(12), 1744–1757. https://doi.org/10.1080/10408398.2013.777020

Manley, M., Joubert, E., Myburgh, L., Lotz, E., & Kidd, M. (2007). Prediction of soluble solids content and post-storage internal quality of Bulida apricots using near infrared spectroscopy. *Journal of Near Infrared Spectroscopy*, *15*(3), 179–188. https://doi.org/10.1255/jnirs.725

Matese, A., & Di Gennaro, S. F. (2015). Technology in precision viticulture: A state of the art review. *International Journal of Wine Research*, *7*(1), 69–81. https://doi.org/10.2147/IJWR.S69405

McGlone, V. A., & Kawano, S. (1998). Firmness, dry-matter and soluble-solids assessment of postharvest kiwifruit by NIR spectroscopy. *Postharvest Biology and Technology*, *13*(2), 131–141. https://doi.org/10.1016/S0925-5214(98)00007-6

Munera, S., Besada, C., Blasco, J., Cubero, S., Salvador, A., Talens, P., & Aleixos, N. (2017). Astringency assessment of persimmon by hyperspectral imaging. *Postharvest Biology and Technology*, *125*, 35–41. https://doi.org/10.1016/j.postharvbio.2016.11.006

Nicolaï, B. M., Beullens, K., Bobelyn, E., Peirs, A., Saeys, W., Theron, K. I., & Lammertyn, J. (2007). Nondestructive measurement of fruit and vegetable quality by means of NIR spectroscopy: A review. *Postharvest Biology and Technology*, *46*(2), 99–118. https://doi.org/10.1016/j.postharvbio.2007.06.024

OIV (International Organisation of Vine and Wine). (2019). *2019 Statistical Report on World Vitiviniculture*. https://www.oiv.int/public/medias/6782/oiv-2019-statistical-report-on-world-vitiviniculture.pdf

Pellegrino, A., Lebon, E., Simonneau, T., & Wery, J. (2005). Towards a simple indicator of water stress in grapevine (Vitis vinifera L.) based on the differential sensitivities of vegetative growth components. *Australian Journal of Grape and Wine Research*, *11*(3), 306–315. https://doi.org/10.1111/j.1755-0238.2005.tb00030.x

Pu, H., Liu, D., Wang, L., & Sun, D. W. (2016). Soluble Solids Content and pH Prediction and Maturity Discrimination of Lychee Fruits Using Visible and Near Infrared Hyperspectral Imaging. *Food Analytical Methods*, *9*(1), 235–244. https://doi.org/10.1007/s12161-015-0186-7

Rinnan, Å., van den Berg, F., & Engelsen, S. B. (2009). Review of the most common pre-processing techniques for near-infrared spectra. *TrAC Trends in Analytical Chemistry*, *28*(10), 1201–1222. https://doi.org/10.1016/j.trac.2009.07.007

Teixeira Dos Santos, C. A., Lopo, M., Páscoa, R. N. M. J., & Lopes, J. A. (2013). A review on the applications of portable near-infrared spectrometers in the agro-food industry. *Applied Spectroscopy*, *67*(11), 1215–1233. https://doi.org/10.1366/13-07228

Underwood, J., Wendel, A., Schofield, B., McMurray, L., & Kimber, R. (2017). Efficient in-field plant phenomics for row-crops with an autonomous ground vehicle. *Journal of Field Robotics*, *34*(6), 1061–1083. https://doi.org/10.1002/rob.21728

Wendel, A., Underwood, J., & Walsh, K. (2018). Maturity estimation of mangoes using hyperspectral

imaging from a ground based mobile platform. *Computers and Electronics in Agriculture*, *155*(June), 298–313. https://doi.org/10.1016/j.compag.2018.10.021

Whetton, R. L., Waine, T. W., & Mouazen, A. M. (2018). Hyperspectral measurements of yellow rust and fusarium head blight in cereal crops: Part 2: On-line field measurement. *Biosystems Engineering*, *167*, 144–158. https://doi.org/10.1016/j.biosystemseng.2018.01.004

Zarco-Tejada, P. J., Guillén-Climent, M. L., Hernández-Clemente, R., Catalina, A., González, M. R., & Martín, P. (2013). Estimating leaf carotenoid content in vineyards using high resolution hyperspectral imagery acquired from an unmanned aerial vehicle (UAV). *Agricultural and Forest Meteorology*, *171–172*, 281–294. https://doi.org/10.1016/j.agrformet.2012.12.013

3.7. Automatic selection of the regions of interest from moving wagon hyperspectral images of grapes and SSC prediction

3.7.1. Introduction

Vines are one of the most important crops in Europe, playing a key environmental and socio-economic role (Droulia & Charalampopoulos, 2021). In particular, the Mediterranean area is world leading in wine production. In 2021, Italy, Spain and France together accounted for 79% of EU wine production, while on a global scale they reached 45% (OIV, 2021). Italy has the first place with a production of 44.5 million hectolitres (MhL), followed by Spain with 35.0 MhL and France with 34.2 MhL (OIV, 2021).

As all other agricultural products, the wine sector is strongly influenced by the ongoing global climate change. The global rise in temperature is caused by the increase in atmospheric CO_2 originating from human activity (Keller, 2020b). Specific thermal and hydrologic conditions are the two most frequently cited factors in arguments regarding the potential effects of climate change on viticulture (Droulia & Charalampopoulos, 2021). In addition, the angle of penetration of solar radiation into the canopies also affects grape temperature and composition (Hunter et al., 2021). Water-saving irrigation methods based on vine physiology, such as regulated deficit irrigation (RDI), partial root zone drying irrigation (PRI), and subsurface drip irrigation strategies, are essential for improving both water efficiency as well as berry and wine quality. Furthermore, in order to design agricultural systems, including vineyards, that are sustainable and resilient to climate change, sustainable soil management practices such as cover crops, mulching, composting, reduced tillage, mutualistic plant-microorganism interactions, and agroforestry could be implemented (Romero et al., 2022).

Future climate changes could make new areas suitable for vine cultivation, require significant movement within current growing areas, affect the phenological timing of vines, and eventually alter the composition of grapes and wine (Droulia & Charalampopoulos, 2021). An already evident effect of climate change is the tendency to anticipate and accelerate the phenological phases flowering, veraison and harvest. The period between budbreak and harvest tends to shorten and ripening to move toward the warmer part of the growing season of grapes. If ripening occurs earlier, there is less time for the pre-veraison synthesis of organic acids and flavanols, which

can be also precursors of tannins. In addition, an early and rapid accumulation of sugars occurs during ripening, which is not necessarily coupled with the accumulation of anthocyanin pigments and aromatic components. This can lead to a decision to delay the harvest, resulting in wines with increasingly higher alcohol contents (Keller, 2020a).

In the mid-1980s, the concept of precision agriculture (PA) was introduced (Santesteban, 2019). PA is a method of agricultural, forestry and livestock management based on the observation, measurement, and response of the set of quantitative and qualitative inter- and intra-field variables acting in agricultural production. The purpose of PA is to define a decision support system for the entire farm management, with the aim of optimising yields while looking at climatic, environmental, economic, productive, and social sustainability (Ammoniaci et al., 2021). PA involves the collection of data through proximal or remote sensors installed on variable rate technology systems, which carry out the given tasks in a semi- or fully automatic way. The assumption behind PA is that each field, unlike how it is generally considered in conventional agriculture, is not uniform, but is managed considering site-specific characteristics. This management strategy increases the efficiency of agricultural inputs and, if adopted correctly, results in cost savings and increased benefits (Ammoniaci et al., 2021). The concept of precision viticulture (PV) is based on PA. In the same vineyard, there are usually several areas with different soil composition and structure, humidity concentration, sun exposure and microclimate. Consequently, the objectives of PV, i.e. the assessment of the health, vigour, and physiological needs of the vines, are related to the different areas of the vineyard over time, which results in a specific adaptation of cultivation techniques. In addition, one of the objectives of PV is the monitoring of grape bunches during ripening. The data collected may concern the degree of ripeness, sugars (expressed as soluble solids content), anthocyanins, acidity, growth ratio. This monitoring can be aimed at selective grape harvesting, which will affect the quality of the wine (Ammoniaci et al., 2021).

Remote sensing systems for data collection are characterised by optical sensors such as RGB visible (Vis) cameras, multispectral (MS) and hyperspectral (HS) sensors, thermal infrared (TIR) sensors, and other spectroscopic sensors like D-radar, Vis, short-wave infrared (SWIR), short-wave near-infrared (SW-NIR). Remote sensing technologies involve the use of satellites, aircraft, and unmanned aerial vehicles (UAVs) or drones. Their introduction has taken place in the last decade but has faced major challenges due to the organisation of the vineyard in rows and the discontinuous nature of the canopy. These characteristics require a high capacity for processing images, which must have a very high resolution to discriminate the canopy from the ground, and spatial data (Ammoniaci et al., 2021).

Among the most analysed attributes by remote sensing systems are vine vigour, water stress, and more recently also some diseases. Vine vigour was assessed through MS imaging (Khaliq et al., 2019). Vine vigour, obtained from RGB and MS imaging, was also correlated to yield, berry composition and vine sanitary status (Ferrer et al., 2020). Vine vigour and water stress of vines were correlated and validated through RGB, MS and TIR imaging (Pádua et al., 2019; Pádua et al., 2020; Comba et al., 2019). Water stress maps were obtained by comparing vine vigour obtained from SWIR and MS imaging, with leaf stomatal conductance measurements (Kandylakis et al., 2020). MS imaging data has also been combined with a decision-making vine water consumption model in order to optimise irrigation (Bellvert et al., 2021). Water stress assessed by TIR imaging has been compared with traditional vine water status metrics (Pagay & Kidman, 2019). MS imaging has been adopted to evaluate status of flavescence dorée grapevine disease (Albetis et al., 2017; Albetis et al., 2019) and grape trunk disease (Albetis et al., 2019). Flavescence dorée has also been evaluated through RGB imaging (Musci et al., 2020).

Proximal sensing systems can be implemented on ground vehicles monitoring of quality attributes of grape ripening, such as soluble solids content (SSC) and acidity directly in the field. The hyperspectral imaging (HSI) sensors recently adopted can operate at short distance from the vineyard row and due to the high resolution, the bunches of grapes can be easily manually discriminated from the background. An on-the-go HSI system was adopted to estimate the concentration of SSC (coefficient of determination (R^2) = 0.92, root-mean-square error (RMSE) = 1.274 °Brix) and anthocyanins (R^2=0.83, RMSE=0.211 mg g^{-1}) of wine grapes by support vector machines (SVM) (Gutiérrez et al., 2019). Fernández-Novales et al. (2019) acquired hyperspectral images of grape cluster regions along vineyard rows during the period between veraison and harvest. Hyperspectral images were acquired directly in the field using an on-the-go HSI system operating in the 570–990 nm spectral range. Analyses included total soluble solids (TSS), anthocyanin and total polyphenols. The best results obtained from PLS regression models consisted of R^2 of cross-validation (R^2_{cv}) = 0.92 and prediction (R^2_p) = 0.95 for TSS, R^2_{cv}=0.75 and R^2_p=0.79 for anthocyanins, and R^2_{cv}=0.42 and R^2_p=0.43 for total polyphenols. The accuracy of the models, expressed in terms of root-mean-square error of cross-validation (RMSECV) and prediction (RMSEP), resulted in RMSECV=1.25 °Brix and RMSEP=1.01 °Brix for TSS, RMSECV=0.66 mg/fresh berry mass (mg/berry) and RMSEP=0.62 mg/berry for anthocyanins, RMSECV=0.73 absorbance units at 280 nm/fresh berry mass (AU/berry) and RMSEP=0.75 AU/berry for total polyphenols. In another study, the proper maturity of red wine grapes after veraison and up to harvest (through SSC) was assessed by adopting a cart mounted HSI system. By partial least squares regression (PLS) the SSC was predicted (R^2=0.77, RMSECV=0.79 °Brix) and by partial least

squares discriminant analysis (PLS-DA) the samples were classified in the two classes ‘not-ripe’ and ‘ripe’ (correctly classified samples from 86% to 91%) (Benelli et al., 2021b).

Based on the hyperspectral data from the study by Benelli et al. (2021b), the present study aimed to develop a method for the automatic selection of grapes representing the regions of interest (ROIs) on hyperspectral images of a row of wine grapes acquired directly in the field during post-veraison and up to harvest. The selected ROIs were subsequently used to predict the SSC of the grapes.

3.7.2. Materials and methods

3.7.2.1. Samples

The analysis covered approximately 30 m of one side of a vineyard row of red ‘Sangiovese’ grapes (*Vitis vinifera* L.), located near Cesena, Italy. The vineyard row was analysed on 17 different days between August 20th and October 4th, 2019, from post-veraison to harvest time. The row was divided into 11 sections, and from each section, three grapes were taken for each day for reference analysis, giving a total of 561 grape samples (Fig. 3.7.1).

3.7.2.2. Hyperspectral images acquisitions

The study was conducted using a line scan hyperspectral camera (Nano-Hyperspec VNIR, Headwall Photonics, Inc., Fitchburg, MA, USA), operating in the Vis/NIR spectral range (400–1000 nm). The camera is characterized by 272 spectral bands, with a nominal spectral resolution of 2.2 nm, and a spatial resolution of 640 pixels. The used lens (Xenoplan 1.4/17-0903, Schneider-Kreuznach, GmbH, Bad Kreuznach, Rhineland-Palatinate, Germany) presents an effective focal length of 17 mm. The camera was installed on a garden cart, at a height of 120 cm above the ground, and was driven at approximately 1.6 m from the vineyard row analysed.

Hyperspectral image acquisitions were carried out between 10:30 and 12:00. Direct sunlight was used as light source under both clear sky (14 days) and partly cloudy (3 days) conditions. Depending on the light intensity, the exposure time was set between 6 and 8 ms in clear sky conditions, and between 8 and 25 ms in partly cloudy conditions. The exposure time was obtained through calibration with a panel of broadband high-reflectance white target (hardboard coated with white matte finish paint), positioned close to the vineyard row, to cover the entire angle of view of the camera. The integration time was determined as the time yielding a maximum pixel intensity return from the white target.

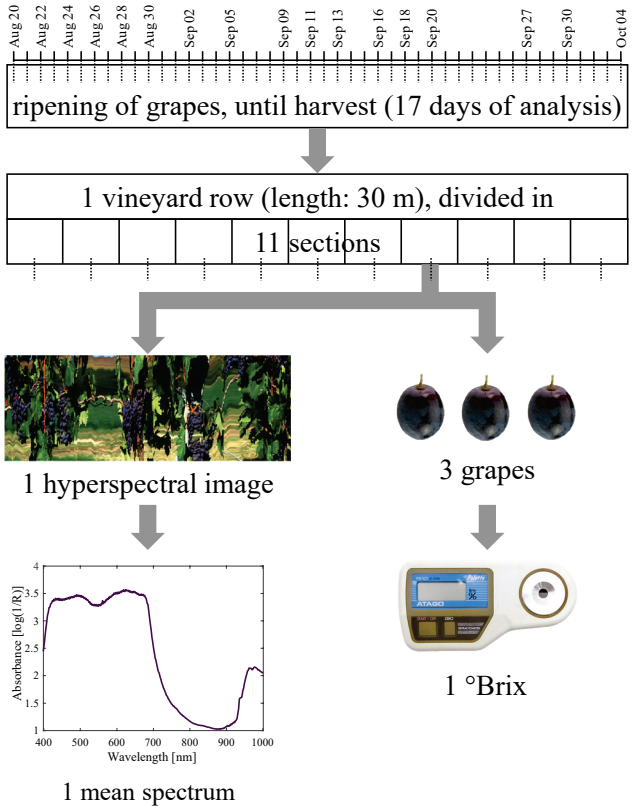

Fig. 3.7.1 – During 17 days of analysis, 187 hyperspectral images of a vineyard row divided into 11 sections were acquired (1 hyperspectral image per section per day of analysis), obtaining 187 mean absorbance spectra; soluble solids content, expressed in °Brix, of 561 grape berries were analysed (3 grape berries per section per day of analysis) by means of a digital refractometer.

Under clear sky conditions, calibration was carried out only once a day, as the acquisition of hyperspectral images of the 11 vineyard row sections required no more than 10 minutes. Under partly cloudy conditions, a calibration was necessary for each acquisition, due to the variability of the intensity of light radiation. This situation extended the analysis time considerably.

A total of 187 hyperspectral images were obtained, one per section of the vineyard row per day of analysis (11 sections × 17 days of analysis = 187 hyperspectral images). From the raw diffuse reflectance spectra (R_R) extracted from the hyperspectral images, the calibrated diffuse reflectance spectra (R_C) were calculated by applying the equation (Guo et al., 2019):

$$R_C = \frac{R_R - R_D}{R_W - R_D} \quad (1)$$

where R_D is the dark reference reflectance spectrum, obtained applying the cap on the lens; R_W are the white reference reflectance spectra, obtained by the above-described white calibration.

Each R_C were finally converted in calibrated diffuse absorbance spectra (A_C) (Sørensen et al., 2021):

$$A_C = log\frac{1}{R_C} \quad (2)$$

3.7.2.3. Soluble solids content measurement

SSC, expressed in °Brix, was measured with a portable digital refractometer (PR-101 Digital Refractometer, ATAGO CO., LTD, Tokyo, Japan) by taking three randomly selected grapes from each of the 11 vineyard row sections for each day of analysis (Fig. 3.7.1). The mean of the °Brix for each section was calculated. Through one-way analysis of variance (ANOVA) with Tukey-HSD post-hoc test (p-level<0.05), significant differences between the mean of SSC for the days of analysis were evaluated.

3.7.2.4. Hyperspectral images elaboration

3.7.2.4.1. RGB images extraction and labelling

An RGB image was extracted from each hyperspectral image, resulting in 187 RGB images. The vertical scan lines forming the RGB images were aligned using a self-alignment algorithm. The image canvas was extended with 150 pixels above and below the scan line data. Then, for each of the scan lines, the neighbour vertical line was shifted from 30 pixels up to 30 pixels down and the RMSE of the gray pixel values were determined for each step (61 steps in total). The chosen shift was selected as the one that yielded the lowest RMSE and applied to all subsequent scans of the image, and then the next scan line was processed. The process was repeated for all scan lines in the image.

A total of 80 RGB images randomly selected were then manually labelled using the Labelbox® web tool (Labelbox, California, USA, 2021). The self-aligned RGB images were manually labelled by assigning 7 different labelling classes: ‘Grapes, sunny’, ‘Grapes, shadow’, ‘Leaf, sunny’, ‘Leaf, shadow’, ‘Background, grass’, ‘Background, sky’, ‘Branches’. Labelling was done coarsely by drawing polygons around relevant areas in the images. At least four areas of each class were selected in all the 80 RGB images, resulting in a total of 2506 areas of interest. Absorbance spectra for the areas

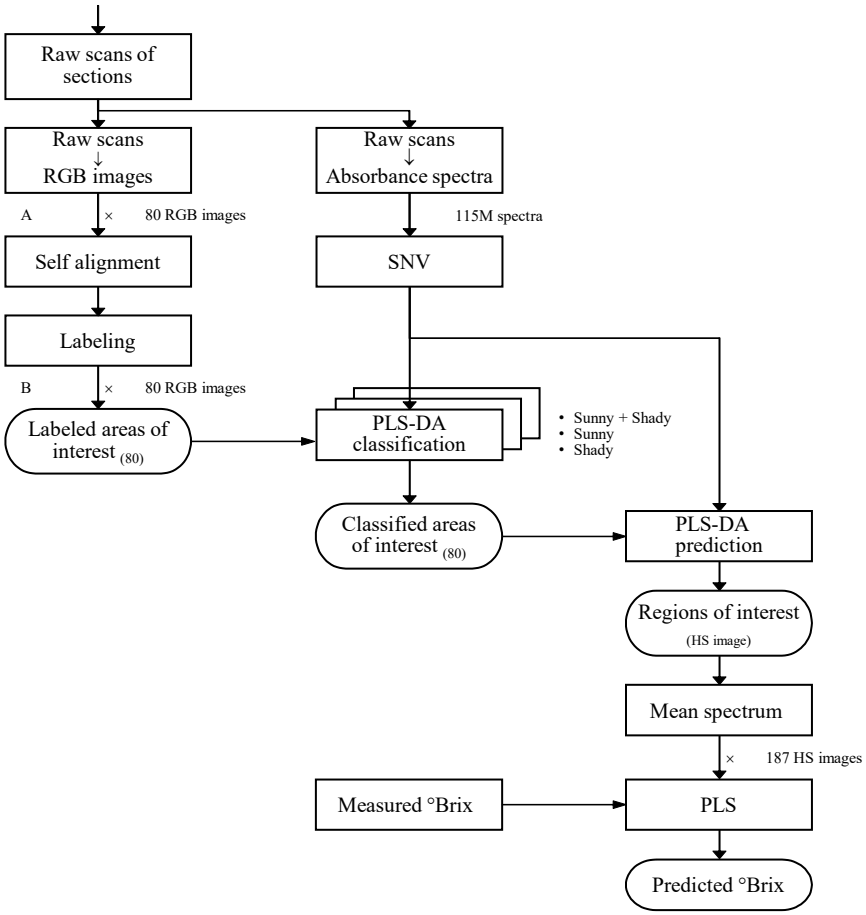

Fig. 3.7.2 – Data flow, from the acquisition of the hyperspectral images of the sections of a vineyard row, to the prediction of °Brix of the grapes.

of interest were extracted from the hyperspectral images as the pixel values circumscribed by the label polygons. Finally, a mean absorbance spectrum was calculated for each selected area, resulting in 2506 labelled mean spectra. The whole flow of the data processing is outlined in Fig. 3.7.2.

3.7.2.4.2. Hyperspectral images classification

The analyses were carried out by PLS Toolbox (PLS_Toolbox, 2020. Eigenvector Research, Inc., Manson, WA, USA) for MATLAB (MATLAB R2020b, The MathWorks, Inc., Natick, Massachusetts, USA) software. PLS-DA (Brereton & Lloyd, 2014) was adopted to classify the mean spectra obtained from the labelling of the 80 randomly selected RGB images.

In order to discriminate the grapes from the background, 'Grapes, sunny' and 'Grapes, shadow' classes were combined in the 'Sunny+Shady' aggregated grape class; therefore, the classes 'Leaf, sunny', 'Leaf, shadow', 'Background, grass', and 'Branches' were combined, obtaining the 'Background' aggregated class. The 'Background, sky' class was excluded due to the high heterogeneity of its mean spectra. The mean spectra were pre-processed by the following methods: smoothing

(window: 9) + standard normal variate (SNV), smoothing (window: 31) + detrend (polynomial order: 1, to remove linear offset), smoothing (window: 15) + extended multiplicative scatter correction (EMSC), Savitzky-Golay first derivative (smoothing window: 7; polynomial order: 2), and second derivative (smoothing window: 15; polynomial order: 2), all followed by mean centring (MC) (Rinnan et al., 2009). Afterwards, the interval PLS (*i*PLS) method for variable region selection was applied, testing 4 different interval sizes (6, 12, 25, 50) in 'forward' mode, with non-overlapping intervals subsequently and automatically included in the analysis (Nørgaard et al., 2000). The PLS-DA models were validated by leave-one-section-out cross-validation ('section' refers to a single hyperspectral image of a vineyard section, see Fig. 3.7.1). Only PLS-DA models with sensitivity and specificity values for the aggregated class 'Sunny+Shady' greater than or equal to 0.99 were considered. Finally, the PLS-DA model that simultaneously showed the lowest number of latent variables and the highest sensitivity or specificity value for the 'Sunny+Shady' aggregated class was selected.

Afterwards, the two classes 'Grapes, sunny' and 'Grapes, shadow' (renamed to 'Sunny' and 'Shady', respectively) were considered individually in order to discriminate grapes exposed directly to the sun and grapes in the shadow from their respective backgrounds.

The same pre-processing as for the PLS-DA classification model selected for the aggregated class 'Sunny+Shady' was used to calculate the new PLS-DA classification models, then variable selection was performed using the same *i*PLS method (interval sizes: 6, 12, 25, 50) described above. Finally, the two best PLS-DA classification models for the 'Sunny' and 'Shady' classes respectively were selected in terms of best performance for sensitivity, specificity, and low number of latent variables (Fig. 3.7.2).

3.7.2.4.3. Regions of interest of the hyperspectral images

The three previously selected PLS-DA classification models (related to grape classes 'Sunny+Shady', 'Sunny, and 'Shady') were then adopted to predict the ROIs of the whole hyperspectral image set (187). Each class of ROI would include spectra attributed to the three grape classes 'Sunny+Shady', 'Sunny', and 'Shady', respectively. Two different set of classification threshold where tested, one at 50% of the predicted values and one at 90% of the predicted values (the 'Super' threshold). Ergo, a total of six classes were obtained: 'Sunny+Shady', 'Sunny' and 'Shady' for the first threshold, 'Super Sunny+Shady', 'Super Sunny' and 'Super Shady' for the second threshold (Fig. 3.7.2).

3.7.2.4.4. Soluble solids content of grapes prediction

The mean absorbance spectra relative to each ROIs class were calculated for each of the 187 hyperspectral images, resulting in six mean spectra (one per ROI class) for each hyperspectral image.

The 187 mean spectra for each of the classes of ROIs were used to predict the SSC of the grapes (in °Brix). Two pre-processing methods, SNV and Savitzky-Golay second derivative (smoothing window: 19; polynomial order: 2), both followed by MC, were used to calculate PLS models; models were validated by leave-one-day-out and leave-one-section-out cross-validation.

Finally, the resulting PLS models were compared with PLS models obtained by manual selection of ROIs (Benelli et al., 2021b). The best PLS models, in terms of number of latent variables, R^2_{CV} and RMSECV, were selected and recalculated by adopting two variable selection methods, *i*PLS and recursive weighted partial least squares (*r*PLS) (Rinnan et al., 2014) (Fig. 3.7.2).

3.7.3. Results and discussion

Mean values of the SSC and standard deviations by day of analysis are reported in Fig. 3.7.3. The SSC ranged from 17.8 °Brix on the first day of analysis (August 20) to 22.7 °Brix during the last day of analysis (October 4), which represents a rise of 27.5%. Significant differences were found between the mean °Brix values for the days of analysis. Due to adverse weather conditions, i.e., rain or extensive cloud cover, it was

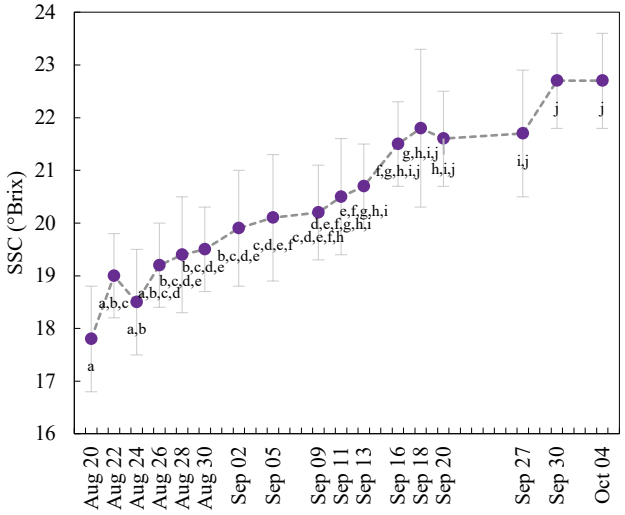

Fig. 3.7.3 – Means (filled purple circles) and standard deviations (grey bars) of soluble solids content (SSC, expressed in °Brix) during the 17 days of analysis. Means with the same letter are not significantly different at p-level<0.05.

not possible to carry out in-field analyses at regular time intervals: this occurred several times between September 20 and September 27.

Random selection of 80 RGB images from the entire set of 187 hyperspectral images was performed in order to calculate mean absorbance spectra from the labelled areas of interest. The seven-class labelling of the RGB images ('Grapes, sunny', 'Grapes, shadow', 'Leaf, sunny', 'Leaf, shadow', 'Background, grass', 'Background, sky', 'Branches') was simplified by the alignment of the vertical scan lines resulting from the acquisition of the hyperspectral images: indeed, the up-down shifts on the vertical plane of the hyperspectral camera, mainly due to the roughness on the ground on which the cart was running, resulted in a significant misalignment of the vertical scan lines. Therefore, for future analysis, it is recommended to install the hyperspectral camera on a gimbal-type three-axis stabilization system to reduce this problem and include an encoder on the card wheelbase synchronized to the camera line scan acquisition.

The best PLS-DA classification models of grapes relative to the aggregated class 'Sunny+Shady' were obtained by pre-processing with smoothing (window: 9) + SNV + MC, and *i*PLS variable selection method (interval size = 50). The PLS-DA model include 3 latent variables and has a resulting sensitivity and specificity values of 0.991 and 0.996, respectively. However, all PLS-DA models performed well, with number of latent variables between 2 and 8 and with sensitivity and specificity values no lower than 0.983 and 0.960, respectively (Table 3.7.1). The same pre-processing applied to the PLS-DA models for the classification of grapes exposed to sun or shade (classes 'Sunny' and 'Shady', respectively) produced slightly inferior results. The best PLS-DA model of grapes exposed to direct solar radiation (class 'Sunny'), using 4 latent variables and *i*PLS interval size = 6, resulted in a sensitivity = 0.988 and specificity = 0.940. Finally, the best PLS-DA model for classification of grapes in shade (class 'Shady'), using 9 latent variables and *i*PLS interval size = 6, resulted in a sensitivity and specificity of 0.920 and 0.927 respectively.

Afterwards, the three PLS-DA classification models reported were used in prediction to define the ROIs of the whole set of hyperspectral images of the vineyard sections. Finally, the mean absorbance spectra of the 6 classes of ROIs obtained, 'Sunny+Shady', 'Sunny', 'Shady', 'Super Sunny+Shady', 'Super Sunny', 'Super Shady', were used to calculate PLS models to predict the °Brix of grapes (Table 3.7.2).

The mean absorbance spectra of the grape ROIs (classes 'Sunny+Shady', 'Sunny', and 'Shady') obtained by averaging the mean spectra of the respective ROIs of the entire set of hyperspectral images are shown in Fig. 3.7.4. Considering the spectral range of the hyperspectral camera adopted (400–1000 nm), the NIR region is particularly interesting for SSC-related spectral information. The second overtone O–H stretching vibration for water is observed at 960–970 nm and for carbohydrates

Table 3.7.1 – PLS-DA models to discriminate the grapes ('Sunny+Shady', 'Sunny', and 'Shady' aggregated grape classes) from the background (obtained aggregating the remaining classes, except 'Background, sky').

Aggregated grape class	Pre-processing	All variables / *i*PLS int. size	#LVs	Sensitivity (CV)	Specificity (CV)
Sunny+Shady	SNV	All	4	0.994	0.996
	SNV	6	3	0.986	0.996
	SNV	12	6	0.994	0.996
	SNV	25	4	0.992	0.995
	SNV	50	3	0.991	0.996
	D1	All	3	0.992	0.995
	D1	6	2	0.990	0.985
	D1	12	8	0.992	0.996
	D1	25	4	0.988	0.996
	D1	50	4	0.990	0.996
	D2	All	3	0.988	0.985
	D2	6	4	0.991	0.990
	D2	12	3	0.987	0.991
	D2	25	4	0.985	0.991
	D2	50	3	0.985	0.994
	Detrend	All	5	0.992	0.997
	Detrend	6	5	0.991	0.996
	Detrend	12	4	0.987	0.995
	Detrend	25	6	0.994	0.995
	Detrend	50	3	0.986	0.997
	EMSC	All	3	0.992	0.979
	EMSC	6	5	0.994	0.974
	EMSC	12	5	0.992	0.974
	EMSC	25	3	0.988	0.960
	EMSC	50	5	0.990	0.969
Sunny	SNV	6	4	0.988	0.940
Shady	SNV	6	9	0.920	0.927

Note – Pre-processing methods details. SNV (standard normal variate): smoothing, window = 9 + SNV + MC (mean centring). D1 (Savitzky-Golay first derivative): D1, smoothing window = 7, polynomial order = 2 + MC; D2 (Savitzky-Golay second derivative): D2, smoothing window = 15, polynomial order = 2 + MC. Detrend: smoothing, window = 31 + detrend, polynomial order = 1 + MC. EMSC (extended multiplicative scatter correction): smoothing, window = 15+ EMSC + MC.
iPLS int. size: iPLS interval size. # LVs: number of latent variables. CV: leave-one-section-out cross-validation.

in the 950–1000 nm region; the third overtone of the C–H stretching vibrations is found at around 900 nm. Since the water content of ripe wine grapes is 70–80% (FAO, 2009), the water-related absorption bands dominate over the carbohydrate-related ones, but it was observed that the water absorption peaks in the NIR spectral region are not very marked and broad, so the carbohydrate-related spectral information should be less covered by the water-related information (Manley et al., 2007; Camps & Christen, 2009).

The best PLS models were obtained with SNV pre-processing and leave-one-day-out cross-validation was adopted to validate the models. The SNV pre-processing was not preceded by smoothing, as in the case of the PLS-DA models, since the calculation of the mean spectra of the ROIs contributed to reduce the high noise level present at the single spectrum level. In particular, the PLS model of the ROIs related to the 'Sunny+Shady' class (using 5 latent variables) resulted in R^2_{CV}=0.69 and

Table 3.7.2 – Results of PLS models obtained by adopting the different classes of regions of interest (Sunny+Shady, Sunny, Shady, Super Sunny+Shady, Super Sunny, Super Shady, manual selection) and applying the reported preprocessing (SNV and 2nd derivative) and cross-validation methods (leave-one-day out and leave-one-section out).

ROIs	Prepro.	#LV	R^2_{cal}	R^2_{CV}	RMSEC	RMSECV	#LV	R^2_{cal}	R^2_{CV}	RMSEC	RMSECV
		Leave-one-day out cross-validation					Leave-one-section out cross-validation				
Sunny+Shady	SNV	5	0.73	0.69	0.87	0.94	5	0.73	0.69	0.87	0.94
	2D	5	0.71	0.58	0.91	1.09	4	0.65	0.56	1.00	1.13
Sunny	SNV	6	0.61	0.51	1.06	1.19	6	0.61	0.49	1.06	1.22
	2D	6	0.63	0.45	1.03	1.27	8	0.68	0.59	0.96	1.09
Shady	SNV	9	0.80	0.67	0.75	0.97	8	0.79	0.71	0.77	0.92
	2D	3	0.62	0.53	1.05	1.16	3	0.62	0.56	1.05	1.13
Super	SNV	4	0.73	0.67	0.88	0.97	5	0.73	0.69	0.87	0.95
Sunny+Shady	2D	5	0.67	0.55	0.97	1.14	4	0.63	0.55	1.02	1.14
Super Sunny	SNV	8	0.51	0.30	1.18	1.43	8	0.51	0.37	1.18	1.36
	2D	8	0.60	0.33	1.07	1.41	7	0.57	0.43	1.10	1.29
Super Shady	SNV	9	0.81	0.67	0.74	0.97	8	0.79	0.71	0.77	0.92
	2D	3	0.61	0.51	1.05	1.18	3	0.61	0.55	1.05	1.14
Manual selection	SNV	7	0.76	0.70	0.83	0.92	3	0.70	0.66	0.92	0.98
	2D	6	0.73	0.66	0.87	0.98	3	0.69	0.63	0.94	1.03

Note – ROIs: regions of interest; Prepro.: preprocessing method; #LV: number of latent variables; CV: cross-validation; SNV: standard normal variate; 2D: 2nd derivative, window dimension = 19.

RMSECV=0.94 °Brix; a similar result was obtained with the 'Super Sunny+Shady' ROIs, with an R^2_{CV}=0.67 and RMSECV=0.97 °Brix, using 4 latent variables. These results are comparable to previous PLS prediction results obtained with the ROIs from manual selection, with R^2_{CV}=0.70 and RMSECV=0.92 °Brix, but with a much higher number of latent variables (8) (Table 3.7.2).

Finally, two variable selection methods, *i*PLS and *r*PLS, were applied to the three PLS models described. *i*PLS proved to be a suitable method for data reduction and

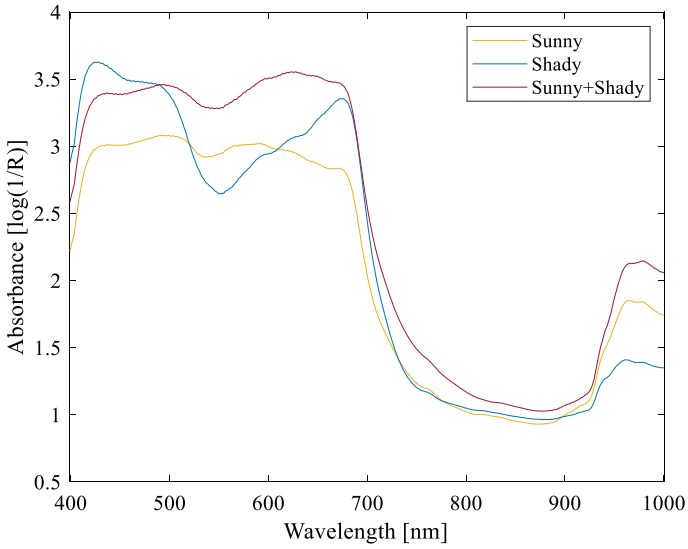

Fig. 3.7.4 – Grapes mean absorbance spectra related to the 3 classes defined (Sunny, Shady, Sunny+Shady).

localisation of informative spectral regions, thus improving the predictive performance and simplicity of the PLS models. The best PLS model was obtained for the 'Sunny+Shady' ROIs: by using 4 latent variables and *i*PLS interval size = 12, R^2_{CV}=0.74 and RMSECV=0.86 °Brix were obtained. Similar results were also achieved with the ROIs 'Super Sunny+Shady': by using 5 latent variables and *i*PLS interval size = 25, R^2_{CV}=0.74 and RMSECV=0.86 °Brix were obtained (Fig. 3.7.5). These results are comparable with those relative to the manual selection of ROIs: the PLS model, using 6 latent variables and *i*PLS interval size = 6, resulted in R^2_{CV}=0.73 and RMSECV=0.87 °Brix (Table 3.7.3).

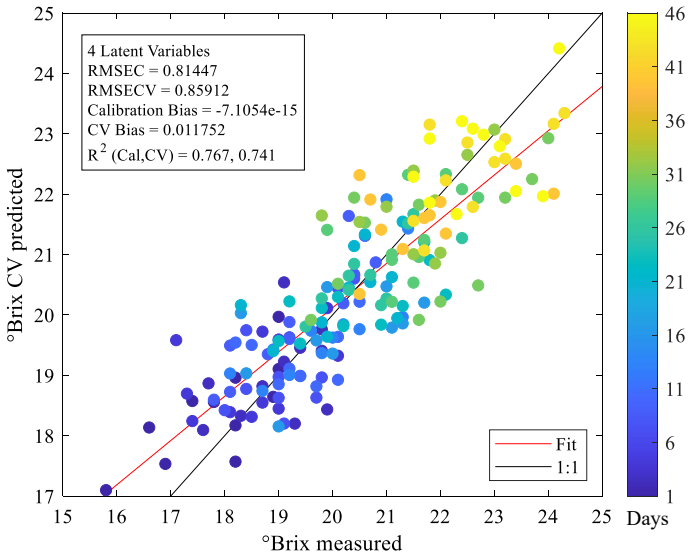

Fig. 3.7.5 – Measured vs predicted values of soluble solids content (°Brix) obtained by PLS regression (cross validation).

The application of Vis/NIR spectroscopic techniques to predict the SSC of grapes directly in the field has already been reported and described in literature. Using Portable Vis/NIR spectrometers and PLS regression, R^2_{CV}=0.72 and a standard error of prediction in cross-validation (SEPCV) = 0.61 °Brix (Diezma-Iglesias et al., 2008), correlation coefficient in prediction (r_P) = 0.82 and RMSEP=1.48 °Brix (Guidetti et al., 2010) were obtained. By means of support vector machine regression (SVMR) Gutiérrez et al. (2018) obtained R^2_P=0.92 and RMSEP=1.274 °Brix. Benelli et al. (2021b) obtained R^2_{CV}=0.77 and RMSECV=0.79 °Brix from the dataset used for the present study, but excluding the days of analysis without clear sky, and by manual selection of the ROIs. The results of the present study are thus comparable with those reported in literature, and in particular the prediction errors, RMSE, obtained are slightly better than those obtained by Gutiérrez et al. (2018).

Table 3.7.3 – PLS models obtained by adopting the ROIs and the settings (SNV preprocessing and leave-one-day out cross-validation methods) of the three best PLS models reported on Table 3.7.2, and two variable selection methods (*i*PLS and *r*PLS).

ROIs	Var. sel. method	*i*PLS window/ *r*PLS mode	#LV	#var.	R^2_{cal}	R^2_{CV}	RMSEC	RMSECV
Sunny+Shady	–	–	5	All	0.73	0.69	0.87	0.94
	*i*PLS	6	9	23	0.78	0.73	0.79	0.88
	*i*PLS	12	4	84	0.77	0.74	0.81	0.86
	*i*PLS	25	6	49	0.79	0.74	0.78	0.86
	*i*PLS	50	3	99	0.73	0.69	0.88	0.94
	*r*PLS	surveyed	7	29	0.75	0.66	0.85	0.98
	*r*PLS	specified 5 LV	4	72	0.74	0.70	0.86	0.92
	*r*PLS	suggested	3	17	0.73	0.69	0.88	0.94
Super Sunny+Shady	–	–	4	All	0.73	0.67	0.88	0.97
	*i*PLS	6	5	12	0.75	0.70	0.84	0.92
	*i*PLS	12	7	36	0.79	0.75	0.78	0.84
	*i*PLS	25	5	49	0.77	0.74	0.80	0.86
	*i*PLS	50	4	50	0.75	0.71	0.85	0.91
	*r*PLS	surveyed	7	25	0.76	0.63	0.83	1.04
	*r*PLS	specified 4 LV	5	28	0.72	0.69	0.89	0.97
	*r*PLS	suggested	5	28	0.72	0.69	0.89	0.97
Manual	–	–	7	All	0.76	0.70	0.83	0.92
	*i*PLS	6	6	48	0.76	0.73	0.83	0.87
	*i*PLS	12	3	108	0.72	0.70	0.90	0.93
	*i*PLS	25	6	100	0.76	0.71	0.82	0.91
	*i*PLS	50	6	100	0.76	0.71	0.82	0.91
	*r*PLS	surveyed	3	27	0.68	0.60	0.96	1.07
	*r*PLS	specified 7 LV	4	13	0.65	0.56	1.00	1.13
	*r*PLS	suggested	1	19	0.69	0.67	0.94	0.96

Note – ROIs: regions of interest; Var. sel. method: variable selection method; #LV: number of latent variables; #var.: number of variables; iPLS: interval PLS; rPLS: recursive weighted PLS.

3.7.4. Conclusions

The present study provided a valid and automatic classification method of the regions of interest for grapes in hyperspectral images of vineyard row sections during post-veraison and up to harvest. Moreover, the mean spectra obtained from the automatic mapping of the regions of interest demonstrated to provide prediction results on par with those obtained by carefully manual selections of the regions of interest using simpler models (fewer PLS components) giving promise of more robust predictions of the maturity of the grapes as measured by the SSC content.

3.7.5. References

Albetis, J., Duthoit, S., Guttler, F., Jacquin, A., Goulard, M., Poilvé, H., Féret, J. B., & Dedieu, G. (2017). Detection of Flavescence dorée Grapevine Disease Using Unmanned Aerial Vehicle (UAV) Multispectral Imagery. *Remote Sensing*, *9*(4), 308. https://doi.org/10.3390/rs9040308

Albetis, J., Jacquin, A., Goulard, M., Poilvé, H., Rousseau, J., Clenet, H., Dedieu, G., & Duthoit, S. (2019). On the Potentiality of UAV Multispectral Imagery to Detect Flavescence dorée and Grapevine Trunk Diseases. *Remote Sensing*, *11*(1), 23. https://doi.org/10.3390/rs11010023

Ammoniaci, M., Kartsiotis, S. P., Perria, R., & Storchi, P. (2021). State of the Art of Monitoring Technologies and Data Processing for Precision Viticulture. *Agriculture*, *11*(3), 201. https://doi.org/10.3390/agriculture11030201

Bellvert, J., Mata, M., Vallverdú, X., Paris, C., & Marsal, J. (2021). Optimizing precision irrigation of a vineyard to improve water use efficiency and profitability by using a decision-oriented vine water consumption model. *Precision Agriculture*, *22*, 319–341. https://doi.org/10.1007/s11119-020-09718-2

Benelli, A., Cevoli, C., Ragni, L., & Fabbri, A. (2021). In-field and non-destructive monitoring of grapes maturity by hyperspectral imaging. *Biosystems Engineering*, *207*, 59–67. https://doi.org/10.1016/j.biosystemseng.2021.04.006

Brereton, R. G., & Lloyd, G. R. (2014). Partial least squares discriminant analysis: taking the magic away. *Journal of Chemometrics*, *28*(4), 213–225. https://doi.org/10.1002/CEM.2609

Camps, C., & Christen, D. (2009). On-tree follow-up of apricot fruit development using a hand-held NIR instrument. *Journal of Food, Agriculture and Environment*, *7*(2), 394–400.

Comba, L., Biglia, A., Aimonino, D. R., Barge, P., Tortia, C., & Gay, P. (2019). 2D and 3D data fusion for crop monitoring in precision agriculture. *2019 IEEE International Workshop on Metrology for Agriculture and Forestry (MetroAgriFor)*, 62–67. https://doi.org/10.1109/MetroAgriFor.2019.8909219

Diezma-Iglesias, B., Barreiro, P., Blanco, R., & García-Ramos, F. J. (2008). Comparison of robust modeling techniques on NIR spectra used to estimate grape quality. *Acta Horticulturae*, *802*, 367–372. https://doi.org/10.17660/ActaHortic.2008.802.48

Droulia, F., & Charalampopoulos, I. (2021). Future Climate Change Impacts on European Viticulture: A Review on Recent Scientific Advances. *Atmosphere*, *12*(4), 495. https://doi.org/10.3390/atmos12040495

FAO (Food and Agriculture Organization). (2009). *Grapes Wine - Agribusiness Handbook*. http://www.fao.org/3/al176e/al176e.pdf

Fernández-Novales, J., Tardáguila, J., Gutiérrez, S., & Paz Diago, M. (2019). On-The-Go VIS + SW − NIR Spectroscopy as a Reliable Monitoring Tool for Grape Composition within the Vineyard. *Molecules*, *24*(15), 2795. https://doi.org/10.3390/molecules24152795

Ferrer, M., Echeverría, G., Pereyra, G., Gonzalez-Neves, G., Pan, D., & Mirás-Avalos, J. M. (2020). Mapping vineyard vigor using airborne remote sensing: relations with yield, berry composition and sanitary status under humid climate conditions. *Precision Agriculture*, *21*(1), 178–197. https://doi.org/10.1007/s11119-019-09663-9

Guidetti, R., Beghi, R., & Bodria, L. (2010). Evaluation of grape quality parameters by a simple VIS/NIR system. *Transactions of the ASABE*, *53*(2), 477–484. https://doi.org/10.13031/2013.29556

Guo, W., Li, W., Yang, B., Zhu, Z. Z., Liu, D., & Zhu, X. (2019). A novel noninvasive and cost-effective handheld detector on soluble solids content of fruits. *Journal of Food Engineering*, *257*, 1–9. https://doi.org/10.1016/j.jfoodeng.2019.03.022

Gutiérrez, S., Tardaguila, J., Fernández-Novales, J., & Diago, M. P. (2019). On-the-go hyperspectral imaging for the in-field estimation of grape berry soluble solids and anthocyanin concentration. *Australian Journal of Grape and Wine Research*, *25*(1), 127–133.

https://doi.org/10.1111/ajgw.12376

Hunter, J. J., Volschenk, C. G., Mania, E., Castro, A. V., Booyse, M., Guidoni, S., Pisciotta, A., Lorenzo, R. Di, Novello, V., & Zorer, R. (2021). Grapevine row orientation mediated temporal and cumulative microclimatic effects on grape berry temperature and composition. *Agricultural and Forest Meteorology*, *310*, 108660. https://doi.org/10.1016/j.agrformet.2021.108660

Kandylakis, Z., Falagas, A., Karakizi, C., & Karantzalos, K. (2020). Water Stress Estimation in Vineyards from Aerial SWIR and multispectral UAV data. *Remote Sensing*, *12*(15), 2499. https://doi.org/10.3390/RS12152499

Keller, M. (2020a). Developmental physiology. In *The Science of Grapevines* (3rd Ed., pp. 199–277). Academic Press. https://doi.org/10.1016/B978-0-12-816365-8.00006-3

Keller, M. (2020b). Phenology and growth cycle. In *The Science of Grapevines* (3rd Ed., pp. 61–103). Academic Press. https://doi.org/10.1016/B978-0-12-816365-8.00002-6

Khaliq, A., Comba, L., Biglia, A., Ricauda Aimonino, D., Chiaberge, M., & Gay, P. (2019). Comparison of satellite and UAV-based multispectral imagery for vineyard variability assessment. *Remote Sensing*, *11*(4). https://doi.org/10.3390/rs11040436

Labelbox. (2021). *Labelbox*. [Online]. https://labelbox.com/

Manley, M., Joubert, E., Myburgh, L., Lotz, E., & Kidd, M. (2007). Prediction of soluble solids content and post-storage internal quality of Bulida apricots using near infrared spectroscopy. *Journal of Near Infrared Spectroscopy*, *15*(3), 179–188. https://doi.org/10.1255/jnirs.725

McGlone, V. A., & Kawano, S. (1998). Firmness, dry-matter and soluble-solids assessment of postharvest kiwifruit by NIR spectroscopy. *Postharvest Biology and Technology*, *13*(2), 131–141. https://doi.org/10.1016/S0925-5214(98)00007-6

Musci, M. A., Persello, C., & Lingua, A. M. (2020). UAV images and deep-learning algorithms for detecting flavescence doree disease in grapevine orchards. *The International Archives of the Photogrammetry, Remote Sensing and Spatial Information Sciences*, *XLIII*(B3), 1483–1489. https://doi.org/10.5194/isprs-archives-XLIII-B3-2020-1483-2020

Nicolaï, B. M., Beullens, K., Bobelyn, E., Peirs, A., Saeys, W., Theron, K. I., & Lammertyn, J. (2007). Nondestructive measurement of fruit and vegetable quality by means of NIR spectroscopy: A review. *Postharvest Biology and Technology*, *46*(2), 99–118. https://doi.org/10.1016/j.postharvbio.2007.06.024

Nørgaard, L., Saudland, A., Wagner, J., Nielsen, J. P., Munck, L., & Engelsen, S. B. (2000). Interval Partial Least-Squares Regression (iPLS): A Comparative Chemometric Study with an Example from Near-Infrared Spectroscopy. *Applied Spectroscopy*, *54*(3), 413–419. https://www.osapublishing.org/as/abstract.cfm?uri=as-54-3-413

OIV (International Organisation of Vine and Wine Intergovernmental Organisation). (2021). *World Wine Production Outlook, First Estimates 4 November 2021*. https://www.oiv.int/public/medias/8553/en-oiv-2021-world-wine-production-first-estimates-to-update.pdf

Pádua, L., Adão, T., Sousa, A., Peres, E., & Sousa, J. J. (2020). Individual Grapevine Analysis in a Multi-Temporal Context Using UAV-Based Multi-Sensor Imagery. *Remote Sensing*, *12*(1), 139. https://doi.org/10.3390/RS12010139

Pádua, L., Marques, P., Adão, T., Guimarães, N., Sousa, A., Peres, E., & Sousa, J. J. (2019). Vineyard variability analysis through UAV-based vigour maps to assess climate change impacts. *Agronomy*, *9*(10). https://doi.org/10.3390/agronomy9100581

Pagay, V., & Kidman, C. M. (2019). Evaluating Remotely-Sensed Grapevine (Vitis vinifera L.) Water Stress Responses across a Viticultural Region. *Agronomy*, *9*(11), 682. https://doi.org/10.3390/agronomy9110682

Pu, H., Liu, D., Wang, L., & Sun, D. W. (2016). Soluble Solids Content and pH Prediction and Maturity Discrimination of Lychee Fruits Using Visible and Near Infrared Hyperspectral Imaging. *Food Analytical Methods*, *9*(1), 235–244. https://doi.org/10.1007/s12161-015-0186-7

Rinnan, Å., Andersson, M., Ridder, C., & Engelsen, S. B. (2014). Recursive weighted partial least squares (rPLS): an efficient variable selection method using PLS. *Journal of Chemometrics*,

28(5), 439–447. https://doi.org/10.1002/cem.2582

Rinnan, Å., van den Berg, F., & Engelsen, S. B. (2009). Review of the most common pre-processing techniques for near-infrared spectra. *TrAC Trends in Analytical Chemistry*, *28*(10), 1201–1222. https://doi.org/10.1016/j.trac.2009.07.007

Romero, P., Navarro, J. M., & Ordaz, P. B. (2022). Towards a sustainable viticulture: The combination of deficit irrigation strategies and agroecological practices in Mediterranean vineyards. A review and update. *Agricultural Water Management*, *259*, 107216. https://doi.org/10.1016/J.AGWAT.2021.107216

Santesteban, L. G. (2019). Precision viticulture and advanced analytics. A short review. *Food Chemistry*, *279*(April 2018), 58–62. https://doi.org/10.1016/j.foodchem.2018.11.140

Sørensen, K. M., Berg, F. van den, & Engelsen, S. B. (2021). NIR Data Exploration and Regression by Chemometrics—A Primer. In Y. Ozaki, C. Huck, S. Tsuchikawa, & S. B. Engelsen (Eds.), *Near-Infrared Spectroscopy* (pp. 127–189). Springer, Singapore. https://doi.org/10.1007/978-981-15-8648-4_7

4. CONCLUSIONS

The monitoring of food quality attributes plays a key role in achieving products with the desired characteristics. In particular, in the fruit sector, the monitoring of quality attributes related to the state of ripeness of the fruit is of great interest, *e.g.*, to decide the time of harvest or marketing. Measuring quality attributes is traditionally carried out by destructive analytical techniques, which require long operating times and high costs. Alternatively, rapid and cost-effective measurements can be achieved through the application of optical techniques. Based on this premise, the work of the present PhD project was aimed at exploring and deepening knowledge in this research field. First, a lab-scale HSI system was developed and adopted for the rapid and non-destructive measurement of quality attributes such as FF and SSC of apricots and kiwis. The FF of kiwi fruit was then measured using a NSD, and finally, the tannins of red wine were measured using a device based on SSPP. Finally, a ground-based HSI system was developed and adopted directly in the field and in daylight conditions to monitor the SSC of wine grapes from post-veraison to harvest.

The application of the HSI technique resulted suitable for the estimation of the quality attributes of the fruits analysed in the laboratory, but in case of low level of variation of the quality attribute, as for the SSC of the analysed apricots, poorer results were obtained. The HSI technique could therefore be implemented in a real-time sorting line, but in the case of specific use on a single product variety, it would be worthwhile to develop a more cost-effective multispectral system, focusing on segmentation techniques for ROIs selection, dimensionality reduction through variable selection, and process automation.

The NDS provided good results in estimating the FF of kiwifruit. The technique offers the advantage of easy implementation in a sorting line and has very low application costs, but it could certainly be improved, perhaps by optimising spectral emission and lamp power.

The SSPP technique provided excellent results in estimating the procyanidin content of red wine. The SSPP technique has therefore proved to be a valid, rapid, and cost-effective alternative to traditional techniques, but care should be taken with the analytical timing and methods, as the turbidity degree of the wine-gelatine mixture is not stable over time.

The two studies concerning the application of the HSI technique directly in the field to estimate the degree of ripeness of wine grapes have demonstrated the potential of the HSI technique outside the laboratory. The results of estimating the SSC content were moderate, and certainly influenced by the numerous environmental variables, in particular the variability of light intensity (affected by atmospheric conditions, time, and date), heat, humidity, wind, and finally soil irregularities, which should be overcome by adopting a hyperspectral camera stabilisation system. The method of automatic selection of the regions of interest finally proved to be as good as the manual one.

HSI produces a huge amount of information, requiring large storage capacities and data processing capacity. For these reasons, during the research period, various techniques for the segmentation of hyperspectral images for the selection of ROIs, as well as dimensionality reduction techniques through the selection of variables, have been progressively investigated and adopted, with an orientation towards the introduction of elements of automation of data processing, calibration, and validation of statistical models. A common solution in the field of HSI is the consequent development of multispectral systems, including portable ones, which are less expensive and less demanding in terms of data processing capacity, but have a narrower field of application. Meanwhile, technological evolution is moving towards a reduction in the size and cost of devices, and an increase in computing and storage capacity, making the adoption of HSI systems increasingly accessible, with greater versatility and more information obtainable compared to multispectral systems. The application of hyperspectral or multispectral systems in ground-based vehicles, such as tractors, offers great potential in the development of techniques for real-time monitoring of vegetative parameters and quality attributes of plants and fruits. Such an approach fits well with the objectives of precision agriculture, providing information that contributes to the optimisation of resource use. However, applying these technologies directly in the field raises great challenges, given the number of environmental variables involved, so it would be particularly interesting to deepen knowledge in this context, and to look for new solutions.